COMPUTATIONAL MODELING OF FALLING LIQUID FILM FREE SURFACE EVAPORATION

A Thesis
Presented to
The Academic Faculty

by

Emmanuel O. Doro

In Partial Fulfillment
of the Requirements for the Degree
Doctor of Philosophy in Mechanical Engineering

Georgia Institute of Technology
August 2012

COMPUTATIONAL MODELING OF FALLING LIQUID FILM FREE SURFACE EVAPORATION

Approved by:

Dr. Cyrus K. Aidun, Advisor
Mechanical Engineering
Georgia Institute of Technology

Dr. Mostafa Ghiaasiaan
Mechanical Engineering
Georgia Institute of Technology

Dr. Yogendra Joshi
Mechanical Engineering
Georgia Institute of Technology

Dr. Jeff Hsieh
Chemical & Biomolecular Engineering
Georgia Institute of Technology

Dr. Preet Singh
Material Science & Engineering
Georgia Institute of Technology

Dr. Chris Verrill
Principal Scientist
International Paper

Date Approved: 14 June 2012

To Funmi & Nnenne

ACKNOWLEDGEMENTS

I would like to express my gratitude to the Institute of Paper Science and Technology (IPST) at Georgia Institute of Technology for funding this research through the PSE Graduate Research Fellowship. I would like to thank my advisor Dr. Cyrus K. Aidun for his guidance and input on my research. I would also like to thank Dr. Mathias Gourdon at Chalmers University of Technology - Sweden for his collaboration on experimental validation.

TABLE OF CONTENTS

LIST OF TABLES

LIST OF FIGURES

NOMENCLATURE

A	coefficient matrix of linear system
A_{I}	interfacial area
$a_{_P}$	discretization coefficient at cell p in generic transport equation
$\boldsymbol{b}$	vector of RHS in generic transport linear system
b_P^o	source term
c_p	specific heat
C_b	soluble solids mass concentration in the bulk flow
Ca	Capillary number
E_{act}	activation energy
f	perturbation frequency
f	subscript designating variable evaluated at control volume cell face
$\boldsymbol{H}(\boldsymbol{v})$	operator in semi-discrete momentum equation
$\triangle H_s^o$	enthalpy of crystallization
h	heat transfer coefficient
h_e	enthalpy of vaporization
h_p	maximum wave height
j_e^h	evaporation heat flux density
$\bar{K}_r$	pre-exponential factor in Arrhenius equation

K	temperature in Kelvin
k	thermal conductivity
$K_{_F}$	physical properties group in Nosoko *et al.* (1995) correlation
K_r	surface rate constant
Ka	Kapitza number
L	wave separation of regular 2-D waves
l, g	subscripts for liquid, vapor/gas properties
$l_{_\mathrm{T}}$	thermal length scale
L_e	evaporator length
l_v	viscous length scale
m_s	mass rate of salt precipitation
N	neighbor control volume cell
n	superscript designating current time step
N_{hp}	non-dimensional maximum wave height
N_L	non-dimensional wave separation
N_{uw}	non-dimensional wave speed
Nu	Nusselt number
o	superscript designating previous time step
P	control volume cell over which equation is discretized
p	pressure

p_x streamwise pressure gradient

Pr Prandtl number

$\boldsymbol{q}_P^o$ vector of explicit terms in semi-discrete momentum equation

q'' wall heat flux

R universal gas constant

R_e^i interfacial heat transfer resistance

R_{FR} fouling thermal resistance

R_{gas} gas constant of water

r_o inlet film height on cylindrical wall

r_{wall} outer radius of cylinder

Re Reynolds number

Re_c critical Reynolds number

$\dot{S}_{m,c}$ rate of species depletion

$\dot{S}_{m,e}$ rate of species enrichment

$\dot{S}_{q,c}$ heat sink from species depletion

$\dot{S}_{q,e}$ heat sink from evaporation

$\dot{S}_v$ volumetric rate of liquid vaporization

$\mathbf{S}$ outward normal surface area vector

S_ϕ source term in generic transport equation

T transpose operator

$\triangle T_{\mathrm{BPR}}$ boiling point rise

T temperature

T_{ref} reference temperature for density calculation due to buoyancy effect

T_{sat} saturation temperature

T_i interface temperature

T_w wall temperature

$u_{_N}$ Nusselt velocity

u_w free surface wave speed

$\boldsymbol{v}$ velocity

$\boldsymbol{v}_{_r}$ phase relative velocity

V volume of control cell

We Weber number

α phase volume fraction / indicator function

β inclination angle between the free surface plane and horizontal

δ film thickness

δ_{I} delta function at interface

$\delta_{_N}$ Nusselt film thickness

ϵ amplitude of perturbation

η_e interfacial vaporization heat transfer coefficient

Γ liquid circulation

γ specific weight of liquid

κ mean curvature of interface

Λ diffusivity in generic transport equation

λ thermal diffusivity

μ dynamic viscosity

ν kinematic viscosity

ω_f central difference face interpolation function

ω_s stabilization constant

Φ coefficient of volume expansion for water

ϕ scalar variable in generic transport equation

Ψ volumetric flux in modified discrete phase equation

ψ_e evaporation coefficient

Ψ_{r_b} relative volumetric flux in modified discrete phase equation

ρ density

ρ_{ref} density at T_{ref}

σ surface tension coefficient

τ_w wall shear stress

$\boldsymbol{\phi}$ vector of unknowns in generic transport linear system

$\boldsymbol{\tau}$ rate of strain tensor

χ species mass fraction

SUMMARY

A computational model is developed to investigate fundamental flow physics and transport phenomena of evaporating wavy-laminar falling liquid films of water and black liquor[1]. The computational model is formulated from first principles based on the conservation laws for mass, momentum, energy and species in addition to a phase transport equation for capturing interface deformation and evolution. Free surface waves are generated by monochromatic perturbation of velocity. Continuum models for interfacial evaporation define source terms for liquid vaporization and species enrichment in the conservation laws. A phenomenological crystallization model is derived to account for species depletion due to salt precipitation during black liquor falling film evaporation.

Using highly resolved numerical grids on parallel computers, the computational model is implemented to analyze the dynamics of backflow (capillary separation eddies) in low Reynolds number falling films, investigate the dominant mechanisms of heat transfer enhancement in falling films at moderately high Reynolds numbers and study the fundamental wave structures and wave induced transport in black liquor falling films on flat and cylindrical walls. Validation of numerical simulations using analytical results and experimental correlations for wavy falling liquid film flows show that the computational model and numerical implementation predicts with sufficiently high accuracy falling film properties such as phase speed, wave height, evaporation heat transfer coefficient and average species concentration at evaporator exit.

[1]Black liquor is a highly viscous shear-thinning liquid produced from Kraft pulping of wood. It is a mixture of organics such as lignin, cellulose and dissolved inorganic salts (Chen & Gao, 2003) containing about 50% of energy content of pulped wood.

Simulation results from low Reynolds number falling films indicate that flow circulation (backflow) is not only limited to the solitary-capillary wave regime, but also occurs in film flow regions with sinusoidal waves. A theory based on the dynamics of the streamwise pressure gradient is proposed to explain interfacial waves interaction that give rise to multiple backflow regions observed in films dominated by solitary-capillary waves. Results from simulations of moderately high Reynolds number falling film evaporation presents new insight into heat transfer enhancement due to formation of an intermediate wave type. The reduction in film thickness at the intermediate wavefront results in relatively lower conduction thermal resistance and higher crosswise convective transport. Interfacial phenomena such as wave-breaking and vapor entrainment observed in experimental studies of black liquor falling films is qualitatively reproduced in the simulations. The evolution of secondary instabilities and corresponding force imbalances that give rise to these phenomena is analyzed. For an evaporating black liquor falling film, numerical predictions of the influence of wave induced transport on soluble salt crystallization and fouling is discussed.

CHAPTER 1

INTRODUCTION

1.1 Research Objectives

The primary aim of this research study is to investigate in detail the flow physics and transport phenomena associated with falling liquid film evaporation. The study focuses on wavy laminar falling films of water and black liquor. Conventional black liquor evaporation is characterized by high rates of soluble scale fouling resulting from precipitation of dissolved black liquor salts on heat transfer surface. Soluble scaling is a concentration and temperature dependent process and for black liquor in particular, the inverse-solubility[2] property makes temperature a critical scaling parameter. In recent times, high energy costs and strict environmental regulatory demands require concentration of black liquor to higher mass fractions of dissolved solids to ensure efficient combustion of the thickened liquor. At high dissolved solids mass fractions, black liquor evaporator scaling becomes erratic and less predictable with rapid fouling of heat transfer surface leading eventually to evaporator shut down (Frederick Jr. *et al.*, 2004).

Falling film evaporation is characterized by high rates of heat transfer and shorter residence time of the process stream, thus making it more suitable for black liquor concentration/evaporation. Nevertheless, with liquors at high dissolved solids mass fraction, its performance still suffers from rapid heat transfer surface fouling albeit to lesser degrees. Studies have shown that soluble scale deposition in high solids black liquor evaporators is controlled by crystallization phenomena, and the influence

[2]Inverse solubility is the phenomenon in which a material becomes less soluble in water as the temperature of the solution increases.

of fluid flow and heat transfer associated with the crystallization and evaporation processes (Frederick Jr. *et al.*, 2004). Extensive experimental research effort has been dedicated to study kinetics of soluble salts that crystallize during black liquor evaporation. However, relatively little information has been reported about the hydrodynamics and transport phenomena of black liquor falling films and their influence on the crystallization process. More importantly, since falling liquid film free surface deformation significantly influence film transport and consequently the temperature and concentration fields, thorough understanding of the soluble scaling process is incomplete without accurate prediction of falling film flow field and interfacial evolution.

This research seeks to develop a computational framework for detailed investigation of falling film flow and transport based on numerical solution of the conservation laws. For constant property liquid, the study investigates the influence of different interfacial wave regimes on falling film hydrodynamics and streamwise thermal regions that evolve in the liquid film due to interfacial deformation. The impact of wave dynamics on evaporation heat transfer enhancement is also analyzed. The computational model is applied to study falling film evaporation of black liquor mixture with dissolved species enrichement and depletion respectively evaluated based on liquid vaporization and soluble salt crystallization.

1.2 Specific Aims

Specifically, this research aims to:

1. investigate the dynamics and effects of capillary separation vortices for growing and saturated disturbances in the sinusoidal and solitary wave regimes of laminar falling liquid film.

2. analyze the distinct streamwise thermal regions that evolve in laminar falling

liquid film as a consequence of interfacial deformation with emphasis on identifying the dominant mechanism enhancing transport in each region.

3. characterize the structure of saturated black liquor interfacial waves and the free surface wave dynamics that give rise to wave-breaking and vapor entrainment in black liquor falling film.

4. analyze the influence of wavy falling film hydrodynamics on transport, salt crystallization and soluble scaling during black liquor evaporation.

To achieve these objectives, the study conducts numerical simulations over a wide range of flow and heating conditions for falling films of water and black liquor on highly resolved numerical grids using parallel computers. Extensive validation of the computational model and numerical implementation is done by comparing simulation results with known analytical solutions, reported experimental measurements and empirical correlations in the literature.

1.3 Motivation

For many industrial processes, the flow of a wavy thin liquid film down a vertical or inclined surface is central to unit operations involving heat and mass transfer e.g. film evaporation and concentration, gas absorption in wetted columns, film cooling etc. For some applications, the process fluid is a simple liquid with readily defined flow fields. For others, the liquid could be a highly viscous non-Newtonian polymeric solution where the corresponding flow field is characterized by irregular or complex interfacial flow structures. It is well reported in the literature that transport of heat or species in falling liquid films is fundamentally influenced by the presence of free surface waves (see for example Kutateladze & Gogonin, 1979; Jayanti & Hewitt, 1995; Miyara, 1999). However, the exact theory describing the mechanism of transport enhancement particularly for falling film flows with irregular interfacial structures is

still not fully established.

Numerical solution of the Navier-Stokes equations coupled with conservation laws for energy and species transport on well resolved grids provide a framework for closer investigation of the hydrodynamics and mechanisms of transport in thin liquid film flows. Results from this study are of primary relevance to processes applications where in-depth knowledge of falling film transport phenomena is necessary for the design of environmentally friendly, cost effective and functionally optimal heat and mass transfer devices and equipment. Specifically, the simulation and analysis of black liquor falling film evaporation with species enrichment/depletion is intended to serve as framework for studying more complex evaporation induced mass transfer phenomena such as evaporator heat transfer surface fouling and bulk flow crystallization associated with the evaporation of non-simple liquid mixtures with complex interfacial flow structures.

1.4 Falling Liquid Films

1.4.1 Literature Review

Falling liquid films are unstable to long wavelength disturbances (Yih, 1963) when the flow Reynolds number Re exceeds the often cited critical value $Re_c = (5/4)\cot\beta$, β is the inclination angle between the plane of the free surface and the horizontal. In his review, Chang (1994) describes distinct wave regimes for the evolution of naturally excited and forced disturbances on a laminar falling liquid film. Near the inlet, the waves are short and periodic and linear stability theory predicts exponential growth of disturbance. For monochromatic disturbances, the emerging wave inherits the forcing frequency. In contrast, natural noise driven waves assume a non regular structure consisting of a complex array of large and small waves moving over a substrate (Luan & Balakotaiah, 2000). As the wave amplitude grows downstream, linear stability theory ceases to apply and nonlinear effects arrest the amplification process. The

amplitude of the wave saturates to a finite value depending on Reynolds number and the fluid Kapitza number. A consequence of nonlinear interaction is the steepening of the sinusoidal shape of the emerging wave. Further downstream, subharmonic and characteristic sideband instabilities result in coalescence of neighboring waves at intermittent locations. Within these locations, the distorted waves evolve into localized teardrop humps (Chang, 1994). The humps have steep fronts which are preceded by a series of front running capillary waves. These solitary humps travel in a non-stationary manner but essentially retain their shapes. Eventually, transverse variations in wave profile gradually sets in.

Experimental analysis of wave evolution on falling films was pioneered by Kapitza & Kapitza (1964). They generated surface waves by imposing controlled disturbances (pressure pulses) on the falling film and then derived wave profiles by observing shadows of the film. Subsequent experimental studies (Chu & Dukler, 1974, 1975; Pierson & Whitaker, 1977; Karapantsios *et al.*, 1989; Alekseenko *et al.*, 1985) focused on direct observation and measurement of surface wave shape and characteristics using different measurement techniques to generate data describing falling film surface waves. Nakoryakov *et al.* (1976) studied two dimensional waves on water films and measured wave characteristics parameters such as phase velocities, wave separations and wave peak heights. The experimental studies of Nosoko *et al.* (1995) resulted in non-dimensional correlations for predicting phase velocities, wave separations and wave peak heights as functions of the flow Reynolds number and a physical properties group $K_{_F} = \rho_l^3 \nu_l^4 g/\sigma^3$.

Early theoretical investigations of hydrodynamic instabilities on falling film flows started with linear stability analysis based on the Orr-Sommerfeld equation. Approximate solutions to the equations were obtained by Benjamin (1957) and Yih (1963) specifying critical values beyond which falling film flows become unstable. Linear stability theory is however valid only at the inception of small amplitude waves, failing to

predict the form of the disturbance downstream. Benney (1966) derived a simplified equation for the instantaneous film height using the film parameter (defined as the ratio of height to wavelength for the wave) in a perturbation style expansion of the momentum equations for low Reynolds number flows. This equation is referred to as the Long Wave (LW) equation in the literature. The weakly nonlinear form of LW is based on the assumption of small amplitude waves. This simplification permits a truncation of the LW expansion yielding the Kuramoto-Sivashinsky (KS) equation. Sivashinsky & Michelson (1980) conducted numerical studies on the KS equation. Their results show that solitary waves generated in a bounded domain with periodic boundary conditions travel at speeds similar to those predicted by linear theory.

The integral boundary layer (IBL) type analysis derives from a simplification of the Navier-Stokes equations based on boundary layer type assumptions. By assuming a self-similar solution for the velocity profile, Shkadov (1967, 1968) derived a two-equation model for the dynamics of free surface waves from the IBL equations. These equations unlike the LW equations are not restricted to short amplitude waves only. Alekseenko *et al.* (1985) showed through experimental measurements that the local velocity profile in the falling film is not self-similar but parabolic. Tsvelodub & Trifonov (1992) succeeded in constructing stationary waves on a moving frame by solving the simplified equations with periodic boundary conditions. Chang *et al.* (1993) also constructed free surface waves by solving the boundary-layer type equations without specifying a velocity profile for the flow. The constructed waves showed reasonable agreement with experimental observations. Whereas previous experimental studies and predictions from the simplified equations provide fundamental understanding of falling film surface wave evolution, they fall short of an established theory explaining film transport enhancement as a consequence interfacial waves.

Numerical solutions of the complete Navier-Stokes equations for falling film flows have been implemented by several researchers (see for example Kheshgi & Scriven,

1987; Ho & Patera, 1990; Malamataris & Papanastasiou, 1991; Salamon *et al.*, 1994; Ramaswamy *et al.*, 1996; Miyara, 2000; Gao *et al.*, 2003; Kunugi & Kino, 2005; Dietze *et al.*, 2008, 2009). Typical challenges for such simulations include correct implementation of flow boundary conditions on the evolving interface and resolving the different length scales for film thickness and flow domain. Malamataris & Papanastasiou (1991) solved the equations in a truncated domain using modified outflow boundary conditions. Ho & Patera (1990), Salamon *et al.* (1994) and Ramaswamy *et al.* (1996) imposed the conservation of mean film thickness constraint on the flow using periodic boundary conditions with initial spatial waves on the films. Kheshgi & Scriven (1987) used the Lagrangian finite element method and compared with the Orr-Sommerfeld linear stability results. Ramaswamy *et al.* (1996) used the Arbitrary Eulerian-Lagrangian method which requires careful selection of grid velocity to handle large deformations. Salamon *et al.* (1994) compared results with the approximated long wave and boundary layer theories. Miyara (2000) solved the Navier-Stokes equations using finite difference in 2-D for the velocity distribution and free surface dynamics using a method based on the MAC algorithm. Gao *et al.* (2003) and Dietze *et al.* (2008, 2009) simulated 2-D falling film flow on a vertical plane by solving the complete equations using finite volume discretization with the Volume of Fluid (VOF) (Hirt & Nichols, 1981) interface capturing method . They accounted for surface tension effects at the interface using the Continuum Surface Force (CSF) model proposed by Brackbill *et al.* (1992). Miyara (2000), Gao *et al.* (2003) and Dietze *et al.* (2008, 2009) generated flow disturbances by imposing monochromatic perturbation of velocity at the inlet.

1.4.2 Falling Film Parameters

In this section we present the relevant parameters for characterizing falling film flow and transport. The parameters are evaluated using properties of the liquid which is

indicated by the subscript l.

(a) *Nusselt Film Velocity and Thickness*

Nusselt (1916) derived expressions for the average velocity and film thickness of a fully develop falling film in terms of film Reynolds number and properties of the liquid following his classical analysis of falling film condensation. The analysis makes the assumption of a flat free surface. For a specified flow Reynolds number Re, the Nusselt film velocity $u_{_N}$ and thickness $\delta_{_N}$ are evaluated as:

$$u_{_N} = \left(\frac{Re^2 \mu_l g}{3\rho_l}\right)^{\frac{1}{3}} \tag{1.1a}$$

$$\delta_{_N} = \left(\frac{3Re\mu_{_l}^2}{\rho_{_l}^2 g}\right)^{\frac{1}{3}} \tag{1.1b}$$

ρ_l and μ_l are the respective density and dynamic viscosity of the liquid, g is gravitational acceleration.

(b) *Film Reynolds Number*

The Reynolds number measures the importance of inertia relative to viscous effects. Convention in the literature prescribes two ways for calculating falling film Reynolds number:

$$Re = \frac{\rho_l \delta_{_N} u_{_N}}{\mu_l} \tag{1.2a}$$

$$Re = \frac{4\Gamma}{\mu_l} \tag{1.2b}$$

Γ is liquid flow circulation. Equation 1.2a is predominantly used in this study.

(c) *Weber Number*

The Weber and Reynolds numbers are the non-dimensional groups that emerge from the natural scaling of the Navier-Stokes equations for constant property falling liquid film. The Weber number measures the importance of surface tension relative to inertial effects and is evaluated in terms of the Nusselt film parameters:

$$We = \frac{\sigma}{\rho_l \delta_{_N} u_{_N}^2} \tag{1.3}$$

σ is surface tension coefficient.

(d) *Kapitza Number*

The Kapitza number is a function of only the liquid properties and not the flow rate. It can be calculated from either the Weber number or the liquid properties as follows:

$$Ka = \frac{\sigma}{\rho_l \nu_l^{4/3} g^{1/3}} \tag{1.4a}$$

$$Ka = \frac{We\, Re^{5/3}}{3^{1/3}} \tag{1.4b}$$

ν_l is liquid kinematic viscosity.

(e) *Viscous Length Scale*

The viscous length scale is a measure of the crosswise distance where diffusive transport dominates in the liquid film. It is evaluated as:

$$l_v = \left(\frac{\nu_l^2}{g}\right)^{1/3} \tag{1.5}$$

(f) *Nusselt Number*

Nusselt number measures the relative importance of convection heat transfer compared to conduction in the liquid film.

$$Nu = \frac{h\, l_v}{k_l} \tag{1.6}$$

k_l is liquid thermal conductivity.

(g) *Prandtl Number*

The Prandtl number is a measure of the ratio of momentum diffusion to thermal diffusion in the liquid film.

$$Pr = \frac{c_{pl}\mu_l}{k_l} \tag{1.7}$$

c_{pl} is liquid specific heat capacity.

1.5 Thesis Outline

Chapter 1 gives an introduction of the thesis topic and outlines the motivation for this research work. The literature review on falling liquid film is presented.

Chapter 2 describes the formulation of the mathematical model for the flow field and interface capturing methodology of a constant property falling liquid film.

Chapter 3 describes the finite volume discretization of the computation domain, momentum equations and a generic scalar transport equation. An overview of the Pressure Implicit with Splitting of Operators (PISO) algorithm is presented.

Chapter 4 analyzes the evolution and dynamics of backflow for sinusoidal and solitary-capillary wave regimes of laminar falling liquid films.

Chapter 5 presents analysis of free surface evaporation for wavy-laminar falling liquid films at moderately high Reynolds numbers.

Chapter 6 discusses simulation results for falling film evaporation of black liquor with emphasis on interfacial wave structure and wave induced transport.

Chapter 7 concludes with fundamental findings from this research study and recommendations for future work.

CHAPTER 2

METHODOLOGY

The computational methodology employed in this research study is based on the finite volume discretization and iterative solution of the conservation laws for 2-D (flat plate) and 3-D (cylindrical wall) falling film flow and transport. In this chapter, the formulation of the modeling equations for the two-phase hydrodynamics of a constant property falling liquid film down a vertical wall is presented. Conservation laws for heat and species transport with phase-change source terms are presented in subsequent chapters where falling film evaporation with species enrichment is analyzed. The numerical discretization method and solution algorithm for the discretized system of equations are discussed in chapter 3.

2.1 Mathematical Model

We consider the wavy-laminar flow of a liquid film down a vertical plane as shown in Figure 2.1. Adjacent to the wall, the liquid film flows under the influence of gravity with a well defined interface. Far form the interface, the film is bound by a quiescent gaseous phase. The simultaneous flow of the two immiscible, incompressible fluids is described by the Navier-Stokes equations using the single-field representation with interface evolution modeled using the well established Volume of Fluid (VOF) method (Hirt & Nichols, 1981). In this formulation, one set of conservation equations is written for the whole flow field where material properties are in general discontinuous across the interfacial boundary. The fluids are identified by a step function which represents the local volume fraction of each fluid. The step function is assigned a value of 1 in one particular fluid and 0 elsewhere. The "mixture" (which is understood to be the composite fluid formed by the two immiscible fluids within the flow

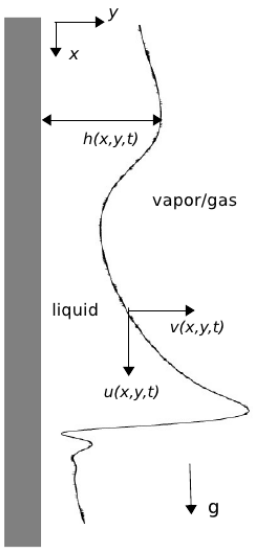

Figure 2.1: Schematic diagram of a wavy falling film: u, v are x, y velocity components, h is wave height and $\mathbf{g}$ is gravitational acceleration.

region) transport properties are written as combination of the volume fraction and the individual fluid properties.

2.1.1 Navier-Stokes Equations

The conservation equations in the single-field representation must account for differences in material properties of individual fluids as well as surface tension acting at the interface. For the entire flow field, the continuity and momentum equations are expressed as:

$$\frac{\partial \rho}{\partial t} + \boldsymbol{\nabla} \cdot (\rho \boldsymbol{v}) = 0 \tag{2.1a}$$

$$\frac{\partial \rho \boldsymbol{v}}{\partial t} + \boldsymbol{\nabla} \cdot (\rho \boldsymbol{v}\boldsymbol{v}) = -\boldsymbol{\nabla} p + \boldsymbol{\nabla} \cdot \boldsymbol{\tau} + \rho \mathbf{g} + \int_{A_\mathrm{I}(t)} \sigma \kappa' \boldsymbol{n}' \delta_\mathrm{I}(\boldsymbol{x} - \boldsymbol{x}') \, \mathrm{d}A_\mathrm{I} \tag{2.1b}$$

where $\boldsymbol{v}$ is velocity, $\boldsymbol{\tau}$ is the rate of strain tensor, p is pressure. The last term in equation (2.1b) represents the source of momentum due to surface tension effects. It only acts at the interface as indicated by the integral of a delta function $\delta_\mathrm{I}(\boldsymbol{x})$ over the interfacial area $A_\mathrm{I}(t)$. In this term, σ is the surface tension coefficient, κ' and $\boldsymbol{n}'$ are the respective curvature and unit normal vector at the interface. The stress

tensor $\boldsymbol{\tau}$ is expressed as:

$$\boldsymbol{\tau} = \mu(\boldsymbol{\nabla v} + \boldsymbol{\nabla v}^{\mathrm{T}}) \tag{2.2}$$

where μ is the dynamic viscosity of the "mixture" and $\boldsymbol{\nabla v}^{\mathrm{T}}$ is the transpose of the gradient of velocity vector. For ease of numerical implementation, the viscous term in equation (2.1b) is reformulated as follows:

$$\begin{aligned}
\boldsymbol{\nabla} \cdot \boldsymbol{\tau} &= \boldsymbol{\nabla} \cdot \left[\mu(\boldsymbol{\nabla v} + \boldsymbol{\nabla v}^{\mathrm{T}})\right] \\
&= \boldsymbol{\nabla} \cdot (\mu \boldsymbol{\nabla v}) + \boldsymbol{\nabla} \cdot (\mu \boldsymbol{\nabla v}^{\mathrm{T}}) \\
&= \boldsymbol{\nabla} \cdot (\mu \boldsymbol{\nabla v}) + (\boldsymbol{\nabla v}) \cdot (\boldsymbol{\nabla} \mu) + \mu \boldsymbol{\nabla} (\boldsymbol{\nabla} \cdot \boldsymbol{v}) \\
&= \boldsymbol{\nabla} \cdot (\mu \boldsymbol{\nabla v}) + (\boldsymbol{\nabla v}) \cdot \boldsymbol{\nabla} \mu
\end{aligned} \tag{2.3}$$

2.1.2 Interface Evolution (VOF)

The interface-capturing methodology employs the volume fraction α as an indicator function to mark the different fluids. In general, the interface is not a sharply defined boundary, rather an infinitesimal transition region exists where the fluid indicator function varies smoothly. The indicator function is defined as:

$$\alpha = \begin{cases} 1 & \text{for a point inside liquid} \\ 0 < \alpha < 1 & \text{for a point in the transition (interfacial) region} \\ 0 & \text{for a point inside gas/vapor} \end{cases} \tag{2.4}$$

The phase volume fraction α propagates as a Lagrangian invariant based on the prescribed flow field. Thus the transport of α can be defined as:

$$\frac{\partial \alpha}{\partial t} + \boldsymbol{\nabla} \cdot (\boldsymbol{v}\alpha) = 0 \tag{2.5}$$

Using the indicator function, the local fluid properties of the "mixture" are evaluated as:

$$\rho = \alpha \rho_l + (1 - \alpha)\rho_g \tag{2.6a}$$

$$\mu = \alpha \mu_l + (1 - \alpha)\mu_g \tag{2.6b}$$

where subscripts l and g indicate liquid and gas/vapor respectively.

The surface integral in equation (2.1b) representing momentum source from surface tension is converted into a volume force using the phase volume fraction field α and the Continuum Surface Force (CSF) model proposed by Brackbill *et al.* (1992):

$$\int_{A_{\mathrm{I}}(t)} \sigma\kappa' \boldsymbol{n}' \delta(\boldsymbol{x} - \boldsymbol{x}') \, \mathrm{d}A_{\mathrm{I}} \;\approx\; \sigma\kappa \boldsymbol{\nabla}\alpha \tag{2.7}$$

with interface mean curvature κ given by

$$\kappa \;=\; -\boldsymbol{\nabla} \cdot \left(\frac{\boldsymbol{\nabla}\alpha}{|\boldsymbol{\nabla}\alpha|} \right) \tag{2.8}$$

2.1.3 Modified VOF Equation

To ensure boundedness and conservation of the phase fraction, a modified version of equation (2.5) is derived by considering a two-fluid formulation of the conventional VOF model (Cerne *et al.*, 2001; Berberovic *et al.*, 2009). The modified equation contains an additional convective term obtained by expressing the velocity field in terms of a weighted average of the individual phase velocities. The derivation of the modified VOF method starts with the two-fluid Eulerian model for two-phase flow where the following evolution equations are solved for the individual phases:

$$\frac{\partial \alpha}{\partial t} + \boldsymbol{\nabla} \cdot (\boldsymbol{v}_{_l} \alpha) = 0 \tag{2.9a}$$

$$\frac{\partial (1-\alpha)}{\partial t} + \boldsymbol{\nabla} \cdot [\boldsymbol{v}_{_g} (1-\alpha)] = 0 \tag{2.9b}$$

subscripts l and g represent liquid and gas phases respectively. Equations (2.9a) and (2.9b) indicate that individual phases propagate at their corresponding phase velocities. It follows therefore that the interface can be assumed to propagate at a weighted velocity expressed as:

$$\boldsymbol{v} \;=\; \alpha \boldsymbol{v}_{_l} + (1-\alpha) \boldsymbol{v}_{_g} \tag{2.10}$$

Equation (2.9a) for the propagation of the liquid phase fraction can be re-written in terms of the individual liquid and vapor phase velocities as follows:

$$
\begin{aligned}
\frac{\partial \alpha}{\partial t} + \boldsymbol{\nabla} \cdot [\boldsymbol{v}_{_l} \alpha + \underbrace{\alpha(\boldsymbol{v}_{_l}\alpha) - \alpha(\boldsymbol{v}_{_l}\alpha)}_{=0}] + \boldsymbol{\nabla} \cdot [\underbrace{\alpha(1-\alpha)\boldsymbol{v}_{_g} - \alpha(1-\alpha)\boldsymbol{v}_{_g}}_{=0}] &= 0 \\
\frac{\partial \alpha}{\partial t} + \boldsymbol{\nabla} \cdot [\alpha(\boldsymbol{v}_{_l}\alpha) + \alpha(1-\alpha)\boldsymbol{v}_{_l}] + \boldsymbol{\nabla} \cdot [\alpha(1-\alpha)\boldsymbol{v}_{_g}] - \boldsymbol{\nabla} \cdot [\alpha(1-\alpha)\boldsymbol{v}_{_g}] &= 0 \\
\frac{\partial \alpha}{\partial t} + \boldsymbol{\nabla} \cdot [\alpha(\boldsymbol{v}_{_l}\alpha)] + \boldsymbol{\nabla} \cdot [\alpha(1-\alpha)\boldsymbol{v}_{_l}] + \boldsymbol{\nabla} \cdot [\alpha(1-\alpha)\boldsymbol{v}_{_g}] - \boldsymbol{\nabla} \cdot [\alpha(1-\alpha)\boldsymbol{v}_{_g}] &= 0 \\
\frac{\partial \alpha}{\partial t} + \boldsymbol{\nabla} \cdot [\alpha(\boldsymbol{v}_{_l}\alpha)] + \boldsymbol{\nabla} \cdot [\alpha(1-\alpha)\boldsymbol{v}_{_g}] + \boldsymbol{\nabla} \cdot [\alpha(1-\alpha)\boldsymbol{v}_{_l}] - \boldsymbol{\nabla} \cdot [\alpha(1-\alpha)\boldsymbol{v}_{_g}] &= 0 \\
\frac{\partial \alpha}{\partial t} + \boldsymbol{\nabla} \cdot [\alpha \underbrace{\{\alpha \boldsymbol{v}_{_l} + (1-\alpha)\boldsymbol{v}_{_g}\}}_{=\boldsymbol{v}}] + \boldsymbol{\nabla} \cdot [\underbrace{(\boldsymbol{v}_{_l} - \boldsymbol{v}_{_g})}_{=\boldsymbol{v}_r} \alpha(1-\alpha)] &= 0
\end{aligned}
\tag{2.11}
$$

$\boldsymbol{v}_{_r} = \boldsymbol{v}_{_l} - \boldsymbol{v}_{_g}$ is the phase relative velocity commonly referred to as the "*compression velocity*" (Berberovic *et al.*, 2009) in the literature. It vanishes everywhere except the phase boundary and its purpose is to keep the interface sharp and reduce numerical smearing.

The modified formulation for the propagation of α better captures the physics of the problem since it explicitly accounts for the contributions of individual fluid phases to the evolution of the interface. Different methods exist for constructing optimal values of $\boldsymbol{v}_r$ that result in well resolved phase boundaries. The relative velocity is typically treated as an explicit term and the numerical implementation employed in this study is discussed in § 3.1.4.

2.1.4 Modified Conservation Laws

Combining (2.3), (2.7) and (2.11), the resulting modified system of equations solved for the two-phase falling film flow field and free surface evolution can be expressed

as:

$$\frac{\partial \rho}{\partial t} + \boldsymbol{\nabla} \cdot (\rho \boldsymbol{v}) = 0 \tag{2.12a}$$

$$\frac{\partial \rho \boldsymbol{v}}{\partial t} + \boldsymbol{\nabla} \cdot (\rho \boldsymbol{v}\boldsymbol{v}) = -\boldsymbol{\nabla} p + \boldsymbol{\nabla} \cdot (\mu \boldsymbol{\nabla} \boldsymbol{v}) + (\boldsymbol{\nabla} \boldsymbol{v}) \cdot \boldsymbol{\nabla} \mu + \rho \mathbf{g} + \sigma \kappa \boldsymbol{\nabla} \alpha \tag{2.12b}$$

$$\frac{\partial \alpha}{\partial t} + \boldsymbol{\nabla} \cdot (\boldsymbol{v} \alpha) + \boldsymbol{\nabla} \cdot [\, \boldsymbol{v}_r \alpha (1 - \alpha) \,] = 0 \tag{2.12c}$$

In subsequent chapters where different aspects of falling film flows are analyzed, the corresponding governing equations would be presented in the original forms as specified in (2.1a), (2.1b) and (2.5).

2.1.5 Boundary and Initial Conditions

The boundary conditions presented in this section are for 2-D falling films over a flat plate. The conditions for 3-D falling films on a cylindrical wall are discussed in chapter 6 where simulation results for black liquor 3-D falling films are presented.

(a) *Inlet*

In this study, the falling liquid is assumed to be a fully developed flat film at the evaporator entrance. Consequently for a given Reynolds number, the film thickness and average velocity at the inlet are specified by Nusselt values (see § 1.4.2). To generate waves on the free surface, the inlet velocity is perturbed by a monochromatic time periodic function. In general, the inlet boundary consists of a liquid section defined by $x = 0,\ 0 \leq y \leq \delta_{_N}$ ($\delta_{_N}$ is Nusselt film thickness) with Dirichlet conditions and a vapor section defined by $x = 0$, $\delta_{_N} < y \leq 4\,\delta_{_N}$ where boundary conditions are prescribed based on flow conditions within the computation domain. At the liquid inlet $\alpha = 1$, while the streamwise velocity u_o is specified as a parabolic profile scaled by the Nusselt velocity with monochromatic perturbation (see Xu *et al.*, 2008):

$$u_o \;=\; \frac{3}{2}\left[2\left(\frac{y}{\delta_{_N}}\right) - \left(\frac{y}{\delta_{_N}}\right)^2\right][1 + \epsilon \sin(2\pi f t)]u_{_N} \tag{2.13}$$

where f is the forcing frequency in Hz, ϵ is the amplitude of perturbation which is set at $\epsilon = 0.05$ for this study. Gao *et al.* (2003) compared numerical results for $\epsilon = 0.03$ and $\epsilon = 0.05$ and concluded that the equilibrium wave shape is insensitive to the amplitude of forcing frequency. Along the boundary $x = 0$, $\delta_{_N} < y \leq 4\,\delta_{_N}$, $\alpha = 0$ with homogenous streamwise derivative for velocity.

(b) *Outlet*

Along the boundary $x = L_e$, $0 \leq y \leq 4\,\delta_{_N}$ (where L_e is streamwise length of the vertical wall) outflow boundary conditions are specified i.e. $\frac{\partial u}{\partial x} = \frac{\partial v}{\partial x} = 0$, $\frac{\partial \alpha}{\partial x} = 0$.

(c) *Wall*

At the wall (x, $y = 0$), no-slip conditions are imposed for velocity with zero-flux for the phase volume fraction i.e. $u = v = 0$, $\frac{\partial \alpha}{\partial y} = 0$. For the purpose of defining the computation domain, we impose a numerical boundary along the plane defined as $\forall x, y = 4\,\delta_{_N}$ where boundary conditions consistent for a wall (i.e. no-slip for velocity and zero flux for phase fraction) also apply.

(d) *Phase Boundary*

No boundary conditions are imposed explicitly at the interface since the entire flow domain is treated as a single fluid following the single-field representation. Surface tension effects are explicitly accounted for in the formulation of the momentum equations.

(e) *Initial Condition*

The film thickness within the flow domain at $t = 0$ is set to the unperturbed Nusselt flat film with velocity specified by values from Nusselt theory. For our simulations, we initialized pressure to zero everywhere in the computation domain.

CHAPTER 3

NUMERICAL METHOD

This chapter presents the numerical discretization methods and solution algorithms for the algebraic system of equations obtained from discretization of the conservation laws. The numerical solutions were implemented in OpenFOAM (OpenCFD, 2011).

3.1 Finite Volume Method

3.1.1 Domain Discretization

The computation domain is subdivided into a finite number of non-overlapping control volume cells (see figure 3.1) over which the governing equations are integrated. Each cell is bound by a finite number of cell faces. A face is internal if it is shared by two control cells or external if it represents a boundary of the domain on which a physical boundary condition is applied. Figure 3.2 shows parameters of a computational cell used in the finite volume discretization.

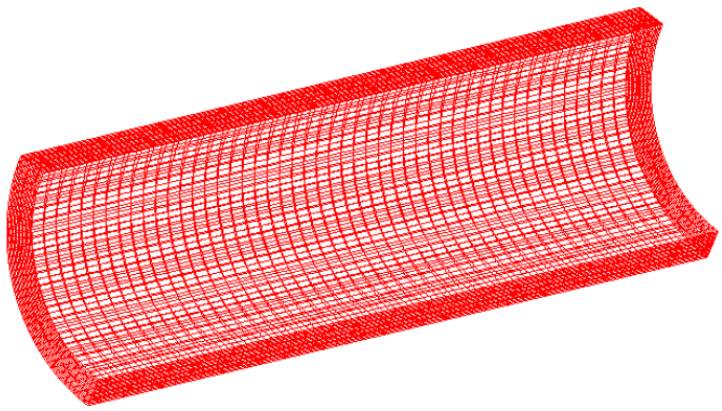

Figure 3.1: Section of cylindrical computational flow domain discretized using structured finite volume cells.

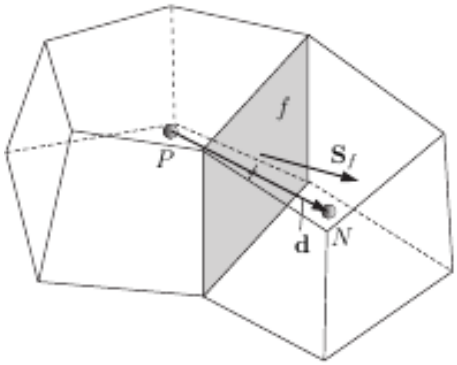

Figure 3.2: Parameters in finite volume discretization: P and N are the centroids of the cell and its neighbor respectively, $\mathbf{d}$ denotes the vector between P and N, S_f is the face-area vector of the face common to both cells (OpenCFD, 2011).

3.1.2 Discretization of Conservation Law

The finite volume discretization of the governing equations proceeds over a few steps. First the conservation laws are written as volume integrals over each control volume and subsequently converted to surface-integrated flux terms using Gauss's theorem. The surface integrals are evaluated by summation of fluxes over control volume cell faces. To determine the fluxes, cell face values of variables are estimated by interpolation using cell centered values at neighboring control cells. The following analysis presents the finite volume discretization for a generic transport equation. The same procedures apply to the terms in the heat and species conservation laws.

The standard conservation law for a generic scalar ϕ can be expressed as:

$$\underbrace{\frac{\partial \rho\phi}{\partial t}}_{\text{transient}} + \underbrace{\boldsymbol{\nabla}\cdot(\rho\boldsymbol{v}\phi)}_{\text{convection}} = \underbrace{\boldsymbol{\nabla}\cdot(\Lambda\boldsymbol{\nabla}\phi)}_{\text{diffusion}} + \underbrace{S_\phi}_{\text{source}} \tag{3.1}$$

where Λ is diffusivity and S_ϕ is a source term. The first step of the finite volume discretization of equation (3.1) over a time interval t, $t+\triangle t$ can be expressed as:

$$\int_t^{t+\triangle t}\left[\frac{\partial}{\partial t}\int_{V_P}\rho\phi\,\mathrm{d}V + \int_{V_P}\boldsymbol{\nabla}\cdot(\rho\boldsymbol{v}\phi)\,\mathrm{d}V\right]\mathrm{d}t = \int_t^{t+\triangle t}\left[\int_{V_P}\boldsymbol{\nabla}\cdot(\Lambda\boldsymbol{\nabla}\phi)\,\mathrm{d}V + \int_{V_P}S_\phi\,\mathrm{d}V\right]\mathrm{d}t \tag{3.2}$$

where V_P is the control volume over which the equation is integrated. The generalized Gauss's theorem applied to a volume integral can be expressed as:

$$\int_V \boldsymbol{\nabla} \otimes \phi \, \mathrm{d}V = \int_S \mathrm{d}\mathbf{S} \otimes \phi \tag{3.3}$$

where $\otimes$ denotes a generalized tensor operator e.g. inner product, and $\mathrm{d}\mathbf{S}$ is the differential of the outward normal surface area vector. The terms in equation (3.2) can be expressed in the form of equation (3.3). The numerical approximation of the right hand side of equation (3.3) for each term in the discretized scalar equation is presented in the following sections.

3.1.2.1 Transient Term

With the exception of the phase transport equation (3.22), the first order backward Euler method was implemented for all other time derivatives. The choice is motivated by the need for numerical stability and large computation time steps. For the transient term, a simple difference approximation is implemented as follows:

$$\int_{V_P} \frac{\partial \rho \phi}{\partial t} \, \mathrm{d}V \;\approx\; V_P \frac{\rho_P^n \phi_P^n - \rho_P^o \phi_P^o}{\triangle t} \tag{3.4}$$

where ϕ^o is the known variable value from the previous time step and ϕ^n is the unknown value at the current time step $t_n = n \triangle t$.

3.1.2.2 Gradient Term

Applying Gauss's theorem to the implicit discretization of the gradient term gives:

$$\int_V \boldsymbol{\nabla} \phi \, \mathrm{d}V \;=\; \int_S \mathrm{d}\mathbf{S} \, \phi \;\approx\; \sum_f \mathbf{S} \, \phi_f^n \tag{3.5}$$

where $\mathbf{S}$ is the outward normal surface area vector of the faces in the control cell and ϕ_f^n is the face-centered value of the variable. Since variables are typically stored at cell centers of control volumes, ϕ_f^n has to be evaluated by interpolation. In our simulations, the second order accurate Central Differencing (CD) scheme was implemented for face

interpolation. The scheme is expressed as (Ferziger & Peric, 2002):

$$\phi_f^n = \omega_f \phi_P^n + (1 - \omega_f)\phi_N^n \tag{3.6}$$

where

$$\omega_f = \frac{|\boldsymbol{x}_f - \boldsymbol{x}_N|}{|\boldsymbol{x}_f - \boldsymbol{x}_N| + |\boldsymbol{x}_f - \boldsymbol{x}_P|} \tag{3.7}$$

$\boldsymbol{x}_i$ is the position vector at point i.

3.1.2.3 Convection Term

For the generic scalar transport, the convection term is evaluated implicitly as:

$$\int_{V_P} \boldsymbol{\nabla} \cdot (\rho \boldsymbol{v} \phi)\, \mathrm{d}V \;=\; \int_S \mathrm{d}\mathbf{S} \cdot (\rho \boldsymbol{v} \phi) \;\approx\; \sum_f \mathbf{S} \cdot (\rho \boldsymbol{v})_f \, \phi_f^n \tag{3.8}$$

$(\rho \boldsymbol{v})_f$ is the mass flux at the control volume cell faces based on a known velocity field and ϕ_f^n is determined from equation (3.6).

3.1.2.4 Diffusion Term

The diffusion term is implicitly discretized as follows:

$$\int_{V_P} \boldsymbol{\nabla} \cdot (\Lambda \boldsymbol{\nabla} \phi)\, \mathrm{d}V \;=\; \int_S \mathrm{d}\mathbf{S} \cdot (\Lambda \boldsymbol{\nabla} \phi) \;\approx\; \sum_f \Lambda_f (\mathbf{S} \cdot \boldsymbol{\nabla}_f \phi^n) \tag{3.9}$$

where Λ_f is the diffusivity evaluated at the cell face and $\boldsymbol{\nabla}_f \phi^n$ is the face normal gradient of ϕ^n. A second order scheme for evaluating $\mathbf{S} \cdot \boldsymbol{\nabla}_f \phi^n$ at the cell face is expressed as:

$$\mathbf{S} \cdot \boldsymbol{\nabla}_f \phi^n \;=\; |\mathbf{S}| \frac{\phi_N^n - \phi_P^n}{|\mathbf{d}|} \tag{3.10}$$

3.1.2.5 Source Term

A second order scheme for discretizing the explicit source term is expressed as:

$$\int_{V_P} S_\phi \, \mathrm{d}V \;\approx\; S_P^o V_p \tag{3.11}$$

i.e. the source term is evaluated using the known variable value at the control volume center.

With respect to boundary cells, Dirichlet boundary conditions are treated as known fluxes at cell faces. Neumann conditions are evaluated in terms of variable values at adjacent cell centers using one-sided face normal derivates (see equation (3.10)). The resulting fluxes and explicit terms at control volumes with boundary faces are modified accordingly (see the following for a comprehensive discussion: Hrvoje, 1996; Rusche, 2002; Ferziger & Peric, 2002). Summation of all flux terms over the control volume results in the algebraic equation for the finite volume discretization at control volume P:

$$a_{_P}\phi^n_{_P} + \sum_N a_{_N}\phi^n_{_N} \;=\; b^o_{_P} \tag{3.12}$$

where $a_{_P}$ is the discretization coefficient of ϕ^n at cell P and the summation is over neighboring cells with respect to P. $b^o_{_P}$ contains all terms evaluated explicitly (e.g. terms from source, deferred correction, linearization etc using values from the previous time step) both at cell P and neighboring cells. Equation (3.12) written for each control volume in the computation domain results in an algebraic system for ϕ:

$$A\boldsymbol{\phi} = \boldsymbol{b} \tag{3.13}$$

where A is the coefficient matrix, $\boldsymbol{b}$ is the vector of explicit terms and $\boldsymbol{\phi}$ is the vector of unknowns. In general $A = A(\phi)$ and the system defined by equation (3.13) is solved iteratively.

3.1.3 Discretization of Navier-Stokes Equations

The modified system of equations solved for the two-phase flow field can be expressed as:

$$\frac{\partial \rho}{\partial t} + \boldsymbol{\nabla}\cdot(\rho\boldsymbol{v}) = 0 \tag{3.14a}$$

$$\frac{\partial \rho\boldsymbol{v}}{\partial t} + \boldsymbol{\nabla}\cdot(\rho\boldsymbol{v}\boldsymbol{v}) = -\boldsymbol{\nabla}p + \boldsymbol{\nabla}\cdot(\mu\boldsymbol{\nabla}\boldsymbol{v}) + (\boldsymbol{\nabla}\boldsymbol{v})\cdot\boldsymbol{\nabla}\mu + \rho\mathbf{g} + \sigma\kappa\boldsymbol{\nabla}\alpha \tag{3.14b}$$

Two issues of importance are the nonlinearity in the momentum equations and pressure-velocity coupling. Nonlinearity is handled by lagging a portion of the velocity (Thomas, 1995) i.e. for the convective terms, the mass flux at cell faces is evaluated using the most recent velocity field that satisfies the continuity constraint:

$$\int_{V_P} \boldsymbol{\nabla} \cdot (\rho \boldsymbol{v}\boldsymbol{v}) \approx \int_{V_P} \boldsymbol{\nabla} \cdot (\rho \boldsymbol{v}^o \boldsymbol{v}) \approx \sum_f \mathbf{S} \cdot (\rho \boldsymbol{v})_f^o \, \boldsymbol{v}_f \tag{3.15}$$

Applying finite volume discretization to equation (3.14b) with the lagged convection term i.e equation (3.15), and dividing through with the cell volume results in the semi-discretized momentum equations:

$$a_P \boldsymbol{v}_P = \boldsymbol{H}(\boldsymbol{v}) - \boldsymbol{\nabla} p \tag{3.16}$$

where

$$\boldsymbol{H}(\boldsymbol{v}) = -\sum_N a_N \boldsymbol{v}_N + \boldsymbol{q}_P^o + \frac{\rho_P^o \boldsymbol{v}_P^o}{\triangle t} \tag{3.17}$$

$\boldsymbol{q}_P^o$ represents source terms obtained from the explicit discretization of $\{(\boldsymbol{\nabla}\boldsymbol{v}) \cdot \boldsymbol{\nabla}\mu + \rho\mathbf{g} + \sigma\kappa\boldsymbol{\nabla}\alpha\}$ at cell P. Equation (3.16) is used to express the discrete velocity field as:

$$\boldsymbol{v}_P = \frac{\boldsymbol{H}(\boldsymbol{v})}{a_P} - \frac{1}{a_P}\boldsymbol{\nabla} p \tag{3.18}$$

Based on interpolation of cell centered values obtained from (3.18), the face flux is evaluated as:

$$(\rho \boldsymbol{v})_f = \left[\frac{\rho_P \boldsymbol{H}(\boldsymbol{v})}{a_P}\right]_f - \left[\frac{\rho_P}{a_P}\right]_f \left[\boldsymbol{\nabla} p\right]_f \tag{3.19}$$

The continuity constraint i.e. equation (3.14a) for a constant density fluid is discretized as:

$$\int_{V_P} \boldsymbol{\nabla} \cdot (\rho \boldsymbol{v}) \approx \sum_f \mathbf{S} \cdot (\rho \boldsymbol{v})_f = 0 \tag{3.20}$$

Combining equations (3.19) and (3.20), the discrete Pressure Poisson Equation is expressed as:

$$\sum_f \mathbf{S} \cdot \left[\left(\frac{\rho_P}{a_P}\right)_f (\boldsymbol{\nabla} p)_f\right] = \sum_f \mathbf{S} \cdot \left[\frac{\rho_P \boldsymbol{H}(\boldsymbol{v})}{a_P}\right]_f \tag{3.21}$$

The formulation of equation (3.21) ensures that the resulting face fluxes are conservative. The face normal gradient of the pressure term is evaluated using equation (3.5).

3.1.4 Discretization of Phase Equation

The modified phase volume fraction equation is expressed as:

$$\frac{\partial \alpha}{\partial t} + \boldsymbol{\nabla} \cdot (\boldsymbol{v}\alpha) + \boldsymbol{\nabla} \cdot [\, \boldsymbol{v}_r \alpha(1-\alpha)\,] = 0 \tag{3.22}$$

The semi-discrete equation obtained from the spatial discretization of equation (3.22) is expressed as (see for example Rusche, 2002):

$$\frac{\partial \alpha}{\partial t} + \sum_f \Psi \alpha_{f(\Psi,S)} + \sum_f \Psi_{r_b} \alpha_{f(\Psi_{r_b},S)} = 0 \tag{3.23}$$

where Ψ is the volumetric flux (i.e. $\mathbf{S}\cdot\boldsymbol{v}$) evaluated directly from fluxes in the pressure-velocity solution procedure to ensure conformity with the continuity constraint. $\Psi_{r_b} = (1-\alpha)_{f(\Psi_{r_b},S)} \Psi_r$, where Ψ_r is constructed so that compression acts perpendicular to the interface. In this study the compression flux is specified based on the maximum velocity magnitude in the transition region (Rusche, 2002):

$$\Psi_r = K_c \boldsymbol{n}^* \max \frac{|\boldsymbol{n}^* \Psi|}{|\mathbf{S}|^2} \tag{3.24}$$

where $K_c = 1.5$ is the adjustable coefficient that specifies the extent of compression and $\boldsymbol{n}^*$ is evaluated as:

$$\boldsymbol{n}^* = \frac{(\boldsymbol{\nabla}\alpha^*)_f}{|(\boldsymbol{\nabla}\alpha^*)_f| + \omega_s} \tag{3.25}$$

$\omega_s = 10^{-5}$ is a stabilization parameter that prevents division by zero and α^* is a smoothed function constructed from α by convolution (see Rusche, 2002).

3.2 PISO Algorithm

The steps in the Pressure Implicit with Splitting of Operators (PISO) algorithm for solving the momentum equations is outlined below (Hrvoje, 1996):

1. **Momentum Prediction**: an approximation of the velocity field is obtained by solving a modification of equation (3.16) using the last known pressure field:

$$a_P \boldsymbol{v}_P = \boldsymbol{H}(\boldsymbol{v}) - \sum_f \mathbf{S}\, p_f^o \tag{3.26}$$

2. **Pressure Solution**: The pressure equation is formulated by assembling the $\boldsymbol{H}(\boldsymbol{v})$ operator using the predicted velocity from the **Momentum Prediction** step. The solution of the pressure equation gives the first estimate of the new pressure field.

3. **Velocity Correction**: Explicit correction of velocity is done using the new pressure field determined from imposing the continuity constraint in the **Pressure Solution** step. The correction is done using equation (3.18).

This procedure is repeated iteratively until the tolerance between consecutive corrected velocity fields is satisfied at each time step.

3.3 Numerical Solution Sequence

The coupled system of equations are solved sequentially i.e. for the algebraic system resulting from discretization of a conservation law, the dominant variable is treated as the single unknown while other "variables" are evaluated explicitly using values from the last iteration. The symmetric system from the discrete pressure equation is solved using preconditioned conjugate gradient method. The discretized phase fraction equation is solved using an explicit time stepping scheme but with multiple solution cycles within a time step. All other discrete equations are solve using a preconditioned GMRES iterative solver. At a specified time step, the following numerical solution sequence is implemented:

- solve the momentum equations with the pressure field from the last iteration to obtain the intermediate velocity field

- using the PISO loop solve the discrete Pressure Poisson Equation for the current pressure field
- with the new pressure field, correct the predicted velocity field to satisfy the divergence-free condition
- solve the volume phase fraction equation
- solve the species conservation equation
- solve the energy equation

For falling film simulations with evaporation and net species enrichment, the source terms for the phase fraction, energy and species transport equations are evaluated immediately after the corresponding equation is solved i.e. evaporation source terms are evaluated after the energy transport equation is solved and crystallization source terms are evaluated after species transport equation is solved. This ensures that the sequential solution procedure uses the most recent variable field values for evaluating fluid transport properties dependent on flow variables e.g. temperature, species concentration or phase volume fraction.

CHAPTER 4

INTERFACIAL WAVES AND BACKFLOW DYNAMICS IN FALLING LIQUID FILMS

4.1 Background

For laminar falling films, Chang (1994) identifies distinct regimes for the evolution of disturbances on naturally excited and monochromatically perturbed flows. Nosoko & Miyara (2004) classified the dominant free surface waves on laminar films based on the frequency of flow perturbation. At low frequencies, solitary pulses similar to teardrop humps traveling on a thin substrate film are observed. These waves have steep fronts which are preceded by a series of front running capillary waves. At much higher disturbance frequencies, the free surface is dominated by sinusoidal waves characterized by an asymmetric shape. These waves have gentle wide peaks with sharp narrow valleys.

Laminar falling liquid film hydrodynamics have been studied numerically by Salamon *et al.* (1994); Jayanti & Hewitt (1995); Ramaswamy *et al.* (1996); Miyara (2000); Gao *et al.* (2003); Kunugi & Kino (2005); Dietze *et al.* (2008, 2009). Streamlines and velocity fields from simulations of Jayanti & Hewitt (1995), Miyara (2000) and Gao *et al.* (2003) show that circulation zones were formed in the middle of large amplitude sinusoidal and solitary waves. Kunugi & Kino (2005) observed separation vortices or backflow regions from velocity vector fields at the wave troughs in front of solitary-capillary waves. Dietze *et al.* (2008) confirmed by numerical simulation on highly resolved spatial and temporal grids the formation of backflow at the capillary wave region of low Reynolds number falling liquid films. Further confirmation of the backflow phenomenon was provided by Dietze *et al.* (2009) based on experimental studies

using laser doppler velocimetry (LDV) and particle image velocimetry (PIV).

Although circulation zones at different wave locations in laminar falling liquid films were observed by several earlier studies, Dietze *et al.* (2008, 2009) were the first to provide a mechanistic explanation of the backflow phenomenon. They show that backflow forms from a separation eddy that develops at the wall surface due to adverse pressure gradients in the capillary wave region. The adverse pressure gradient was a result of change in curvature of the free surface. Dietze *et al.* (2008) concluded that the dynamics of the backflow region is determined by the characteristics of the capillary waves which themselves are governed by the separation of the large wave humps they precede. Their results also indicate that transport is enhanced in the liquid film by relatively higher crosswise velocities in the backflow regions.

In this chapter, we employ highly resolved numerical grids to investigate the flow dynamics leading to formation and subsequent evolution of backflow regions for a growing interfacial disturbance. The analysis is conducted for both sinusoidal and solitary interfacial wave regimes of laminar 2-D falling liquid films (see figure 2.1) at low Reynolds numbers. The study investigates numerically if the formation of capillary separation vortices (backflow) is possible in falling liquid films without capillary waves. This has greater importance in falling film flow regions dominated by strictly sinusoidal interfacial waves (see for example Kapitza & Kapitza, 1964) where capillary waves are absent. For both sinusoidal and solitary-capillary waves, we analyze the dynamics of backflow regions after formation and investigate how backflow downstream propagation is influenced by the type of surrounding interfacial waves.

4.2 Mathematical Model

The governing equations for wavy-laminar falling film on a vertical wall without heat transfer is presented in § 2.1.1. A description of the computation domain and corresponding boundary and initial conditions are discussed in § 2.1.5.

4.3 Numerical Validation

The numerical implementation is validated based on comparisons of simulation results with correlations developed from experimental studies for falling film phase speed and maximum wave height by Nosoko *et al.* (1995), and experimentally determined time traces of liquid film streamwise velocity and free surface profile by Dietze *et al.* (2009).

4.3.1 Correlations for 2-D Falling Films

Nosoko *et al.* (1995) conducted falling liquid film experiments using water on a glass plate of dimensions $205 \times 245\,\mathrm{mm}^2$. The flow Reynolds numbers for the experiments were in the range $Re = 15 - 90$ with temperatures between $278 - 296\,\mathrm{K}$. Based on their experimental results, they proposed the following correlations for regularly spaced two-dimensional waves on water falling film:

$$N_{hp} = 0.49 K_{F}^{0.044} N_{L}^{0.39} Re^{0.46} \tag{4.1a}$$

$$N_{uw} = 1.13 K_{F}^{0.02} N_{L}^{0.31} Re^{0.37} \tag{4.1b}$$

where N_{hp} and N_{uw} are the non-dimensional maximum wave height and non-dimensional wave speed respectively, $K_{F} = \rho_{l}^{3} \nu_{l}^{4} g/\sigma^{3}$ is the non-dimensional physical properties group and $N_{L} = L(g/\nu_{l}^{2})^{1/3}$ is the non-dimensional wave separation calculated from the distance L between regularly-spaced 2-D waves.

Numerical simulations were conducted for the flow domain and conditions corresponding to the experiments by Nosoko *et al.* (1995). The length and width of the computation domain were respectively set at $700\delta_{N}$ and $4\delta_{N}$. The uniform mesh sizes were set at $\Delta x = 0.15\delta_{N}$ and $\Delta y = 0.03\delta_{N}$ in the streamwise and crosswise directions respectively. The time step was adaptively set based on the global CFL condition for the α equation. Typical values were in the range 1 - 10×10^{-6} s. Table 4.1 shows results for phase velocity u_{w}, maximum wave height h_{p} and wave separation L for simulated water falling film surface waves at different Reynolds numbers Re and forcing

Table 4.1: Wave properties of simulated water falling film

Re	f(Hz)	$u_w\,(\mathrm{ms}^{-1})$	h_p(m)	L(m)
20.1	27	0.24	0.000266	0.0076
20.1	45	0.27	0.000293	0.0118
69.0	30	0.41	0.000492	0.0148
69.0	45	0.35	0.000443	0.0092
69.0	70	0.33	0.000415	0.0064

frequencies f. Transport properties for the simulations were set at $\rho_l = 998.2\,\mathrm{kgm}^{-3}$, $\rho_g = 1.2\,\mathrm{kgm}^{-3}$, $\nu_l = 1 \times 10^{-6}\,\mathrm{m}^2\mathrm{s}^{-1}$, $\nu_g = 1.51 \times 10^{-5}\,\mathrm{m}^2\mathrm{s}^{-1}$, $\sigma = 0.073\,\mathrm{Nm}^{-1}$ and $g = 9.78\,\mathrm{ms}^{-2}$.

To compare simulated values with equations 4.1a and 4.1b, u_w and h_p are respectively non-dimensionalized using $N_{uw} = u_w/(\nu_l g)^{1/3}$ and $N_{hp} = h_p(g/\nu_l^2)^{1/3}$ (Nosoko *et al.*, 1995). Figure 4.1 shows plots of N_{hp} and N_{uw} from numerical simulations by Gao *et al.* (2003), Xu *et al.* (2008) and this study compared with equations (4.1a) and (4.1b). The results show good agreement both between this work and previously reported simulation results and the correlations. The $Re = 20.1$, $f = 27\,\mathrm{Hz}$ case corresponds to the seminal experiment conducted by Kapitza & Kapitza (1964) where the reported wave speed u_w was $0.22\,\mathrm{ms}^{-1}$ (Gao *et al.*, 2003).

4.3.2 2-D Falling Film Experiments

Dietze *et al.* (2009) conducted falling liquid film experiments and numerical simulations using an aqueous solution of dimethylsulfoxide (DMSO) at Reynolds number $Re = 15$, Kapitza number $Ka = 509$ and perturbation frequency $f = 16\,\mathrm{Hz}$. The transport properties of the DMSO solution were specified as: $\rho_l = 1098.3\,\mathrm{kgm}^{-3}$, $\nu_l = 2.85 \times 10^{-6}\,\mathrm{m}^2\mathrm{s}^{-1}$, $\sigma = 0.0484\,\mathrm{Nm}^{-1}$ at a temperature of 298.35 K. The gas phase was air with transport properties specified by atmospheric conditions at the liquid film temperature. Measurements of the liquid film height and streamwise velocity were sampled at a streamwise distance of 120 mm from the inlet where the

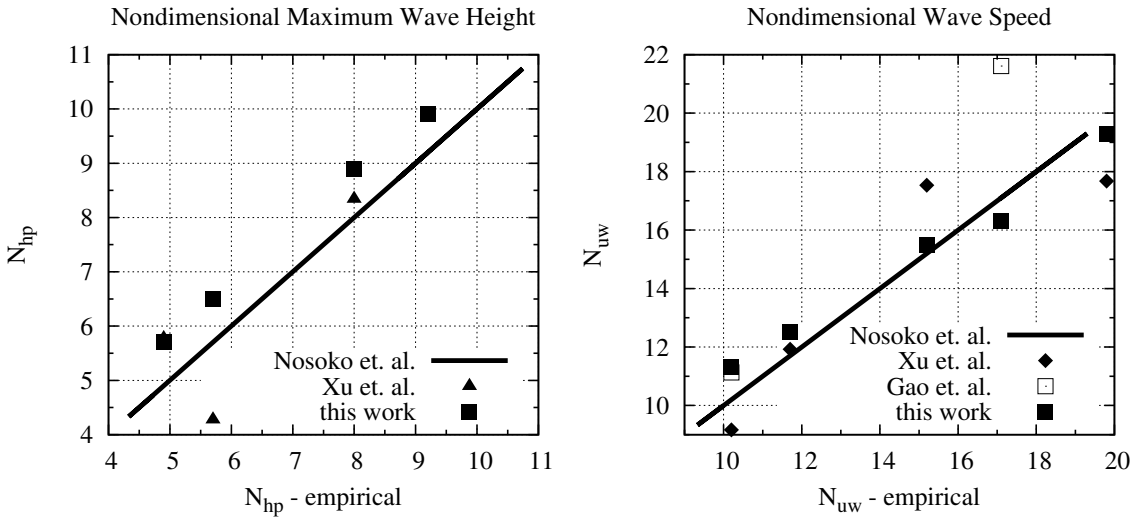

Figure 4.1: Simulated non-dimensional maximum wave height N_{hp} and non-dimensional wave speed N_{uw} for water falling films compared with Nosoko *et al.* (1995) correlations

experimental results show that the liquid film surface waves were fully developed. The streamwise velocity was measured at a distance of 0.12 mm from the wall. Figure 4.2 show results of their experimental measurements and numerical simulations for the conditions described above.

To further validate our numerical implementation, simulations were conducted for flow conditions and transport properties specified for the DMSO solution (Dietze *et al.*, 2009). Results from our simulations also show that the film free surface was characterized by fully developed 2-D waves at streamwise distance $x > 0.1$m from the inlet. Beyond this point the wave retained its shape and phase speed as it traveled downstream for the remaining portion of the computation domain. Figure 4.3 shows plots of the time traces of the wave profile and streamwise velocity sampled at a distance of 0.12 mm from the wall and 120 mm from the inlet. The plots in figures 4.2 and 4.3 show good agreement between our simulations and results reported by Dietze *et al.* (2009). Our simulation slightly under-predicts the maximum wave height of the liquid film which can be attributed to the different values of ϵ used in both studies. In

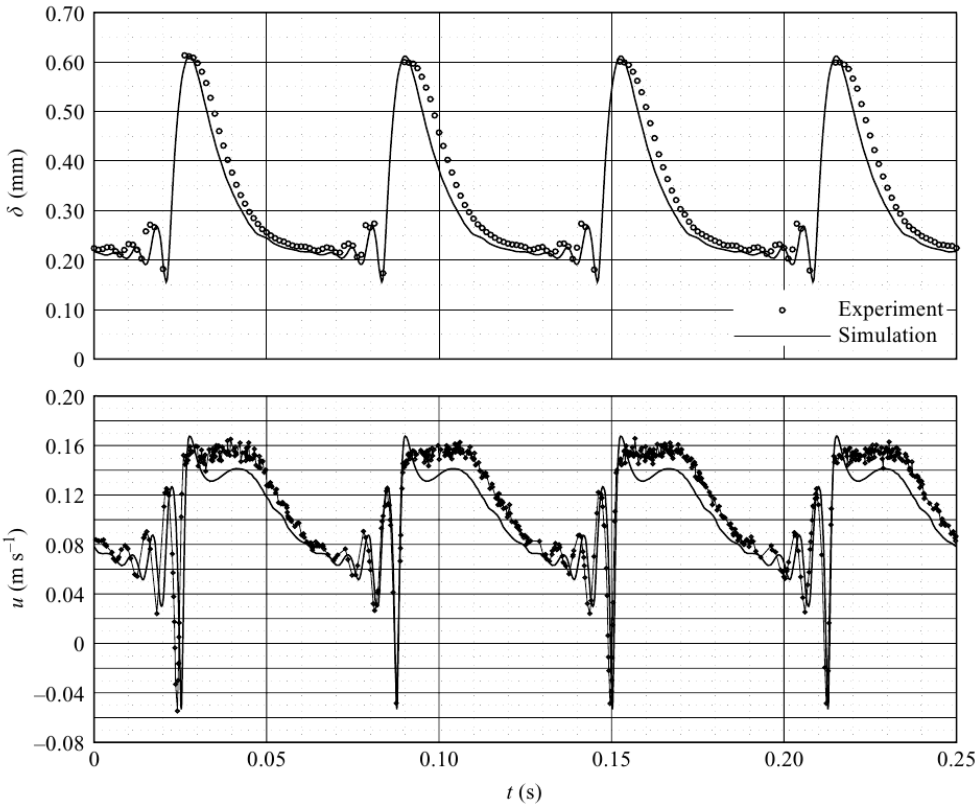

Figure 4.2: Comparison of numerical and experimental data by Dietze *et al.* (2009) for time traces of film thickness and streamwise velocity for $Re = 15$, $f = 16\,\text{Hz}$ and $y = 0.12\,\text{mm}$

.

our simulation, $\epsilon = 0.05$ was used while Dietze *et al.* (2009) does not report the value of ϵ used in their simulation. They however specified that the value of ϵ was adjusted so as to match the wave amplitude from their numerical results with experimental measurements.

4.4 Analysis of Simulation Results

4.4.1 Interfacial Waves and Backflow Evolution

Figure 4.4 shows free surface wave profiles of simulated water falling films at $Re = 69$ and forcing frequency f set at 30, 45, 70 and 110 Hz. The plots show the variation of free surface deformation with wavelength of inlet disturbance. Large amplitude solitary waves preceded by much smaller capillary waves are formed at low frequency

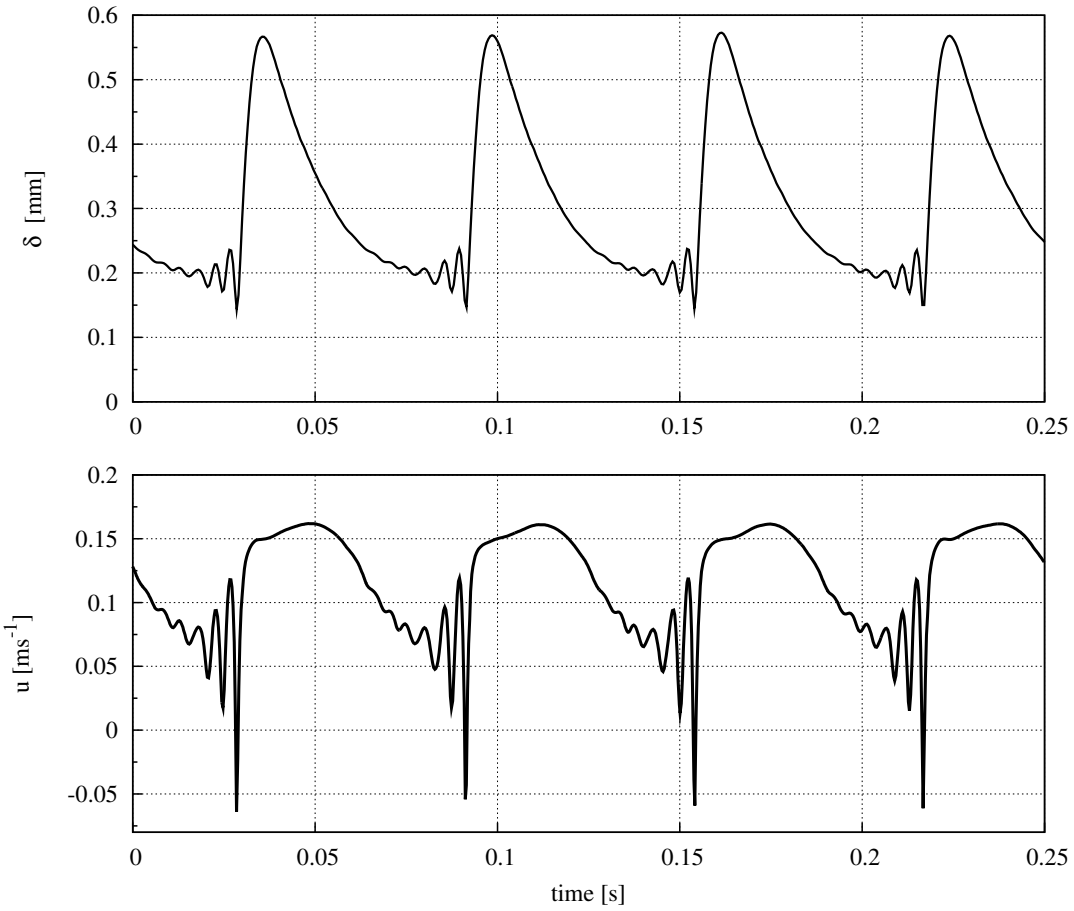

Figure 4.3: Time traces of film thickness and streamwise velocity from falling film simulation of DMSO solution (specified in Dietze *et al.* (2009)) with $Re = 15$, $f = 16\,\mathrm{Hz}$. The time traces were sampled at $y = 0.12\,\mathrm{mm}$ from the wall and $x = 120\,\mathrm{mm}$ from the inlet.

perturbations (see figures 4.4 and 4.5: $f = 30\,\mathrm{Hz}$). As perturbation frequency increases, short wavelength inlet disturbances evolve into sinusoidal surface waves with no preceding capillary waves (see figures 4.4 and 4.5: $f = 70\,\mathrm{Hz}$).

The disturbance introduced at the inlet grows as it travels downstream, consistent with linear stability analysis. The growth in amplitude deforms the free surface of the liquid film which in turn imposes a streamwise pressure gradient in the liquid film. This pressure gradient significantly impacts the dynamics and transport within the liquid film. The sign and magnitude of the streamwise pressure gradient is proportional to the streamwise derivative of the interface curvature Dietze *et al.* (2008).

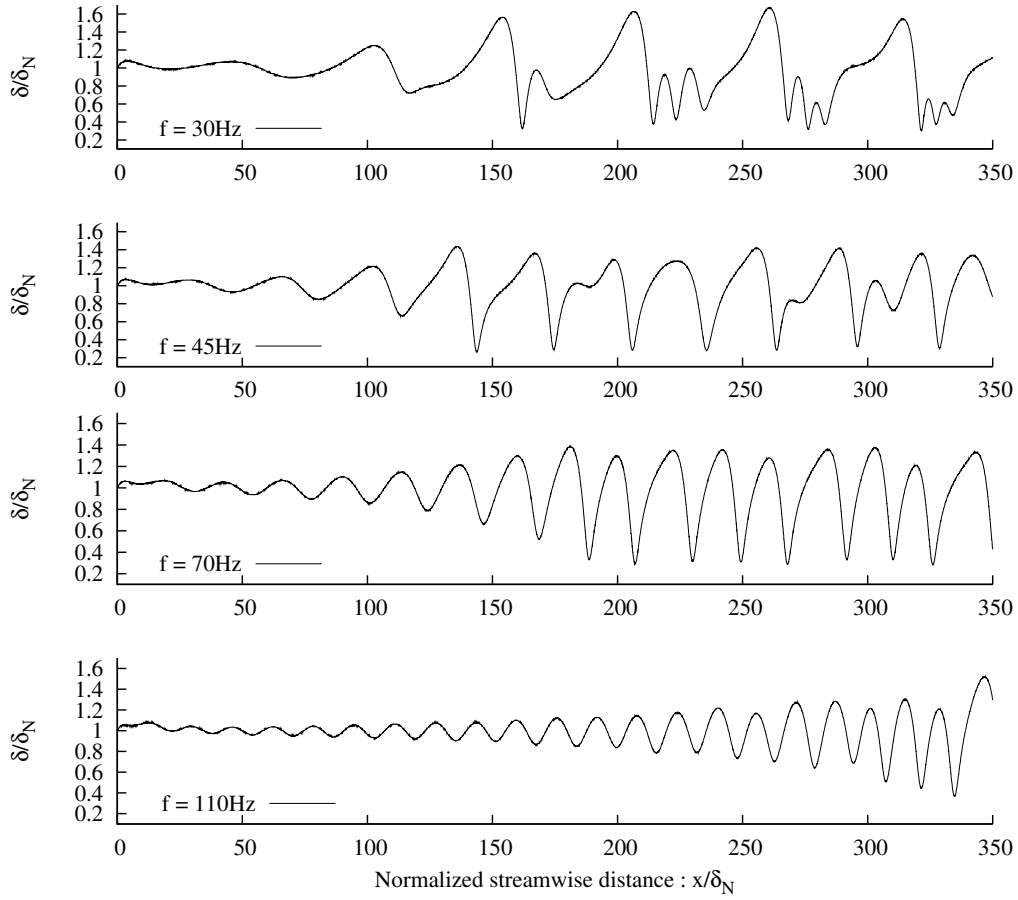

Figure 4.4: Surface wave profiles for simulated water falling film at $Re = 69$ and different inlet disturbance frequencies.

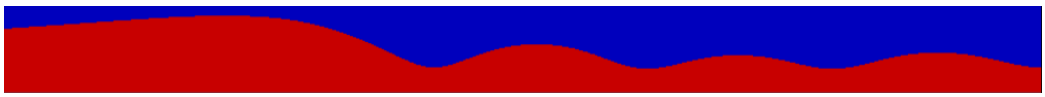

(a): $f = 30\,\mathrm{Hz}$

(b): $f = 70\,\mathrm{Hz}$

Figure 4.5: Film free surface wave profiles for (a): Solitary-capillary waves and (b): sinusoidal waves both at $Re = 69$. The red color represents the liquid film while blue is the gas phase and flow is from left to right.

This implies that the respective downward and upward concavity at the wave crest and preceding trough give rise to local negative and positive streamwise pressure

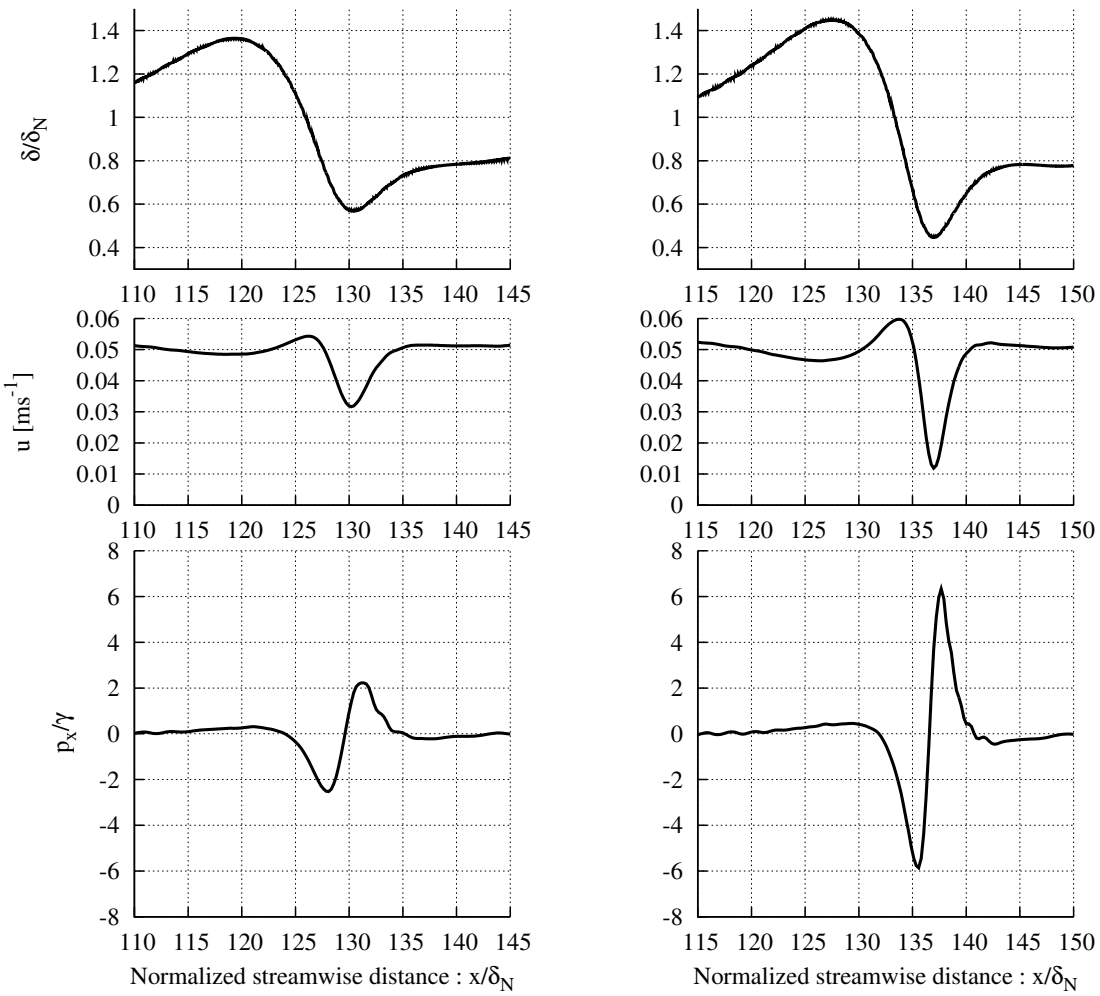

(a): $t = 2.410\,\mathrm{s}$ (b): $t = 2.415\,\mathrm{s}$

Figure 4.6: Normalized film thickness δ/δ_N, liquid film streamwise velocity u and normalized liquid film streamwise pressure gradient $p_x(=\frac{\partial p}{\partial x})/\gamma$ across a solitary wavefront with $Re = 69$ and $f = 30$Hz (note the change in abscissa scale). The streamwise velocity and pressure gradient distribution were sampled at a distance $20\,\mu$m from the wall.

gradients respectively across the wavefront.

Across the wavefront, fluid elements are either accelerated or decelerated depending on their position relative to the wavefront. Thus for the flow field between the wave crest and its preceding trough, we can identify regions where $\frac{\partial u}{\partial x}$ changes from positive to negative (see figure 4.6). As the wave grows to saturation, the steepness at the wavefront increases, with corresponding increase in the magnitude of the

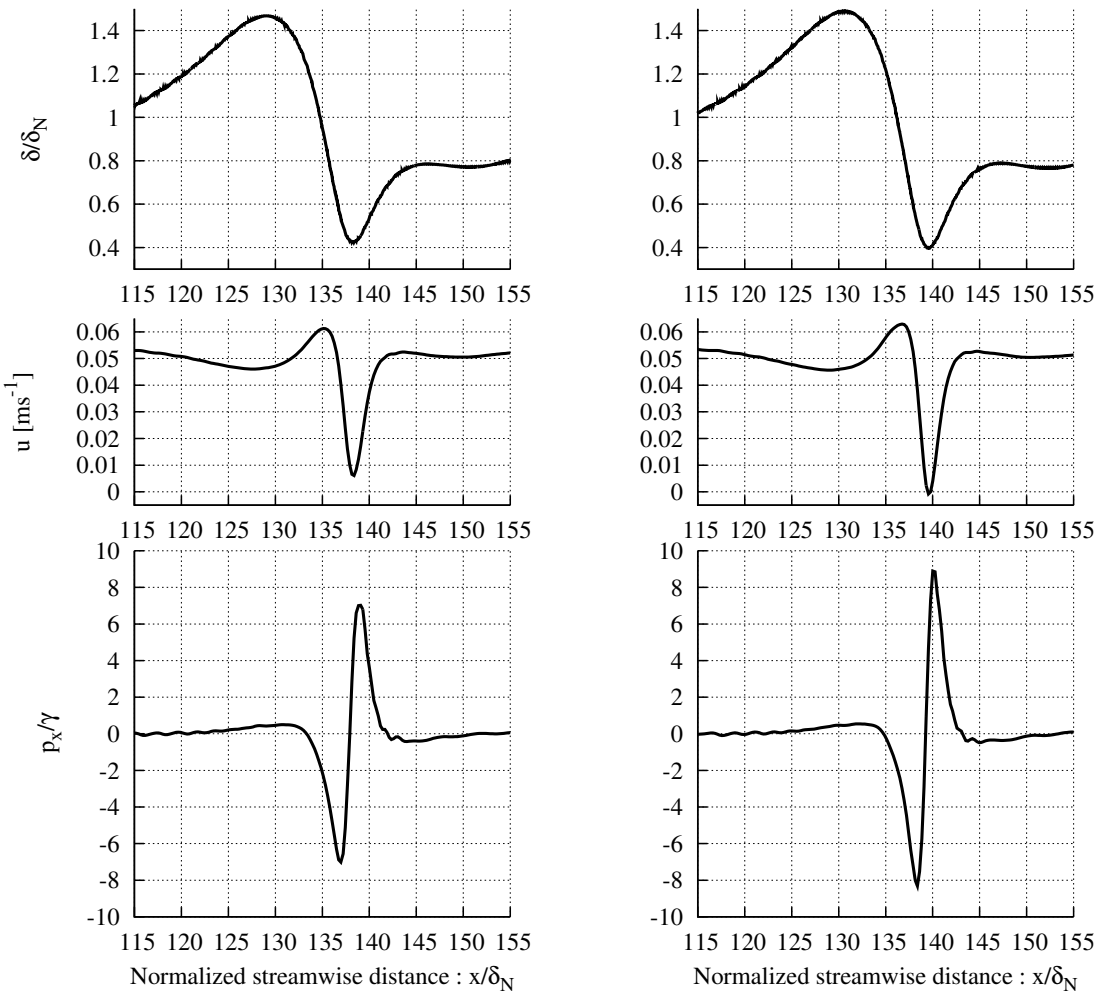

(a): $t = 2.416\,\mathrm{s}$ (b): $t = 2.417\,\mathrm{s}$

Figure 4.7: Normalized film thickness δ/δ_N, liquid film streamwise velocity u and normalized liquid film streamwise pressure gradient $p_x(=\frac{\partial p}{\partial x})/\gamma$ for the wave front in figure 4.6 after traveling further downstream. The streamwise velocity and pressure gradient distribution were sampled at a distance $20\,\mu$m from the wall.

wavefront streamwise pressure gradient. This results in larger streamwise variations of liquid streamwise velocity across the wavefront. Figure 4.6 shows the streamwise velocity and normalized streamwise pressure gradient for a traveling wave at different times ($\triangle t = 0.005\,\mathrm{s}$) for the $Re = 69$, $f = 30\,\mathrm{Hz}$ film flow. The streamwise velocity and pressure gradient distributions were sampled at a distance $y = 20\,\mu$m from the wall. The streamwise pressure gradient is normalized with the liquid specific weight $\gamma = \rho_l g$.

For liquid fluid elements close to the wall, the combined effect of shear and high local adverse streamwise pressure gradient could overwhelm the gravitational force driving the flow. At first, accelerated fluid elements (i.e. fluid elements from wave front region where $\frac{\partial u}{\partial x} > 0$) move "over" slower or decelerating fluid elements as depicted by streamlines moving away from the wall (see figure 4.8(a)). As the wave travels further downstream, the local positive (adverse) streamwise pressure gradient grows sufficiently large to force a change in sign (from positive to negative) of the local streamwise velocity of liquid fluid elements in the $\frac{\partial u}{\partial x} < 0$ region of the wavefront resulting in such fluid elements traveling upstream. However, the streamwise velocity of upstream traveling fluid elements remain negative only momentarily. As the wave front travels slightly further downstream, upstream traveling fluid elements end up in the wavefront region where $\frac{\partial p}{\partial x} < 0$ and $\frac{\partial u}{\partial x} > 0$. As a result, the streamwise velocity of upstream traveling fluid elements revert back to positive with flow now in the downstream direction. This cyclic process give rise to the backflow phenomenon observed in the capillary wave region of laminar falling liquid films (Kunugi & Kino, 2005; Dietze *et al.*, 2008, 2009).

Figures 4.7 - 4.8 show streamwise velocity, streamwise pressure gradient and streamlines for flow sequences leading to backflow with inlet perturbation frequency $f = 30$Hz. Although these results (i.e. figures 4.6 - 4.8) correspond to flow structures leading to backflow for a liquid film with solitary wave, the same holds true for a falling film free surface with only sinusoidal waves. Figure 4.9 shows a similar sequence for a growing sinusoidal wave-train where the increasing adverse pressure gradient at the wavefront of the leading sinusoidal wave (fully shown) eventually induces backflow at its wavefront.

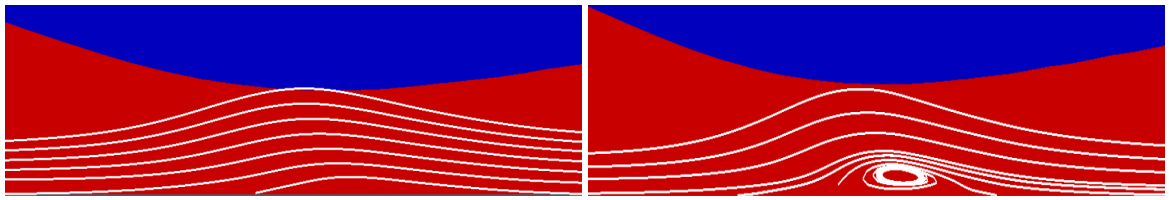

(a): $t = 2.416\,\mathrm{s}$ (b): $t = 2.417\,\mathrm{s}$

Figure 4.8: (a) and (b) are streamlines at the solitary wavefront corresponding to flow conditions in figure 4.7 (a) and (b) respectively.

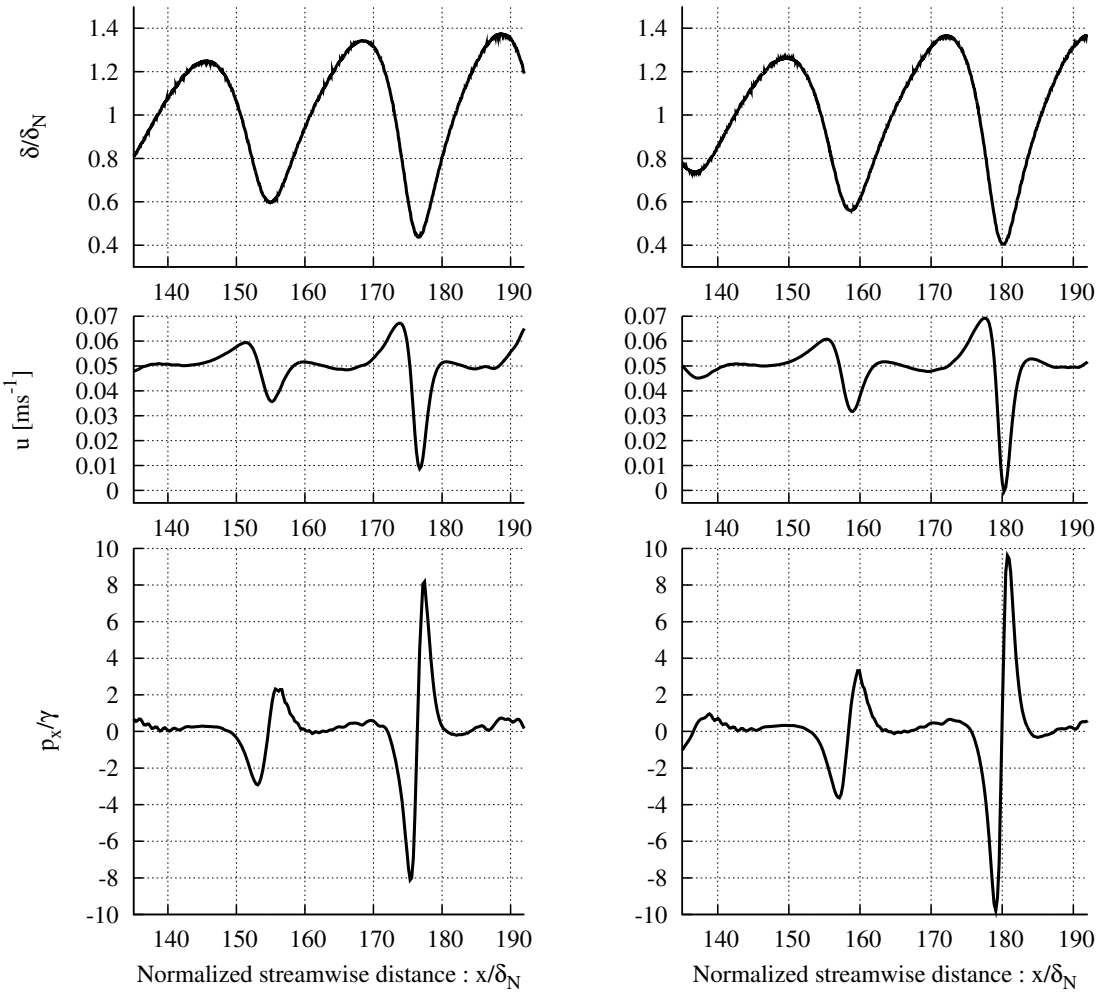

(a): $t = 2.4055\,\mathrm{s}$ (b): $t = 2.4075\,\mathrm{s}$

Figure 4.9: Normalized film thickness $\delta/\delta_{_N}$, liquid film streamwise velocity u and normalized liquid film streamwise pressure gradient $p_x(=\frac{\partial p}{\partial x})/\gamma$ across the wavefront with $Re = 69$ and $f = 70\,\mathrm{Hz}$. The streamwise velocity and pressure gradient distribution were sampled at a distance $20\,\mu$m from the wall.

4.4.2 Dynamics of Backflow

The crosswise variation of the streamwise pressure gradient is negligible within the liquid film (see figure 4.10). As a result, liquid fluid elements in the layer just above the wall experience backflow earlier than those further away. Although flow separation at the wall occurs at the point where the crosswise derivative of the streamwise velocity first vanishes for that wave, backflow is initiated only when this derivative is negative. Figure 4.11 shows plots of the normalized maximum positive (or adverse) streamwise pressure gradient $(p_x)^+/\gamma$ and normalized wall shear stress $\tau_w (= \mu_l \frac{\partial u}{\partial y}|_{y=0})/\gamma\delta_N$ both measured at the wavefront of traveling solitary ($f = 30\,\text{Hz}$) and sinusoidal ($f = 70\,\text{Hz}$) waves. All values are measured at the wall (i.e. $y = 0$) as the wave continues downstream. These plots provide qualitative insights with respect to the influence of downstream wave evolution on the dynamics of falling film backflow. For either solitary or sinusoidal waves, the adverse streamwise pressure gradient $(p_x)^+/\gamma$ for a growing disturbance (wave) attains a first maximum (see bottom plots of figure 4.11) which corresponds to saturation point for that disturbance/wave. Subsequent to attaining the peak value, $(p_x)^+/\gamma$ for the sinusoidal wave evolves with small deviations from the maximum as the wave continues downstream. For the traveling solitary wave, $(p_x)^+/\gamma$ undergoes relatively large excursions from and then back to near-peak values.

4.4.2.1 Open Vortex

From figure 4.11, backflow (i.e. $\frac{\partial u}{\partial y}|_{y=0} < 0$) precedes wave saturation (i.e. $(p_x)^+/\gamma$ attaining first maximum). This means the traveling wave continues to grow in amplitude or steepness (resulting in a thinner liquid film directly in front of the wave) subsequent to the onset of backflow. In addition, the increasingly higher adverse streamwise pressure gradients developed at the wavefront, forces more liquid fluid

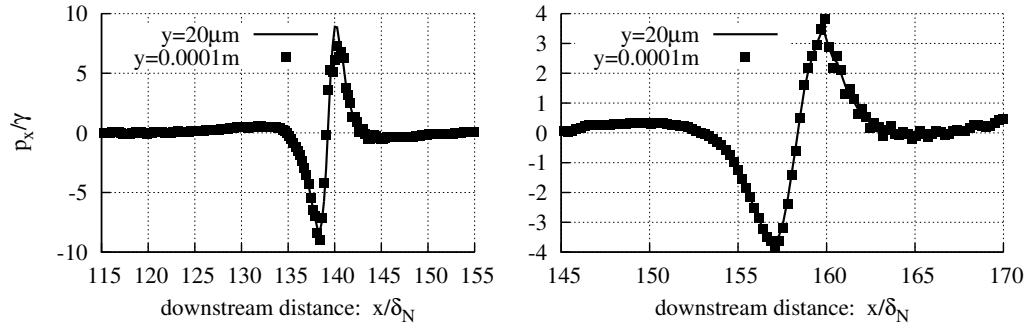

(a) : $f = 30\,\mathrm{Hz}$ (b) : $f = 70\,\mathrm{Hz}$

Figure 4.10: Normalized liquid film streamwise pressure gradient $p_x(=\frac{\partial p}{\partial x})/\gamma$ across the wavefront for $Re = 69$, $f = 30\,\mathrm{Hz}$ and $70\,\mathrm{Hz}$ sampled at $20\,\mu$m and $0.0001\,$m from the wall.

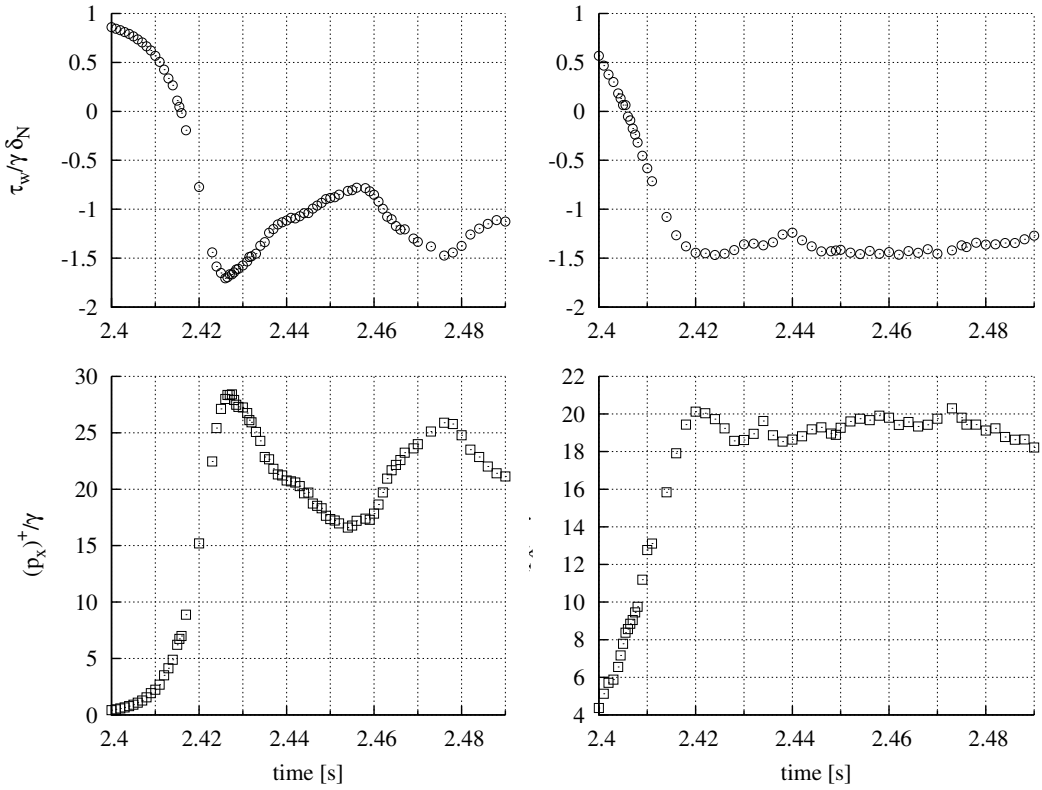

(a) : $f = 30\,\mathrm{Hz}$ (b) : $f = 70\,\mathrm{Hz}$

Figure 4.11: Normalized maximum positive streamwise pressure gradient $(p_x)^+/\gamma$, and normalized wall shear stress $\tau_w(=\mu_l\frac{\partial u}{\partial y}|_{y=0})/\gamma\delta_N$ measured at the wavefront of a solitary wave (a) and sinusoidal wave (b), both traveling downstream.

elements further from both the wall and the wavefront to flow in the upstream direction. As a result, the closed circulation region grows both in the streamwise and

crosswise directions. Further decrease in height of the liquid film in front of the wave eventually transforms the growing closed circulation into an open vortex or "*U - loop*" (Dietze *et al.*, 2009). This process applies to both solitary and sinusoidal waves (see figures 4.12 and 4.13). For the closed circulation backflow, a closed loop for the circulating liquid fluid elements can be defined entirely within the liquid film. This differentiates it structurally from the open vortex. In general, for a fixed Reynolds number, the sinusoidal wave attains saturation further downstream than the solitary wave and the height of its preceding trough at saturation is greater than that of the solitary wave (see figure 4.14). In particular, the higher adverse streamwise pressure gradient and smaller preceding film height at saturation induces a more intense open vortex circulation zone at the solitary wavefront. Figure 4.14 shows crosswise velocity distributions across the wavefronts of solitary and sinusoidal waves at saturation. The plots show that at similar points from the wall, liquid fluid elements at the solitary wavefront circulation zone have higher crosswise velocities indicating higher rates of crosswise transport.

4.4.2.2 Solitary-Capillary Waves

For both sinusoidal and solitary waves, the flow structure and dynamics leading to backflow are the same. In addition, the evolution of a closed backflow region into an open vortex follows the same process for both wave types. However, once the wavefront adverse streamwise pressure gradient $(p_x)^+/\gamma$ grows to its saturation value, the dynamics of the backflow region evolve differently for the two wave types. For the sinusoidal wave, $(p_x)^+/\gamma$ remains approximately equal to the first maximum value as the wave travels downstream. Consequently, the backflow region preceding the saturated wave retains its open vortex structure. This is valid so long as the sinusoidal structure or shape of the traveling wave is not fundamentally altered by secondary instabilities.

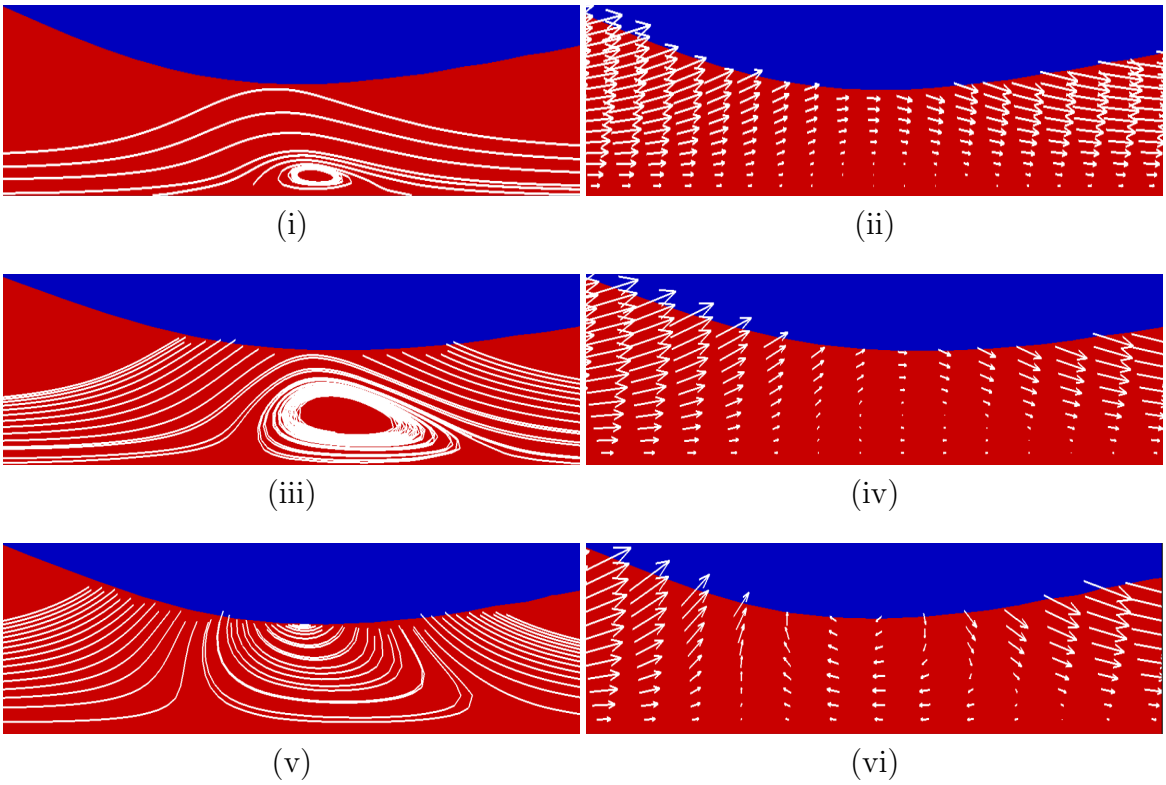

Figure 4.12: Streamlines and velocity vector plots showing evolution from flow separation to closed circulation and then open vortex for the backflow region at the wavefront of the solitary ($f = 30\,\mathrm{Hz}$) wave: $t = 2.417\,\mathrm{s}$ (i) and (ii); $t = 2.419\,\mathrm{s}$ (iii) and (iv); $t = 2.422\,\mathrm{s}$ (v) and (vi).

Beyond the saturation point, $(p_x)^+/\gamma$ for the solitary wave evolves like a time-periodic function (going through multiple distinct minima/maxima) as the wave travels downstream. This phenomenon is a consequence of the interaction between the solitary wave and its preceding capillary wave. The nature of the interaction is such that a decrease in $(p_x)^+/\gamma$ or $(p_x)^-/\gamma$ across the solitary wavefront is followed by an increase in $(p_x)^+/\gamma$ or $(p_x)^-/\gamma$ at the wavefront of the preceding capillary wave. For convenience, we use $(p_x)^+/\gamma$ only in the following analysis. Since $(p_x)^+/\gamma$ is a measure of interface deformation at the wavefront, this interaction suggests a conservation of surface (deformation) energy between the solitary and capillary waves. For the capillary wave, the increase in $(p_x)^+/\gamma$ corresponds to an increase in capillary wavefront steepness (see figure 4.15). For the solitary wave, the decrease in $(p_x)^+/\gamma$

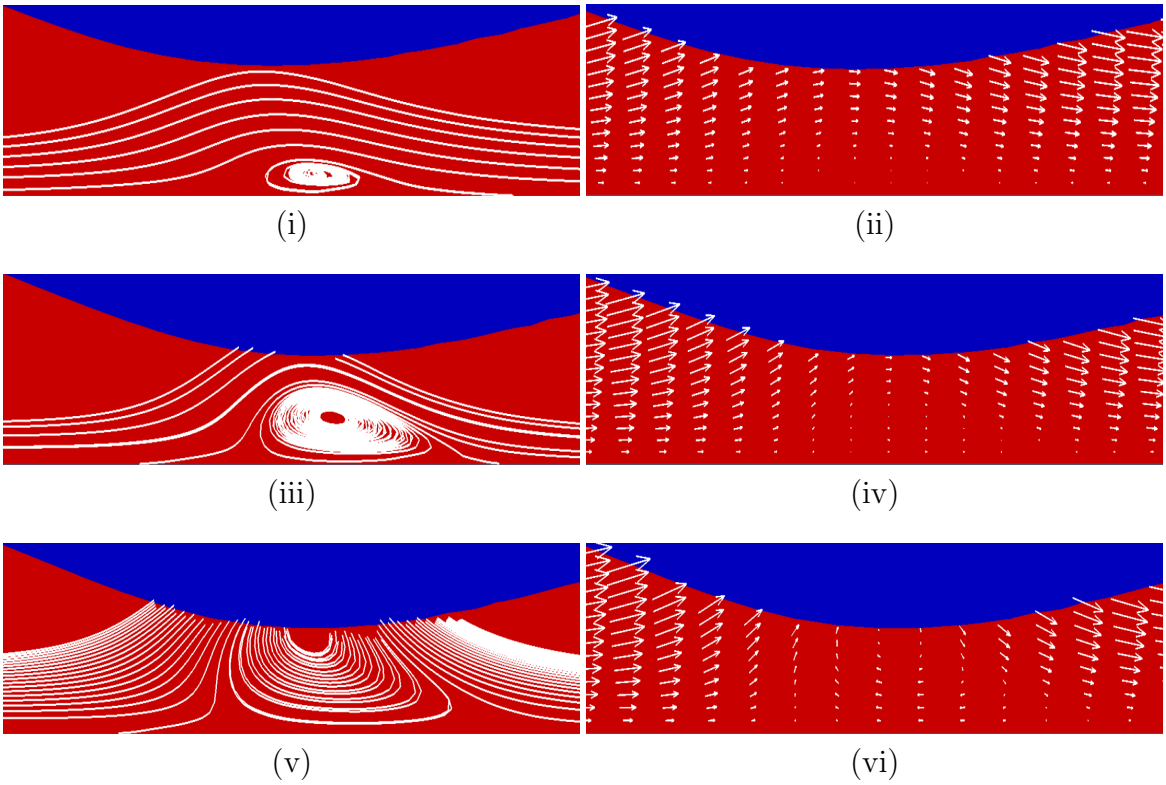

Figure 4.13: Streamlines and velocity vector plots showing evolution from flow separation to closed circulation and then open vortex for the backflow region at the wavefront of the sinusoidal ($f = 70\,\mathrm{Hz}$) wave: $t = 2.408\,\mathrm{s}$ (i) and (ii); $t = 2.412\,\mathrm{s}$ (iii) and (iv); $t = 2.418\,\mathrm{s}$ (v) and (vi).

results in an increase in height of its preceding trough. However, the structure of the solitary wave is not fundamentally altered (also see figure 4.15).

The combined effect of increased film steepness and large adverse streamwise pressure gradients results in backflow at the capillary wavefront. The corresponding closed circulation region evolves quickly into an open vortex (see right end of figure 4.16). For the solitary wave however, the reduced adverse streamwise pressure gradient and increased height of its preceding wave trough transforms the initial open vortex at the wavefront of the solitary wave into a closed recirculation region (see left end of figure 4.16).

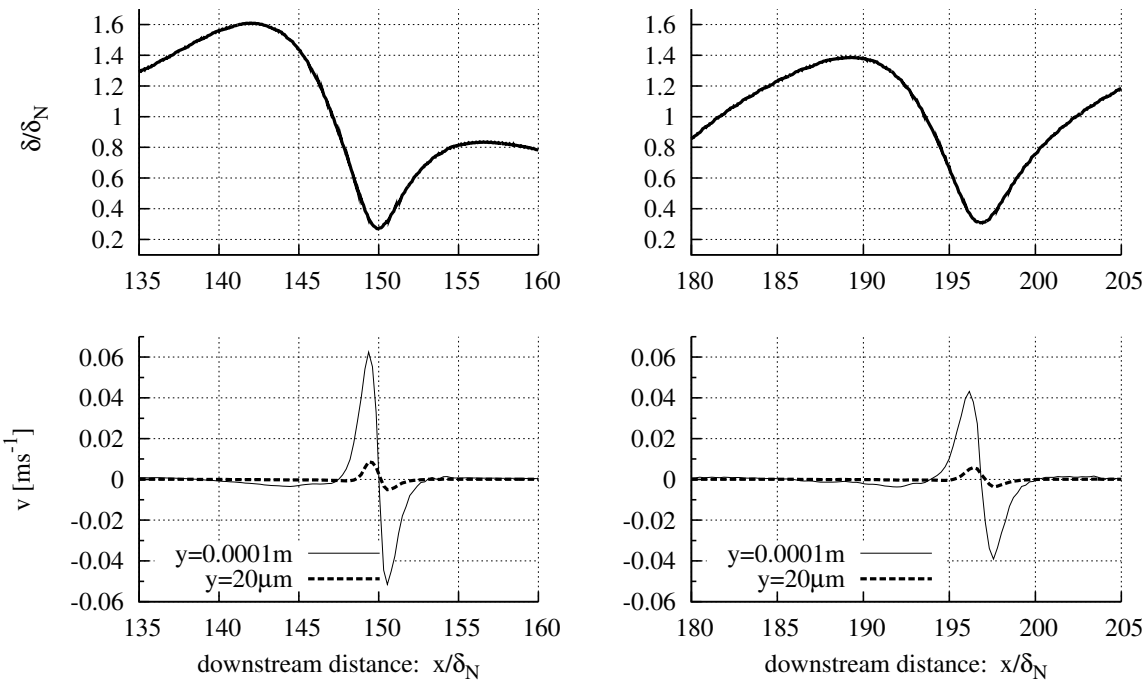

(a) : $f = 30\,\mathrm{Hz}$; $t = 2.425\,\mathrm{s}$ (a) : $f = 70\,\mathrm{Hz}$; $t = 2.420\,\mathrm{s}$

Figure 4.14: Normalized interface height δ/δ_N and crosswise velocity v at saturation for solitary (a) and sinusoidal (b) waves at $Re = 69$.

4.4.2.3 Solitary-Capillary-Capillary Waves

As the wavefront of the capillary wave steepens, the height of its preceding trough reduces resulting in more liquid fluid elements being displaced away from the capillary wavefront. To conserve the volume of liquid displaced, a second capillary wave gradually forms in front of the first capillary wave while the height of the trough preceding the solitary wave increases (see lower plots of figure 4.15). The first capillary wave appears to inherit the properties of the saturated solitary wave. Similar to the solitary wave, $(p_x)^+/\gamma$ for the first capillary wave grows to a maximum and thereafter starts to decrease. In this instance, the decrease in $(p_x)^+/\gamma$ at the wavefront of the first capillary wave is followed by an increase in $(p_x)^+/\gamma$ at the wavefronts of both the solitary wave and the newly formed second capillary wave (see figure 4.17).

The increase in $(p_x)^+/\gamma$ at the wavefront of the second capillary wave results in

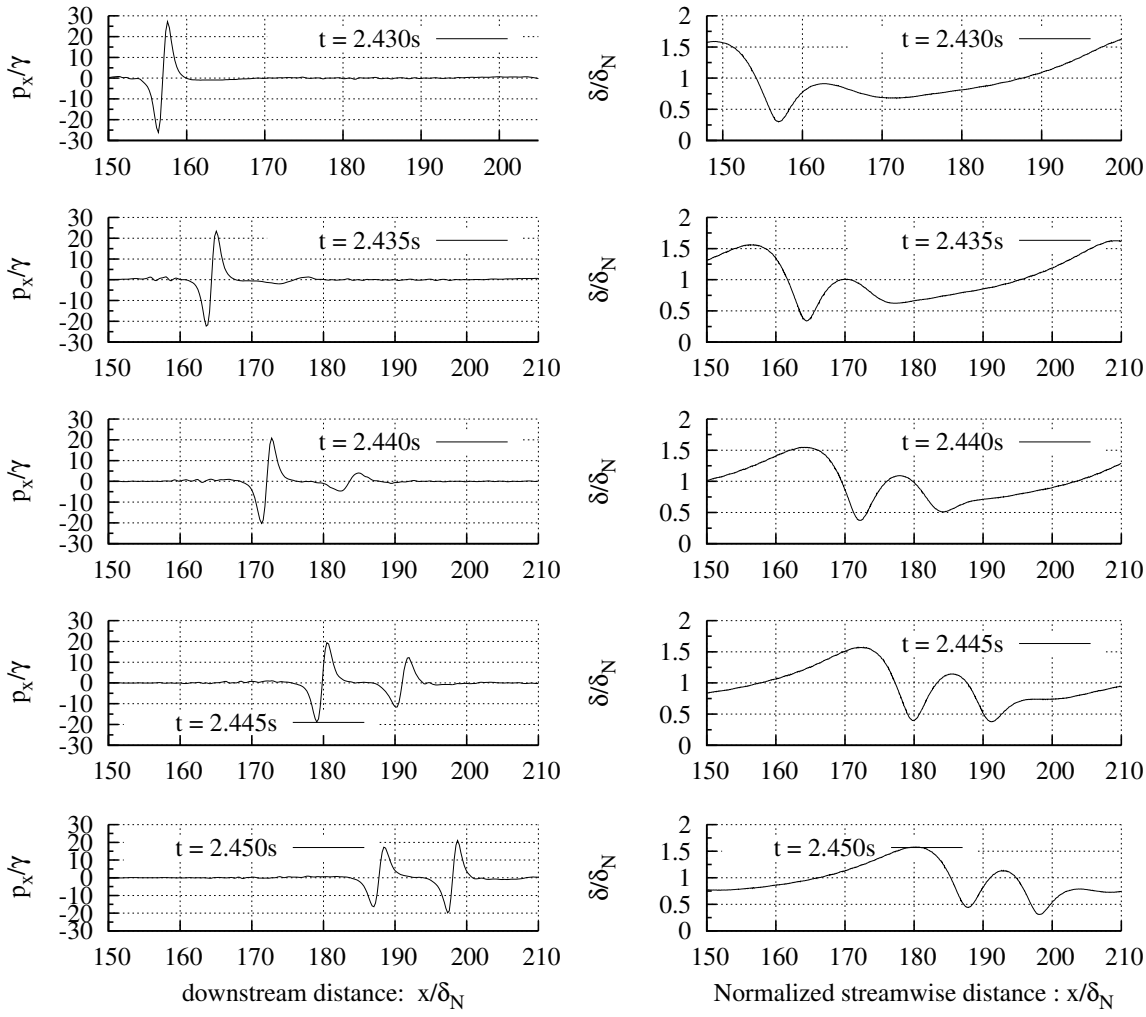

Figure 4.15: Normalized liquid film streamwise pressure gradient ($p_x = \frac{\partial p}{\partial x})/\gamma$ and normalized interface height $\delta/\delta_{_N}$ for flow conditions corresponding to solitary-capillary waves interaction.

a backflow region at its wavefront. Unlike the first capillary wave, this closed circulation backflow region does not evolve into an open vortex. This follows from the fact that energy exchange in this instance is between three waves and that the total energy exchanged (i.e. between solitary-capillary and solitary-capillary-capillary interactions) is conserved. As a result, the second capillary wavefront is not deformed (or steepened) sufficiently to transform its closed circulation region into an open vortex. The conservation of exchanged energy also explains why $(p_x)^+/\gamma$ for the solitary

(a) : $t = 2.440\,\mathrm{s}$

(b) : $t = 2.445\,\mathrm{s}$

(c) : $t = 2.450\,\mathrm{s}$

Figure 4.16: Streamlines between the wavefronts of the solitary wave and the preceding first capillary wave for the flow conditions in figure 4.15. (a): open vortex at wavefront of solitary wave, (b): closed circulation at wavefront of solitary and capillary waves, (c): open vortex at wavefront of capillary wave and closed circulation at wavefront of solitary wave.

wave does not grow back to its initial maximum value (see figures 4.11 and 4.17)). However $(p_x)^+/\gamma$ still grows large enough to transform the closed circulation region at the solitary wavefront back into an open vortex. For the first capillary wave, the decrease in $(p_x)^+/\gamma$ and increased height of its preceding trough means the open vortex at its wavefront reverts back to a closed circulation backflow (see figure 4.18).

The cycle of energy exchange and formation of multiple backflow regions continue as the solitary-capillary wave-train interactions continue travels downstream. In general the number of preceding capillary waves that develop in front of the large amplitude solitary wave decrease with increasing frequency of inlet disturbance. Low frequency disturbances give rise to large amplitude solitary waves which in turn attain much larger $(p_x)^+/\gamma$ at saturation. Such waves are also separated by longer and thinner liquid films in between. Consequently their wave interactions are characterized by large energy exchanges which allow multiple smaller capillary waves and backflow

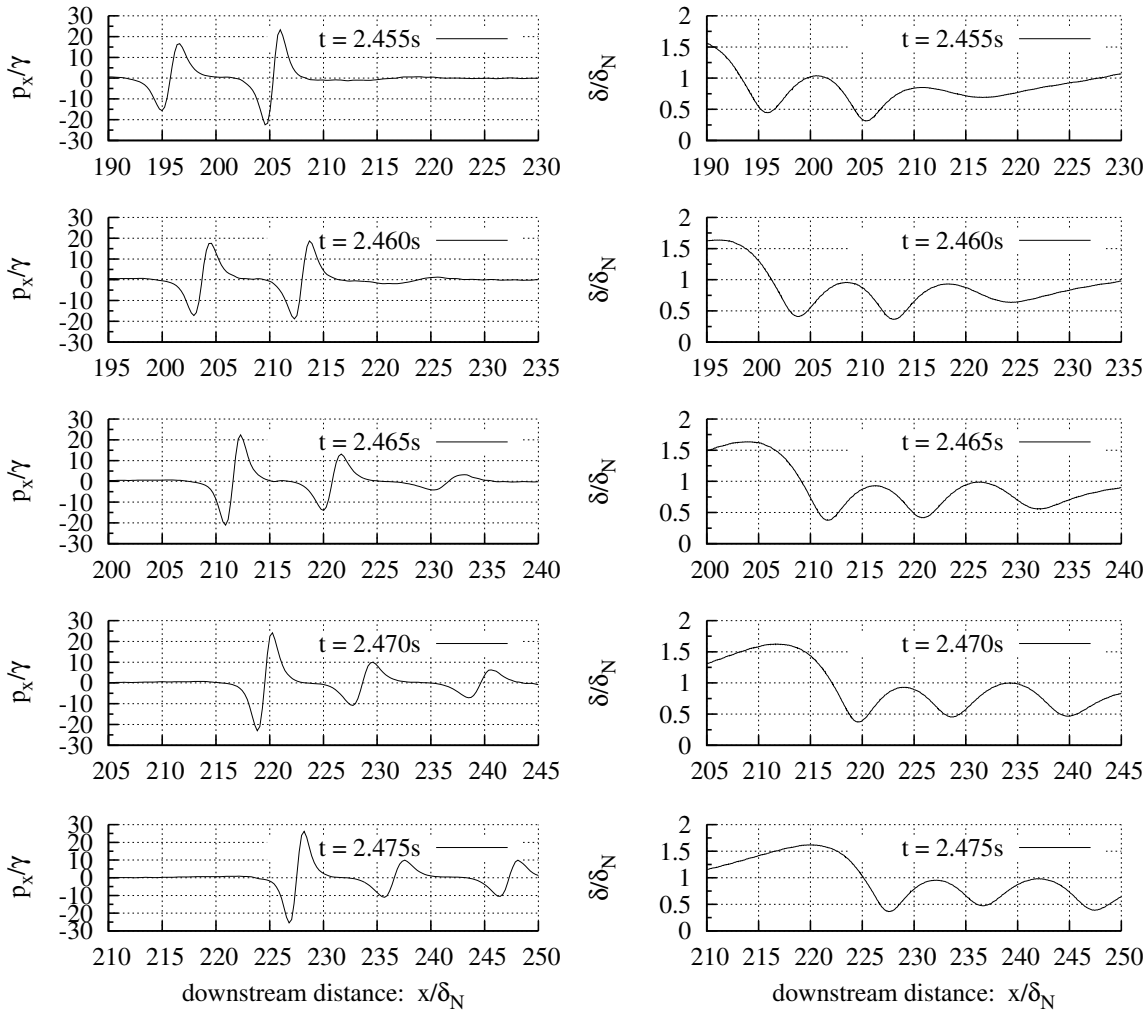

(a) : $f = 30\,\mathrm{Hz}$ (b) : $f = 70\,\mathrm{Hz}$

Figure 4.17: Normalized liquid film streamwise pressure gradient ($p_x = \frac{\partial p}{\partial x})/\gamma$ and normalized interface height δ/δ_N for flow conditions corresponding to solitary-capillary-capillary waves interaction.

Figure 4.18: Streamlines at the wavefronts of the solitary wave and the preceding first and second capillary waves at $t = 2.480$s showing a newly formed backflow region at the second capillary wavefront (right-end) and a diminished closed circulation at the first capillary wavefront (middle). The backflow region at the front of the solitary wave has reverted to an open vortex.

regions to evolve.

4.4.3 Buoyancy and Viscous Dissipation

To investigate the influence of buoyancy and viscous dissipation on low Reynolds number falling film flow separation, numerical simulations were run for water at Reynolds number $Re = 20.1$, $f = 27\,\mathrm{Hz}$, inlet temperature $T_{in} = 298\,\mathrm{K}$ and uniform wall temperature fixed at $T_w = 303\mathrm{K}$. The conservation law for energy transport with viscous dissipation is expressed as:

$$\frac{\partial \rho c_p T}{\partial t} + \boldsymbol{\nabla} \cdot (\rho \boldsymbol{v} c_p T) \;=\; \boldsymbol{\nabla} \cdot (k \boldsymbol{\nabla} T) + \boldsymbol{\tau} : \boldsymbol{\nabla} \boldsymbol{v} \tag{4.2}$$

where $\boldsymbol{\tau} : \boldsymbol{\nabla} \boldsymbol{v}$ represents the contribution to internal energy due to viscous dissipation. Liquid density as a function of temperature variation is given by:

$$\frac{\rho_{_l}}{\rho_{\mathrm{ref}}} = 1 - \Phi(T - T_{\mathrm{ref}}) \tag{4.3}$$

where $\Phi = 0.257\,\mathrm{x}\,10^{-3}\,\mathrm{K}^{-1}$ is coefficient of volume expansion of water, T_{ref} is same as inlet temperature and ρ_{ref} is liquid density at T_{ref}. Analysis of results from the numerical solution of equation (4.2) with the Navier-Stokes equations indicate that buoyancy and viscous dissipation have minimal influence on the formation and propagation of backflow for low Reynolds number falling films. In particular, the onset and subsequent size of the backflow region remained unchanged with addition of heat transfer effects. We also observed no significant change in surface wave properties such as wave separation, phase speed and maximum wave amplitude for the case simulated.

CHAPTER 5

WAVY-LAMINAR FALLING LIQUID FILM FREE SURFACE EVAPORATION

5.1 Background

Interfacial waves on falling liquid films enhance energy transfer between the liquid film and the heating or cooling surface (Kutateladze & Gogonin, 1979; Jayanti & Hewitt, 1995; Miyara, 1999). Extensive experimental studies (see for example Chun & Seban, 1971; Schnabel & Schlunder, 1980; Holmberg *et al.*, 1991; Abdulmalik *et al.*, 1998) have been conducted for falling liquid film evaporation to correlate the average heat transfer coefficient in terms of film Reynolds number Re and liquid Kapitza number Ka. These experimental studies are valid over a wide range of liquid Prandtl numbers and apply to falling liquid films in the laminar, wavy-laminar and turbulent flow regimes. Although suitable for predicting overall evaporation heat transfer, such correlations provide little insight into detailed flow physics of falling liquid films as characterized by free surface deformation and how such deformations in turn influence local heat transport and rate of evaporation.

At very high Reynolds numbers, falling film interfacial dynamics is dominated by internal turbulence (Chang, 1994) implying that transport in the liquid film is predominantly due to turbulent mixing. For low - moderate Reynolds numbers (e.g. $Re < 500$), the liquid film consists of long interfacial waves dominated by gravity-capillary effects. In this so-called wavy-laminar regime, transport in the film is significantly influenced by the nature and evolution of interfacial waves. Depending on film Reynolds number Re, Kapitza number Ka and the wavelength of flow perturbation, the interfacial waves evolve into finite amplitude sinusoidal or solitary waves with the

later eventually preceded by capillary waves (Chang, 1994; Nosoko & Miyara, 2004). The present study focuses on falling film evaporation in the wavy-laminar flow regime with perturbation frequency resulting in solitary-capillary interfacial waves.

Results from the numerical simulations of transport phenomena in low Reynolds number falling liquid films (Jayanti & Hewitt, 1995; Miyara, 2000; Gao *et al.*, 2003; Kunugi & Kino, 2005; Dietze *et al.*, 2008, 2009) indicate that transport enhancement can be attributed to reduction in film thickness and the formation of circulation zones (see discussion in § 4.1) at specific free surface wave regions within the liquid film. With respect to transport enhancement, Jayanti & Hewitt (1995) argued that the overall heat transfer is still dominated by conduction primarily due to reduction in effective film thickness. They concluded that the contribution of circulation to heat transfer enhancement is minimal. Miyara (2000) contended that heat transfer enhancement was due to a combination of both film thinning and convection effects resulting from circulation flow in solitary or roll waves. Kunugi & Kino (2005) and Dietze *et al.* (2008) reported that heat transport is enhanced in the liquid film by crosswise velocities in the backflow regions. As at the time of this report, numerical studies for evaporation of moderately high Reynolds number falling liquid films have not been reported in the literature. As a result, it is not conclusive if the regimes of transport that dominate low Reynolds number films remain valid at moderately high Reynolds number wavy-laminar falling film flows.

This chapter investigates the influence of interfacial wave dynamics on evaporation heat transfer for moderately high Reynolds number 2-D wavy-laminar falling liquid films based on numerical solution of the Navier-Stokes equation on highly resolved computational grids. For the waveforms that develop at different regions of the falling liquid film, we analyze the dominant wave induced mechanism of crosswise transport and the possible enhancement of evaporation heat transfer. We study the correlation between free surface waveforms, film thickness and streamwise variation

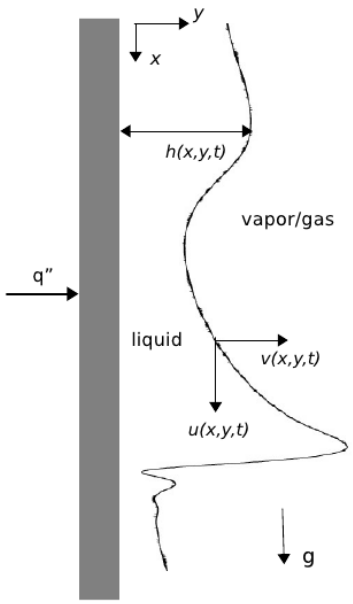

Figure 5.1: Schematic diagram of a wavy falling liquid film with constant flux heating: u, v are x, y velocity components, h is wave height, q'' is wall heat flux, $\mathbf{g}$ is gravitational acceleration.

of wall temperature for the case of constant wall heat flux. In the fully developed thermal region, we investigate the interfacial rate of evaporation at different regions of a fully developed 2-D free surface wave.

5.2 Mathematical Model

We consider the flow of a constant property Newtonian liquid film down a constant heat flux vertical wall under conditions where the flow regime is wavy-laminar with the film interface dominated by solitary-capillary waves (see figure 5.1). The liquid enters the evaporator at saturation conditions and flows under the influence of gravity with a sharp interface separating it from saturated vapor.

5.2.1 Governing Equations

The respective continuity, momentum, energy and phase equations for the two-phase flow field are expressed as:

$$\frac{\partial \rho}{\partial t} + \boldsymbol{\nabla} \cdot (\rho \boldsymbol{v}) = 0 \tag{5.1a}$$

$$\frac{\partial \rho \boldsymbol{v}}{\partial t} + \boldsymbol{\nabla} \cdot (\rho \boldsymbol{v}\boldsymbol{v}) = -\boldsymbol{\nabla} p + \boldsymbol{\nabla} \cdot \boldsymbol{\tau} + \rho \mathbf{g} + \int_{A_\mathrm{I}(t)} \sigma \kappa' \boldsymbol{n}' \delta_\mathrm{I}(\boldsymbol{x} - \boldsymbol{x}') \, \mathrm{d}A_\mathrm{I} \tag{5.1b}$$

$$\frac{\partial \rho c_p T}{\partial t} + \boldsymbol{\nabla} \cdot (\rho \boldsymbol{v} c_p T) = \boldsymbol{\nabla} \cdot (k \boldsymbol{\nabla} T) - \dot{S}_{q,e} \tag{5.1c}$$

$$\frac{\partial \alpha}{\partial t} + \boldsymbol{\nabla} \cdot (\boldsymbol{v} \alpha) = -\dot{S}_v \tag{5.1d}$$

where $\boldsymbol{v}$ is velocity, $\boldsymbol{\tau}$ is the deviatoric stress tensor, p is pressure, T is temperature and α is phase volume fraction. $\dot{S}_{q,e}$ and $\dot{S}_v$ are the respective evaporation induced source terms for latent heat sink and liquid vaporization. The source term in (5.1d) tracks the position of the interface by accounting for liquid vaporization only.

5.2.2 Evaporation Source Terms

Liquid vaporization at the film free surface results in an interfacial energy sink which is given by the product of the mass rate of vaporization and the enthalpy of vaporization (at the corresponding saturation conditions). We assume that the interface remains at saturation temperature T_{sat}. Thus, for positive deviations of the interfacial temperature T_i from T_{sat} the heat flux on the excess temperature of the phase boundary is given by the simplified model (Tanasawa, 1991):

$$j_e^h = \eta_e (T_i - T_\mathrm{sat}) \tag{5.2}$$

where j_e^h is the evaporation heat flux density. The interfacial vaporization heat transfer coefficient η_e is evaluated as (Schrage, 1953):

$$\eta_e = \frac{2\psi_e}{2 - \psi_e} \frac{h_e^2}{\sqrt{2\pi R_{gas}}} \frac{\rho_g}{T_\mathrm{sat}^{3/2}} \tag{5.3}$$

where ψ_e is evaporation coefficient (typically $0 < \psi_e \leq 1$), h_e is enthalpy of vaporization and R_{gas} is the gas constant of water. The volume V integral of the magnitude of

the gradient of the phase fraction field α over a region enclosing the interface measures the interfacial area (Hardt & Wondra, 2008). Combining this integral with equation (5.2), the evaporation source terms are defined as:

$$\dot{S}_{q,e} = \frac{j_e^h}{V} \int_V |\boldsymbol{\nabla}\alpha| \, \mathrm{d}V \tag{5.4a}$$

$$\dot{S}_v = \frac{\dot{S}_{q,e}}{\rho_l h_e} \tag{5.4b}$$

Since the gradient of the volume fraction field vanishes everywhere except in the interfacial region, the source terms are non-zero only at the film interface.

5.2.3 Boundary and Initial Conditions

The boundary conditions for velocity and phase volume fraction are the same for the case of a non-heated falling liquid film as described in § 2.1.5. Only boundary and initial conditions for temperature are presented in this section. At the liquid and vapor sections of the evaporator inlet, temperature is fixed at the saturation value. Along the wall on which the liquid film flows, a constant heat flux is maintained. At the outlet of the evaporator, outflow conditions are specified i.e. $\frac{\partial T}{\partial x} = 0$ while a zero-flux condition is maintained on the numerical wall boundary. The flow domain is initialized with saturated liquid and vapor.

5.3 Numerical Validation

Validation results for numerical simulation of falling film velocity field and wave properties (e.g. phase speed, maximum wave height) based on comparisons with experimental correlations for 2-D falling films are presented and discussed in § 4.3. In this section, we present validation results for phase change and evaporation heat transfer by comparing numerical simulation results for the governing equations and source terms with analytical solutions for Stefan problem and experimental correlations developed for evaporation heat transfer coefficient for wavy-laminar falling liquid films.

5.3.1 Stefan Problem

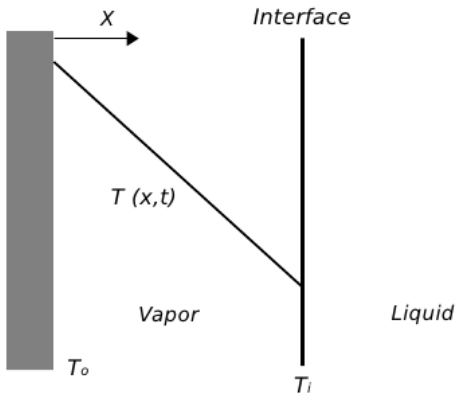

Figure 5.2: Specification of Stefan problem

We consider the case where heat is transferred by conduction from a heated wall through vapor to a liquid/vapor interface (see figure 5.2). The liquid and the phase boundary (interface) remain at saturation temperature T_{sat} while the wall is kept isothermal at a temperature $T_o > T_{sat}$ so that liquid vaporization leads to a motion of the interface away from the heating wall. With the assumption of a flat interface, the formulation reduces to a 1-D problem. The analytical solution for this problem was obtained by Neumann (see Welch & John, 2000; Hardt & Wondra, 2008) where the interfacial position $x_i(t)$ and temperature distribution $T(x,t)$ are respectively expressed as:

$$x_i(t) \;=\; 2\zeta\sqrt{\lambda_g t} \tag{5.5a}$$

$$T(x,t) \;=\; T_o + \frac{T_{sat}-T_o}{\operatorname{erf}(\zeta)}\operatorname{erf}\left(\frac{x}{2\sqrt{\lambda_g t}}\right) \tag{5.5b}$$

erf is the error function, $\lambda_g = \kappa_g/\rho_g c_{p_g}$ is the thermal diffusivity for the vapor phase and the parameter ζ is determined from the transcendental equation:

$$\zeta \exp(\zeta^2)\operatorname{erf}(\zeta) = \frac{c_{p_g}(T_o - T_{sat})}{h_e\sqrt{\pi}} \tag{5.6}$$

Liquid and vapor properties used in the Stefan problem numerical simulation were set based on the validation studies of Hardt & Wondra (2008): $\rho_l = 1.0\,\mathrm{kgm^{-3}}$, $\rho_g = 1.0\,\mathrm{kgm^{-3}}$, $\nu_l = 1.0\,e-05\,\mathrm{m^2s^{-1}}$, $\nu_g = 1.0\,e-05\,\mathrm{m^2s^{-1}}$, $c_{p_l} = 1000\,\mathrm{Jkg^{-1}K^{-1}}$, $c_{p_g} = 1000\,\mathrm{Jkg^{-1}K^{-1}}$, $\kappa_l = 1.0\,\mathrm{Wm^{-1}K^{-1}}$, $\kappa_g = 1.0\,e-02\,\mathrm{Wm^{-1}K^{-1}}$, $h_e = 1.0\,e\,06\,\mathrm{Jkg^{-1}}$, $T_{sat} = 373.15\,\mathrm{K}$, $T_o = 383.15\,\mathrm{K}$, $\sigma = 0.01\,\mathrm{Nm^{-1}}$ and $g = 9.78\,\mathrm{ms^{-2}}$. The choice of values for liquid density and thermal conductivity is to ensure significantly increased heat diffusion in the liquid so that the interface always remains close to saturation temperature. Figures 5.3 and 5.4 show respective plots of the interface position $x_i(t)$ and instantaneous temperature profiles $T(x)$ from our numerical simulation and Neumann's analytical solution. The results show good agreement.

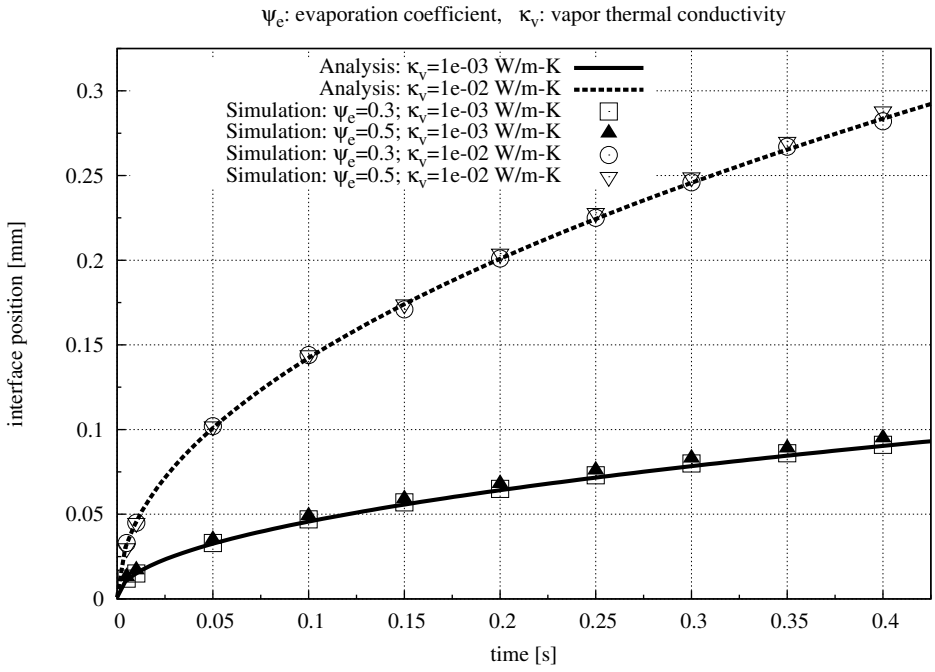

Figure 5.3: Interface position as a function of time for Stefan problem

5.3.2 Evaporation Heat Transfer Coefficient

Table 5.1 shows flow and heating conditions (obtained from experimental studies by Abdulmalik *et al.*, 1998) for the numerical simulation of wavy laminar falling film evaporation of water. The liquid and vapor properties for these simulations were

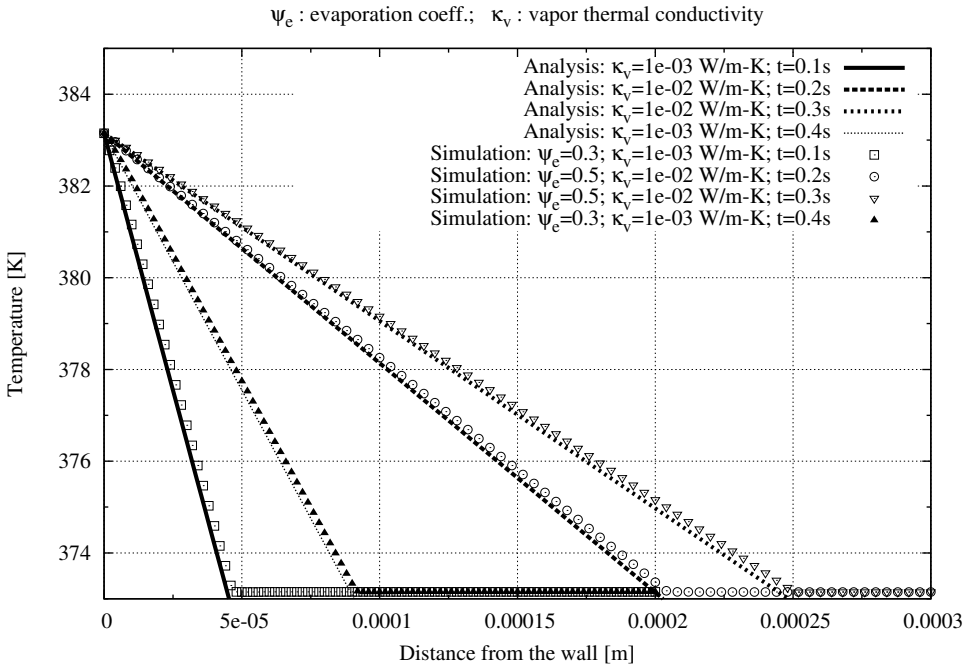

Figure 5.4: Temperature profile at different time steps for the Stefan problem

set at their corresponding saturation values (Incropera *et al.*, 2007). The length of the evaporator computation domain is 0.5m and is uniformly discretized with grid sizes $0.22\delta_{_N}$ and $0.05\delta_{_N}$ in the streamwise and normal directions respectively. Time step for the computation was set at $\triangle t = 6.0\,\mu$s. Based on the Nusselt film height $\delta_{_N}$ and Nusselt film velocity $u_{_N}$, we define a flow time scale $\tau_{_N} = \delta_{_N}/u_{_N}$. To ensure simulations run until flow attains equilibrium, the stop time was set at $t_{\text{stop}}/\tau_{_N} \geq 2000$ which is equivalent to about $250,000$ time steps. The frequency of inlet perturbation was fixed at $f = 30$ Hz for all simulations, which is much less than the cut-off frequency (Gao *et al.*, 2003) beyond which flow perturbations are damped out.

Based on Newton's law of cooling, the local evaporation heat transfer coefficient is defined as:

$$h(x,t) = \frac{q^{''}}{T_w(x,t) - T_i(x,t)} \tag{5.7}$$

where $T_w(x,t)$ is the local wall temperature, $T_i(x,t)$ is the corresponding interfacial

Table 5.1: Transport and heating conditions for falling film evaporation simulations. $Ka^* = 1/Ka^3$ (Abdulmalik *et al.*, 1998) is evaluated using fluid properties at temperature $T_m = (\bar{T}_w + T_{sat})/2$, where $\bar{T}_w$ is the time-average mean wall temperature.

Case #	T_{sat} [K]	Heat flux [Wm^{-2}]	Re	Ka^*
1	311.65	19500	200	5.09317e-12
2	311.65	19500	250	5.06420e-12
3	372.75	18200	300	2.92891e-13
4	372.75	18200	350	2.92220e-13

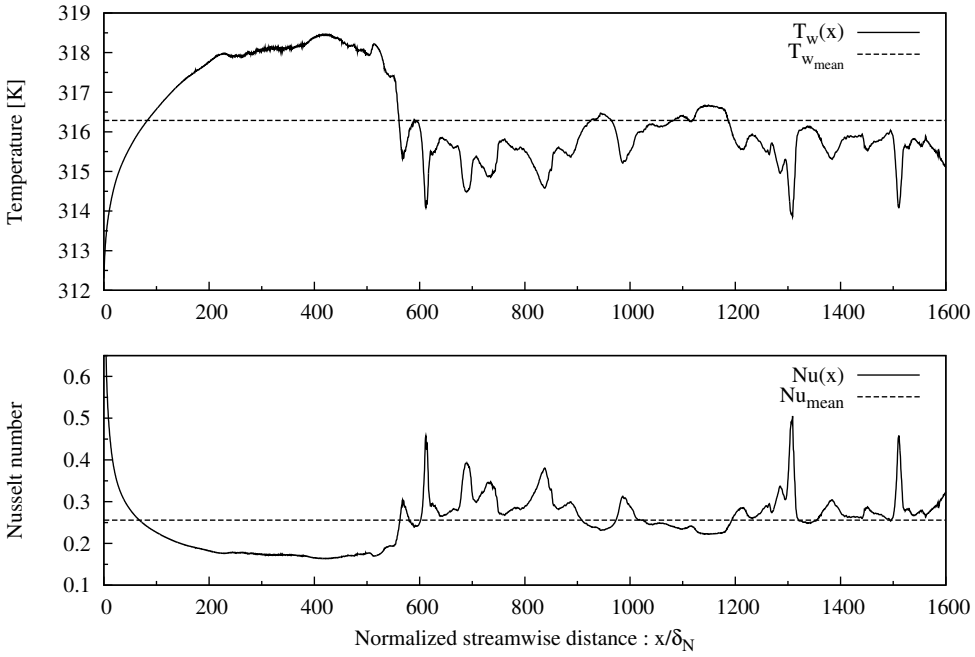

Figure 5.5: Instantaneous streamwise and corresponding mean values of Nusselt number and wall temperature for case 1.

temperature and q'' is the constant heat flux at the evaporator wall. The time-averaged mean evaporation heat transfer coefficient $\bar{h}$ for the falling liquid film is defined as :

$$\bar{h} = \frac{1}{N_j} \sum_j \frac{1}{L_e} \int_0^{L_e} h(x, t_j) dx \qquad j = 1, 2, ..., N_j \tag{5.8}$$

where N_j is the number of time steps over which the average is evaluated, L_e is the evaporator length, $h(x, t_j)$ is the instantaneous heat transfer coefficient (see figure 5.5) at time t_j. Following (5.8), the time-averaged mean Nusselt number $\bar{Nu}$ for the

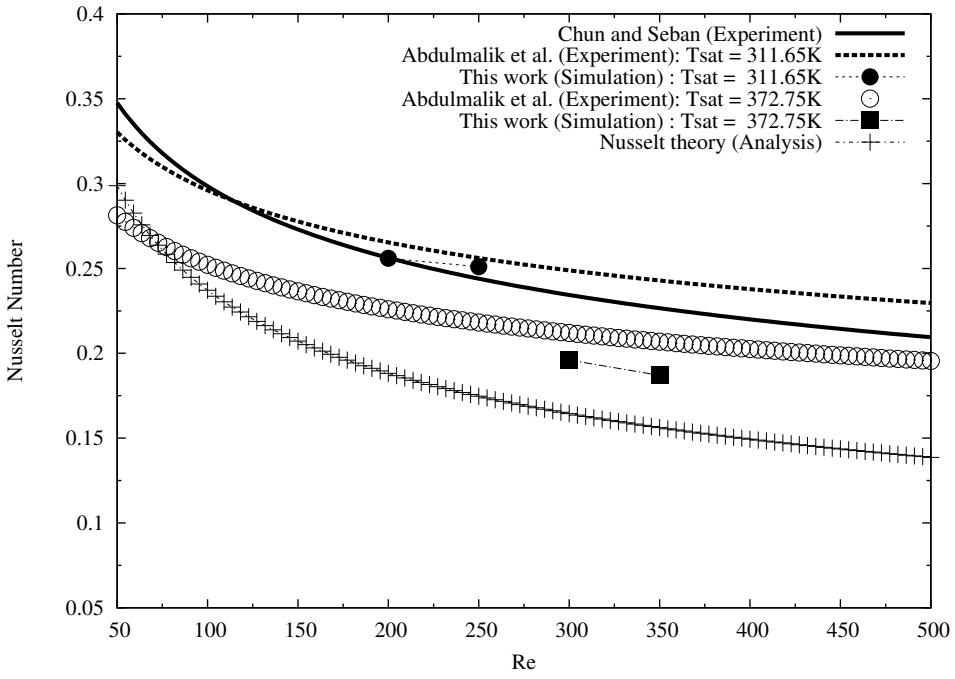

Figure 5.6: Simulated average Nusselt number for the cases in table 5.1 compared with predictions from Nusselt (1916) flat film theory and correlations from Chun & Seban (1971); Abdulmalik *et al.* (1998).

evaporating falling liquid film is expressed as (Abdulmalik *et al.*, 1998):

$$\bar{Nu} = \frac{\bar{h} l_v}{\kappa_l} \tag{5.9}$$

$l_v = (\nu_l^2/g)^{1/3}$ is the viscous length scale. Based on experimental studies, Chun & Seban (1971) and Abdulmalik *et al.* (1998) proposed the following correlations for the average Nusselt number for falling film evaporation in the wavy-laminar flow regime:

$$\bar{Nu} = 0.822\, Re^{-0.22} \qquad \text{(Chun \& Seban)} \tag{5.10a}$$

$$\bar{Nu} = 2.65\, (Ka^*)^{0.0563}\, Re^{-0.158} \qquad \text{(Abdulmalik et al.)} \tag{5.10b}$$

Figure 5.6 shows plots of the average Nusselt number calculated from numerical simulation of the cases in table 5.1 and predictions using (5.10a) and (5.10b). The general trend of the numerical results is consistent with the experimental correlations as exemplified by higher values of Nu compared to Nusselt flat film theory and a decrease

in Nu with Re in the wavy-laminar regime. Overall, the results show good agreement with the experimental correlations.

5.4 Analysis of Simulation Results

5.4.1 Free Surface Waves Evolution

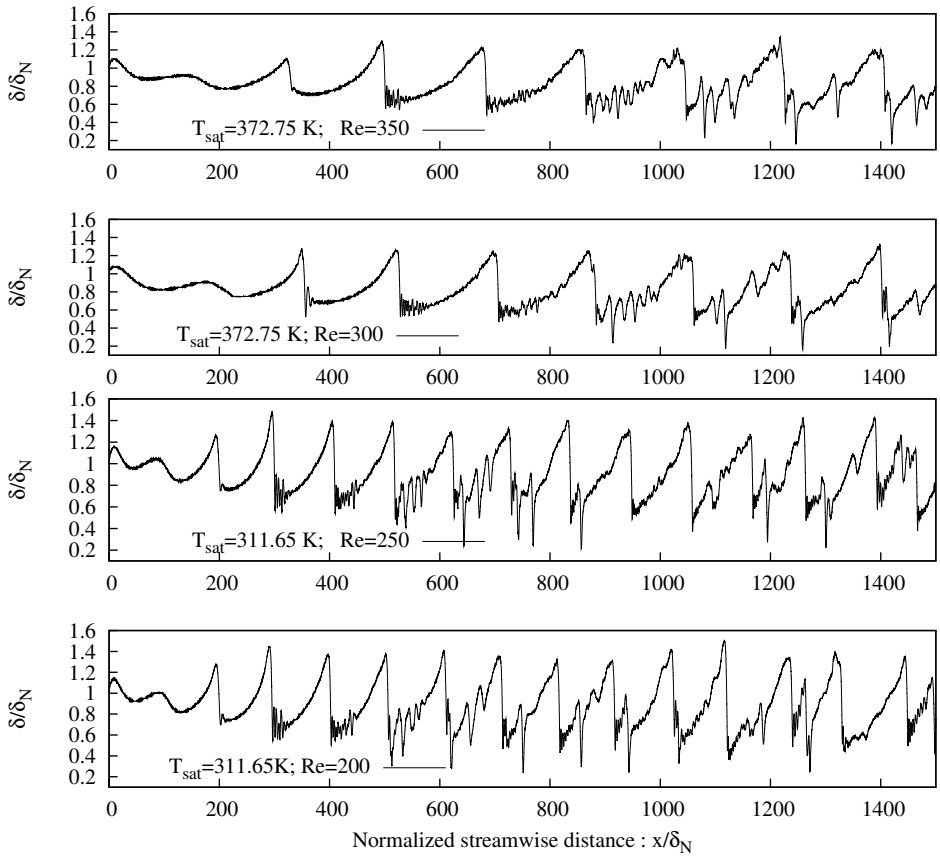

Figure 5.7: Free surface wave profiles for simulated water falling films at different Reynolds numbers and saturation temperatures.

Figure 5.7 shows free surface wave profiles of evaporating falling water films for the different Reynolds numbers simulated in this study. The frequency of inlet perturbation for all cases is fixed at $f = 30\,\mathrm{Hz}$. Close to the inlet, the interface is characterized by growing amplitude of flow perturbation. Once the disturbance grows to saturation, the saturated surface wave travels as a solitary wave over a streamwise distance of about 2 - 3 times the average wave separation where capillary waves gradually

develop in front of the saturated wave. Over this streamwise distance, the number of capillary waves formed increase as the wave continues downstream. The amplitude of the saturated wave and the minimum film thickness (corresponding to the height of the film at the solitary wavefront) remains uniform in this flow region.

Figure 5.8: Film free surface waves profiles for case 1 showing saturated solitary wave preceded by: multiple capillary waves only (top); fewer capillary waves and an intermediate-sized wave (bottom). The red color defines the liquid film while blue defines the vapor film and flow is from left to right.

As the solitary-capillary wave-train continues downstream, the preceding capillary waves interact, giving rise to intermediate-sized waves (i.e. the amplitude is greater than capillary waves' but less than saturated solitary waves') between consecutive saturated solitary waves (see figures 5.7 and 5.8). The transition from capillary to intermediate-sized waves can also be characterized in terms of the reduction in multiplicity of capillary waves in front of large amplitude solitary waves. The growth in amplitude of the intermediate-sized waves results in significant reduction in film thickness at the intermediate wavefront leading to an overall reduction in mean film thickness. Further downstream where the film contains fully developed intermediate-sized waves, the saturated solitary waves still retain their uniform amplitude and wave separation.

5.4.2 Wave Properties Compared to 2-D Correlations

Figure 5.9 shows plots of simulation results for wave properties (non-dimensional wave speed and maximum wave height) for the cases in table 5.1 compared with correlations from Nosoko *et al.* (1995). The values for wave speed and wave separation were evaluated from the flow region dominated by regularly spaced fully developed solitary waves while the peak wave height was determined considering waves in the entire flow domain. The plots show that the correlations overstate the maximum wave height while under-predicting the wave speed. The variation in wave height between the simulations and correlations is more pronounced. The results indicate that the correlations proposed by Nosoko *et al.* (1995) are not suitable for estimating falling film wave properties for moderately high Reynolds number ($200 < Re < 500$) flows. This is consistent with the fact that the experiments for which the correlations were developed applied to falling films with flow Reynolds numbers in the range $Re = 15 - 90$. The significant over-prediction (compared to simulation results) of the maximum wave height by the low Reynolds number correlations of Nosoko *et al.* (1995) underscores the influence of intermediate waves on the reduction of overall film thickness for moderately high Reynolds number falling films.

5.4.3 Streamwise Thermal Regions

From the plots in figure 5.5, the following distinct thermal regions with respect to the streamwise variation of the wall temperature or heat transfer coefficient can be defined for the case of constant wall heat flux:

- region of growing wall temperature close to the inlet.
- an intermediate region of relatively uniform wall temperature.
- region of fluctuating wall temperature beyond the intermediate region.

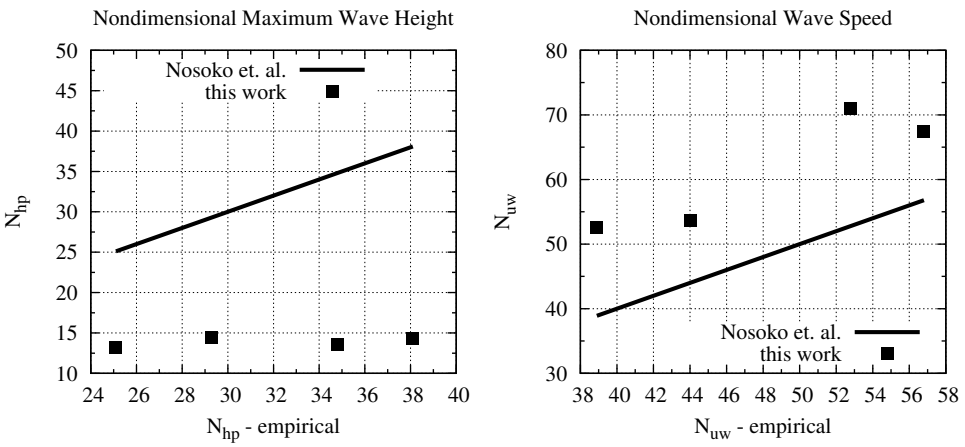

Figure 5.9: Simulated non-dimensional maximum wave height N_{hp} and non-dimensional wave speed N_{uw} for water falling films at moderately high Reynolds numbers (see table 5.1) compared with Nosoko *et al.* (1995) correlations.

These regions are indicative of the influence of wave evolution on the development of liquid film thermal conditions and consequently evaporation heat transfer. Figure 5.10 shows plots of the streamwise distribution of wall temperature for the four cases corresponding to figure 5.7. The plots show that for the film flows at both higher saturation temperature and Reynolds number, the wall temperature in the fluctuating region does not deviate significantly from the value in the intermediate region.

5.4.3.1 Growing Wall Temperature

The region of growing wall temperature is characterized by a developing thermal boundary layer. Although liquid enters the evaporator at saturation conditions, evaporation only occurs at the interface when the interfacial surface-normal temperature gradient is positive or in this formulation $T_i - T_{sat} > 0$. The consequence of this free surface thermal constraint is that a thermal boundary layer develops in the liquid film at the entrance region. Figure 5.11 shows plots of the normal distribution of temperature in the liquid film at the entrance region depicting a growing thermal boundary layer. As the thermal boundary layer grows to fill the liquid film, the wall temperature approaches a local maximum. From figure 5.10 we observe that the wall

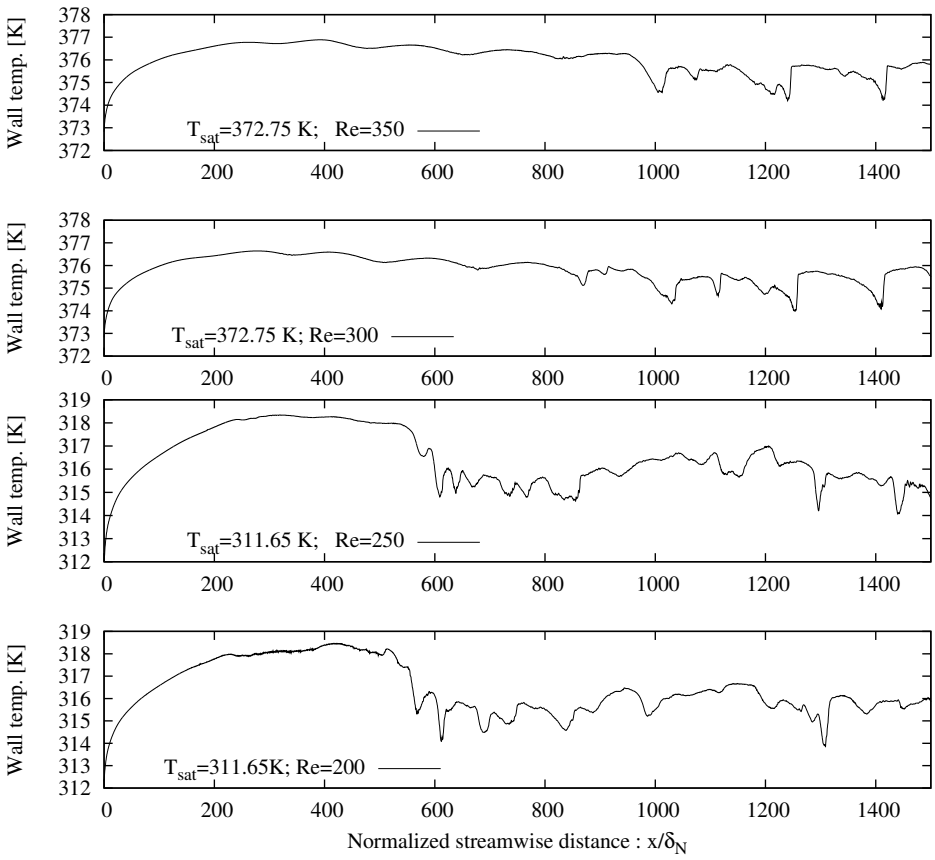

Figure 5.10: Streamwise variation of wall temperature for simulated water fall films at different Reynolds numbers and saturation temperatures.

temperature attains its first maximum around $x/\delta_{_N} \approx 240$ for case 1 ($Re = 200$, $T_{sat} = 311.65$K, $\delta_{_N} = 0.3\,$mm, $Pr = 4.47$) and $x/\delta_{_N} \approx 200$ for case 3 ($Re = 300$, $T_{sat} = 372.75$K, $\delta_{_N} = 0.2\,$mm, $Pr = 1.77$). The shorter length of the thermal entrance region for the higher temperature liquid film is consistent with the relative increase in diffusion due to lower liquid Prandtl number and an overall relatively thinner film.

5.4.3.2 Near-Uniform Wall Temperature

Once the thermal region becomes fully developed, the wall temperature remains relatively uniform over a few wavelengths downstream. Although the onset of the region of near-uniform wall temperature is largely dependent on the length of the thermal entrance region, its extent in the streamwise direction is almost entirely defined by the

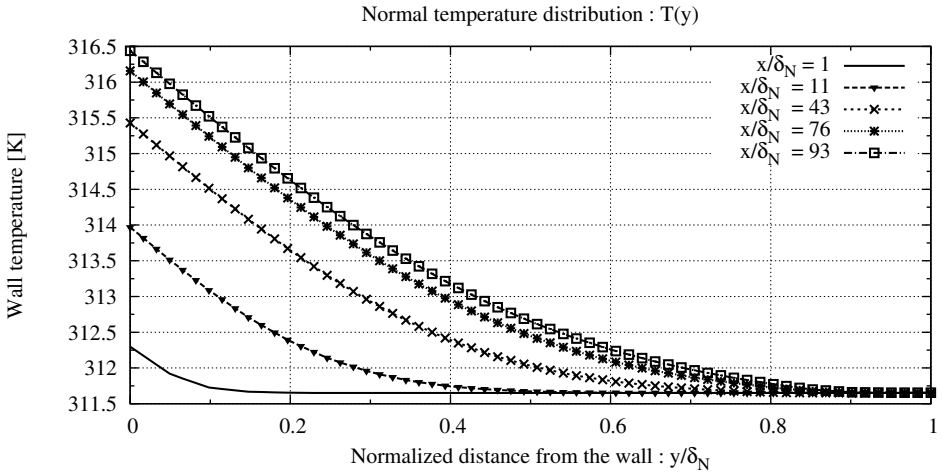

Figure 5.11: Crosswise temperature distribution in the thermal boundary layer at the entrance region for case 1 showing decreasing growth in wall temperature with streamwise distance.

evolution of the free surface waves. For all cases simulated in this study, the termination point for the near-uniform wall temperature region coincides with the flow region where capillary waves' interaction leads to formation of intermediate-sized waves (see figures 5.7 and 5.10). This implies that in the region where the flow is in a strict sense dominated by purely saturated solitary-capillary waves, the wall temperature (and consequently heat transfer coefficient) remains approximately uniform. Figure 5.5 shows that the instantaneous heat transfer coefficient in this region is less than the mean heat transfer coefficient integrated over the evaporator length.

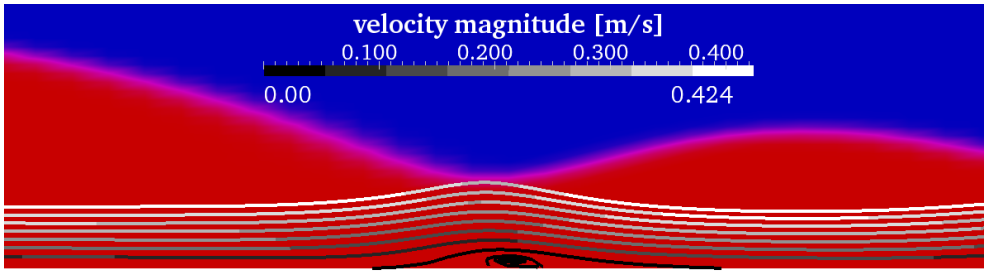

Figure 5.12: Liquid film streamlines for case 1 showing flow separation at the wavefront of the solitary wave ($x/\delta_N = 404$; see figures 5.7 and 5.13) in the region where the wall temperature is approximately uniform.

Studies (Kunugi & Kino, 2005; Dietze *et al.*, 2008, 2009) show that the onset

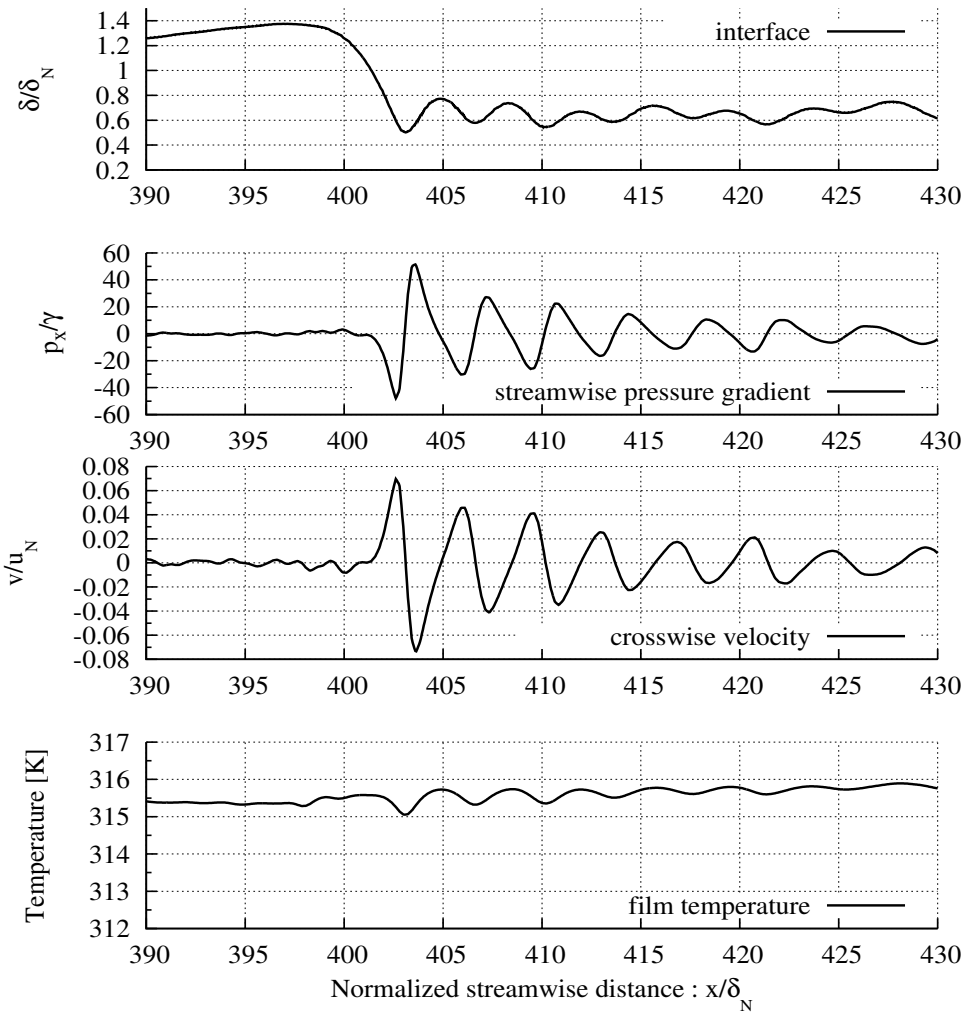

Figure 5.13: Plots of film interface in the region of near-uniform wall temperature showing solitary and multiple capillary waves, normalized streamwise pressure gradient $p_x(=\frac{\partial p}{\partial x})/\gamma$, normalized crosswise velocity $v/u_{_N}$ and film temperature for case 1. The streamwise values for velocity, pressure gradient and film temperature were sampled at $y = 75\mu$m from the wall. γ is the specific weight of the liquid.

of capillary waves in constant property low Reynolds number (e.g. $Re < 80$) vertical falling liquid films with long wavelength disturbances is typically accompanied by flow separation (or backflow) with the resultant effect of convective heat transfer enhancement. In our simulations, flow separation is also observed in the region of uniform wall temperature where multiple capillary waves are formed ahead of a saturated solitary wave (see figure 5.12). However the size of the backflow separation

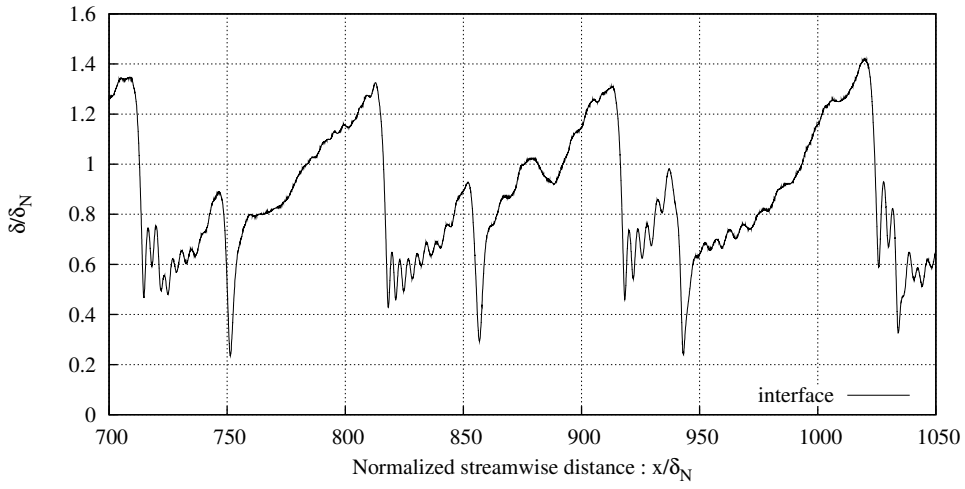

Figure 5.14: Interface profile showing fully developed intermediate waves between saturated solitary waves in the region of fluctuating wall temperature for case 1.

vortex is much smaller (see § 4.4.2 for discussion on backflow dynamics). This is due to higher liquid streamwise momentum which dampens the impact of the adverse streamwise pressure gradient primarily responsible for the formation and growth of the separation vortex at the solitary-capillary wavefront. Consequently, the crosswise velocity (see figure 5.13) induced by backflow does not result in significant convective transport from the wall to the interfacial boundary. This underscores a fundamental difference between low and moderately high Reynolds number falling films in terms of the effect of backflow in heat transfer enhancement in the solitary-capillary waves regime.

Fourier's law applied at the evaporator surface for a thin liquid film of thickness $\delta(x,t)$ can be expressed as:

$$q^{"} = -\kappa_l \frac{\partial T}{\partial y}\bigg|_{y=0} = \frac{\kappa_l \big(T_w(x,t) - T_i(x,t)\big)}{\delta(x,t)} + O\left(\delta(x,t)\right) \tag{5.11}$$

With $T_i \approx T_{sat}$, the streamwise derivative of (5.11) for constant heat flux and thermal conductivity gives:

$$\frac{\partial T_w}{\partial x} \approx \frac{q^{"}}{\kappa_l}\frac{\partial \delta}{\partial x} \tag{5.12}$$

Equation (5.12) indicates that in the fully developed thermal region, the wall (or

near-wall region of the liquid film) temperature varies as the film thickness for constant wall heat flux. Figure 5.13 (bottom plot) shows the liquid film temperature parallel to the wall at $y/\delta_N = 0.25$ (or $y = 75\mu$m) for case 1. The streamwise variation of temperature is consistent with equation (5.12) (see temperature and interface plots). The plot shows that across each wave, the minimum temperature (or highest heat transfer rate) occurs at the wavefront where the film thickness for that wave is smallest. Within the large solitary wave where $\frac{\partial \delta}{\partial x} \approx 0$ the temperature remains uniform. The results clearly show that in the region of near-uniform wall temperature, heat transfer from the wall is highly dependent on film thickness and consequently dominated by conduction and any transport enhancement from crosswise convective effects resulting from backflow or large wave circulation is minimal or negligible.

5.4.3.3 Fluctuating Wall Temperature

With regards to heat transfer, the most consequential effect of the intermediate surface waves is the significant reduction in film thickness at the intermediate wavefront i.e. the flow region between consecutive saturated solitary waves (see figure 5.14). As predicted by equation (5.12), the liquid film near-wall temperature approaches its minimum value at the intermediate wavefront where the film thickness is smallest before growing back to the average value fixed by the film height at the solitary-capillary wavefront upstream of the intermediate wave (see figure 5.15). This repeated process due to the presence of intermediate waves between saturated solitary waves give rise to the region of fluctuating wall temperature (see figure 5.5). The heat transfer enhancement for the entire falling film is largely dependent on the presence and structure (e.g. minimum film thickness at wavefront) of the intermediate waves. Figure 5.5 shows that in this region, the heat transfer coefficient is typically greater than the mean value integrated over the evaporator length.

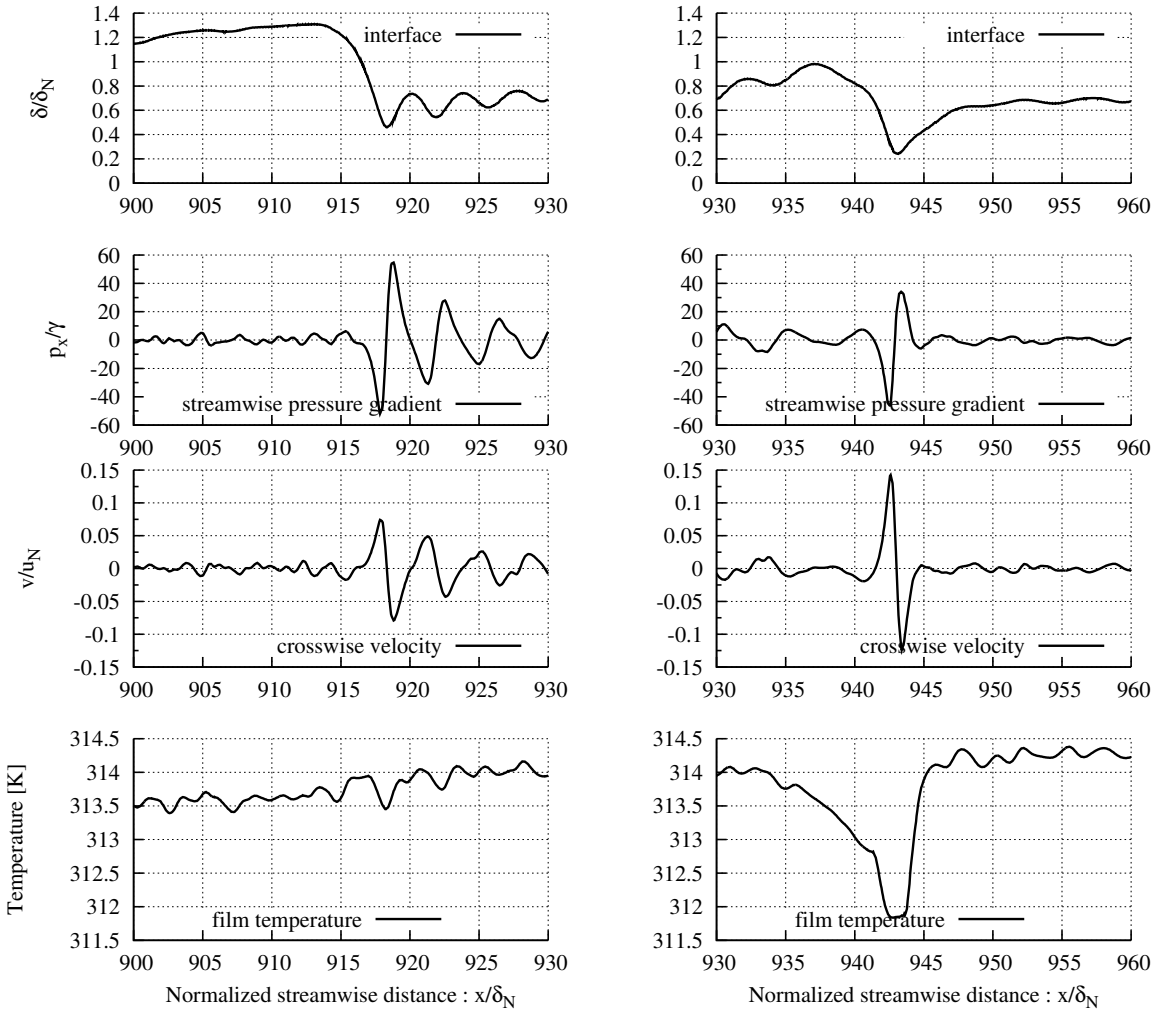

(a): Solitary-capillary waves (b): Intermediate wave

Figure 5.15: Plots of film interface in the region of fluctuating wall temperature showing solitary-capillary waves and the intermediate wave (see figure 5.14) and their corresponding normalized streamwise pressure gradient $p_x(= \frac{\partial p}{\partial x})/\gamma$, normalized crosswise velocity $v/u_{_N}$ and film temperature for case 1. The streamwise values for velocity, pressure gradient and film temperature were sampled at $y = 75\mu$m from the wall.

In addition to increased heat transport by diffusion, the normalized crosswise velocity at the intermediate wavefront (see figure 5.15) also indicate increased convective transport. Figure 5.15 shows that even though the streamwise pressure gradient across the solitary wavefront is greater than the value across the intermediate wavefront, the crosswise velocity induced by the pressure gradient is about three times

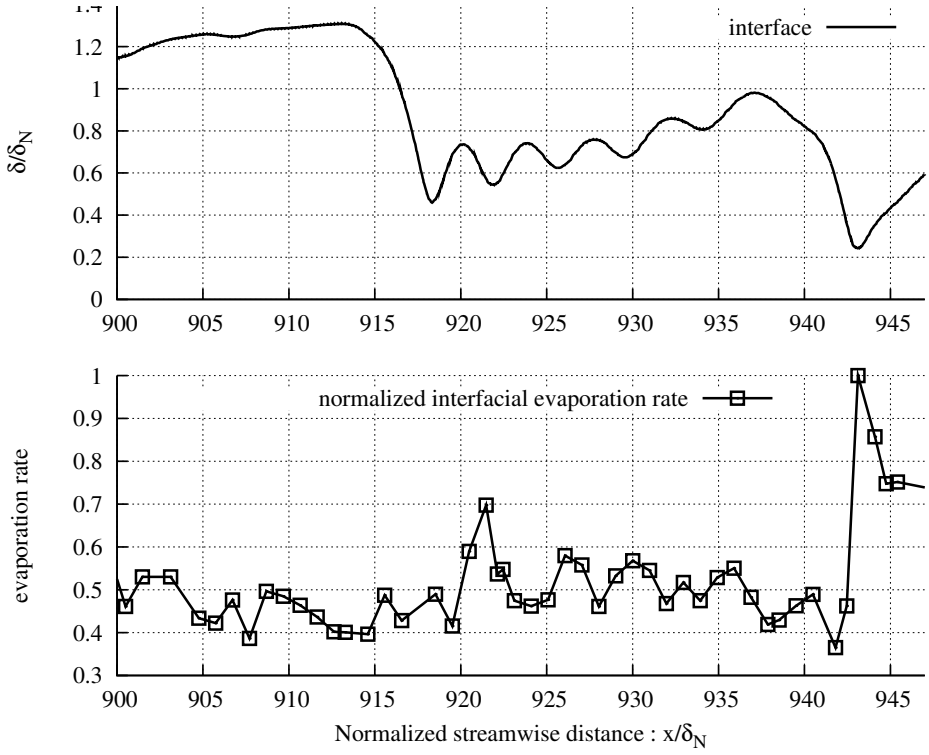

Figure 5.16: Interfacial evaporation rate along the solitary-capillary-intermediate wave train in the region of fluctuating wall temperature (see figures 5.14 and 5.15) for case 1. The evaporation rate is normalized by the value at the intermediate wavefront.

higher at the intermediate wavefront. This is a consequence of the combined effect of significant reduction in film thickness at the intermediate wavefront which induces higher velocities to satisfy the continuity constraint.

5.4.4 Evaporation Rates along Waves

Figure 5.16 shows the normalized rate of evaporation at the film interface across a fully developed solitary-capillary-intermediate wave train in the region of fluctuating temperature. The plots show that the maximum evaporation rate occurs at the intermediate wavefront where the film is thinnest. This is due to a combination of conduction and convective effects. Across the solitary wave, the average evaporation rate is less than the average rate across the multiple capillary waves in front of the solitary wave. In general the average evaporation is highest at the intermediate

wavefront (smallest film thickness and highest crosswise velocity) and least within the solitary wave (highest film thickness and lowest crosswise velocity). Within the core of the large amplitude solitary waves, we found no evidence of flow circulations zones similar to backflow regions that evolve at the wavefront of solitary-capillary waves (see figure 5.12).

CHAPTER 6

FALLING FILM EVAPORATION OF BLACK LIQUOR

6.1 Background

Black liquor is a highly viscous liquid residual stream from the pulp production process that needs to be recycled due to environmental and economic reasons (Gourdon, 2011). The evaporation process is one of the critical unit operations in the recovery cycle of pulp mills since the efficiency of the cycle is largely dictated by evaporator performance. To minimize the extent of evaporator heat transfer surface fouling due to crystallization, falling film evaporation is typically employed for black liquor concentration (Chen & Gao, 2003). Black liquor mixture consist of dissolved solids (soluble salts, wood extractives) that is enriched during evaporation. The transport properties of black liquor are dependent on temperature and dry solids mass fraction, and its rheology could be Newtonian at low dry solids mass fraction or non-Newtonian (shear-thinning) at dry solids mass fraction greater than 0.5 (Adams *et al.*, 1997). Even under conditions where black liquor flow is Newtonian, the combination of high density and viscosity coupled with relatively low surface tension coefficient could induce complex interfacial flow structures.

Dissolved solids enrichment during black liquor evaporative concentration is primarily responsible for crystallization fouling. For most Kraft black liquor mixtures, sodium carbonate (Na_2CO_3) and sodium sulfate (Na_2SO_4) are the major inorganic species. Under certain thermophysicial conditions, enriched soluble salts crystallize out of the evaporating mixture, forming scales that deposit on evaporator surface (see for example Hedrick & Kent, 1992; Shi *et al.*, 2003; DeMartini & Verrill, 2007; Gourdon *et al.*, 2009; Gourdon, 2011). Research studies have been conducted to

characterize the kinetics and predict conditions under which black liquor salts crystallize. Grace (1975) defined the maximum solubility of Na_2CO_3 and Na_2SO_4 in a black liquor mixture as the critical solids point beyond which soluble salt crystallize. Rosier (1997) proposed predictive correlations for black liquor soluble salt precipitation. Chen & Gao (2003) discuss the inverse solubility property of black liquor with implication that dissolved salt have reduced solubility with increasing temperatures of black liquor mixtures. Gourdon (2009) developed methods for investigating variation in evaporator heat transfer coefficient due to soluble scale fouling.

Falling film hydrodynamics and heat transfer of evaporating black liquor under laminar and turbulent flow conditions has been studied experimentally (Johansson, 2008; Johansson *et al.*, 2009*a*,*b*) and numerically (Chen & Gao, 2003). Johansson *et al.* (2009*a*) characterized fundamental differences in free surface wave flow structures for evaporating falling films of water and black liquor at similar film Reynolds number. In particular bubble formation was observed only in evaporating black liquor falling films, which was attributed to a combination of surface-active agents and air/vapor entrainment due to free surface wave-breaking. Johansson *et al.* (2009*b*) proposed correlations for predicting black liquor falling film evaporation heat transfer coefficient for laminar, turbulent and transition flow regimes. Chen & Gao (2003) simulated black liquor falling film evaporation based on elliptic incompressible Navier-Stokes equations in 2-D. They assumed a flat free surface for the falling film with liquid vaporization occurring within the film as opposed to free surface evaporation. The numerical implementation of Chen & Gao (2003) also includes a phenomenological model for heat transfer surface fouling due to dissolved solids solid enrichment.

This chapter focuses on the analysis of Newtonian wavy-laminar 2-D (flat plate) and 3-D (cylindrical) black liquor falling films based on numerical solution of the transient Navier-Stokes equations on highly resolved spatio-temporal grids. Conservation laws for the transport of heat and species are implemented with source terms

describing interfacial evaporation and species enrichment/depletion. The study investigates the fundamental structure of fully developed black liquor falling film interfacial waves at low and moderately high dry solid mass fraction for specified flow inlet perturbation. We analyze free surface wave phenomena such as wave breaking and air entrainment for films with moderately high dry solid mass fraction. For fully developed waves, we investigate the influence of wavy film transport on temperature and species distribution and the possible implications for crystallization and soluble scaling.

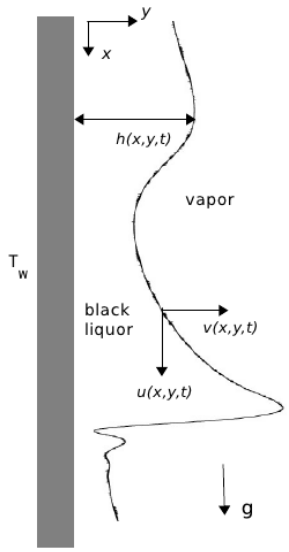

Figure 6.1: 2-D schematic diagram of a black liquor falling film heated by uniform temperature wall: u, v are x, y velocity components, h is wave height, T_w is uniform wall temperature, $\mathbf{g}$ is gravitational acceleration.

6.2 Mathematical Model

We consider the wavy-laminar flow of Newtonian black liquor mixture down a vertical wall (flat or cylindrical) maintained at constant temperature T_w (see figure 6.1 for the 2-D illustration). It is customary to represent all soluble salts in the black liquor mixture in terms of an overall dry solids mass fraction (Golike *et al.*, 1998; Gourdon, 2009). Individual salts concentrations can be expressed as a function of this fraction. For evaporating flow, inlet temperature for black liquor and steam is specified by the

boiling point rise corresponding to the inlet dry solids mass fraction. Species (i.e. dry solids mass fraction) conservation law accounts for dry solids enrichment as a result of liquid vaporization and depletion due to salt precipitation.

6.2.1 Governing Equations

Based on the single-field formulation, the respective continuity, momentum, energy, species and phase equations for the two-phase flow field are expressed as:

$$\frac{\partial \rho}{\partial t} + \boldsymbol{\nabla} \cdot (\rho \boldsymbol{v}) = 0 \tag{6.1a}$$

$$\frac{\partial \rho \boldsymbol{v}}{\partial t} + \boldsymbol{\nabla} \cdot (\rho \boldsymbol{v}\boldsymbol{v}) = -\boldsymbol{\nabla} p + \boldsymbol{\nabla} \cdot \boldsymbol{\tau} + \rho \mathbf{g} + \int_{A_\mathrm{I}(t)} \sigma \kappa' \boldsymbol{n}' \delta_\mathrm{I}(\boldsymbol{x} - \boldsymbol{x}') \, \mathrm{d}A_\mathrm{I} \tag{6.1b}$$

$$\frac{\partial \rho c_p T}{\partial t} + \boldsymbol{\nabla} \cdot (\rho \boldsymbol{v} c_p T) \; = \; \boldsymbol{\nabla} \cdot (k \boldsymbol{\nabla} T) + \boldsymbol{\tau} : \boldsymbol{\nabla} \boldsymbol{v} - \dot{S}_{q,e} + \dot{S}_{q,c} \tag{6.1c}$$

$$\frac{\partial \rho \chi_s}{\partial t} + \boldsymbol{\nabla} \cdot (\rho \boldsymbol{v} \chi_s) \; = \; \boldsymbol{\nabla} \cdot (\rho \, \xi \boldsymbol{\nabla} \chi_s) + \dot{S}_{m,e} - \dot{S}_{m,c} \tag{6.1d}$$

$$\frac{\partial \alpha}{\partial t} + \boldsymbol{\nabla} \cdot (\boldsymbol{v} \alpha) = -\dot{S}_v \tag{6.1e}$$

where $\boldsymbol{v}$ is velocity, $\boldsymbol{\tau}$ is the stress tensor, p is pressure, T is temperature, χ_s is mass fraction of dissolved solids (i.e. species) in the black liquor mixture and α is phase volume fraction. $\dot{S}_{q,e}$ and $\dot{S}_{m,e}$ represent the respective heat and mass source terms resulting from liquid vaporization. $\dot{S}_{q,c}$ and $\dot{S}_{m,c}$ represent the respective heat and mass source terms from species depletion. Conservation of mass fraction in the liquid film ensures that the mass rate of liquid vaporization equals the mass rate of species enrichment. The physical presence of salt crystals in the liquid film due to crystallization is not explicitly captured in this formulation. Rather, the species depletion terms account for dissolved solids mass fraction destruction when salt concentration levels attain or exceed supersaturation states. Species transport occurs in the liquid film only. $\dot{S}_v$ is the rate of liquid vaporization and tracks the liquid interface due to evaporation of liquid only i.e. no condensation effects are considered. The energy transport equation (6.1c) also accounts for viscous dissipation since black liquor flow is typically characterized by relatively large velocity gradients

and high viscosity. The viscous dissipation term is treated explicitly in the numerical implementation.

6.2.2 Evaporation Source Terms

Free surface evaporation of black liquor is driven by an excess temperature $T_i - T_{sb}$ at the phase boundary where T_i is the interfacial temperature and T_{sb} is defined as:

$$T_{sb} = T_{\text{sat}} + \triangle T_{\text{BPR}} \tag{6.2a}$$

$$\triangle T_{\text{BPR}} = \text{BPR}_{50} \left[\frac{9.1\chi_s}{8.1 - 7.1\chi_s} \right] \tag{6.2b}$$

$\triangle T_{\text{BPR}}$ is the boiling point rise expressed as a function of the dry solid mass fraction (see TAPPI manuscripts by Clay, 2011) and BPR_{50} is the boiling point elevation for a black liquor mixture with $\chi_s = 0.5$. T_{sat} is the saturation temperature at the specified saturation pressure. The vaporization heat flux density j_e^h at the phase boundary is evaluated (Tanasawa, 1991) based on the excess temperature:

$$j_e^h = \frac{T_i - T_{sb}}{R_e^i} \tag{6.3}$$

where the interfacial evaporation heat transfer resistance R_e^i is defined (see Kunkelman & Stephan, 2009) as:

$$R_e^i = \left[\frac{2\psi_e}{2 - \psi_e} \frac{h_e^2}{\sqrt{2\pi R_{gas}}} \frac{\rho_g}{T_{\text{sat}}^{3/2}} \right]^{-1} \tag{6.4}$$

h_e and R_{gas} are the respective enthalpy of vaporization and gas constant of water at saturation conditions. ψ_e is evaporation coefficient which is set to 0.5 in our simulations. With the interfacial area evaluated based on the model of Hardt & Wondra (2008), the evaporation source terms are defined as:

$$\dot{S}_{q,e} = \frac{j_e^h}{V} \int_V |\boldsymbol{\nabla}\alpha| \, \mathrm{d}V \tag{6.5a}$$

$$\dot{S}_{m,e} = \frac{\dot{S}_{q,e}}{h_e} \tag{6.5b}$$

$$\dot{S}_v = \frac{\dot{S}_{m,e}}{\rho_l} \tag{6.5c}$$

V is volume.

6.2.3 Phenomenological Crystallization Model

The mass and heat source terms for species depletion due to salt crystallization are derived based on the phenomenological model for black liquor fouling thermal resistance of Chen & Gao (2003) . The fouling resistance model follows from an extension of the empirical models for predicting heat transfer fouling proposed by Muller-Steinhagen & Branch (1997); Forster *et al.* (1999). Chen & Gao (2003) assumes that all precipitated salt resulting from elevated concentration due to species enrichment is deposited on the heat transfer surface. Thus, the derivation of the fouling thermal resistance starts with a rate equation for mass m_s of black liquor salt precipitated per unit volume:

$$\frac{\partial m_s}{\partial t} \;=\; K_r \left(C_b - C^*\right) \tag{6.6}$$

where K_r is the surface rate constant, C_b is soluble solids mass concentration in the bulk flow and C^* depends on the weight percent of sodium salts in the black liquor mixture. Equation (6.6) is based on the following simplifying assumptions (Chen & Gao, 2003):

1. the deposition process is controlled by a first order chemical reaction on the heat transfer surface i.e. the exponent n of the concentration difference is assigned a value of one, and the surface rate constant is evaluated based on temperature conditions at the evaporator wall.

2. the driving force for the reaction is the positive species concentration gradient.

3. the system is considered quiescent and diffusion controlled.

By assuming that the surface rate constant follows Arrhenius equation, K_r is expressed as:

$$K_r = \bar{K_r} \exp\left(\frac{-E_{\text{act}}}{R\,T_w}\right) \tag{6.7}$$

where $\bar{K_r}$ is the pre-exponential factor and R is the universal gas constant. The rate of fouling resistance R_{FR} can be expressed in terms of the fouling deposit density ρ_d, deposit thermal conductivity k_d and the mass rate of precipitation per unit deposit area A_d, i.e.:

$$\rho_d k_d \frac{\partial R_{\text{FR}}}{\partial t} \;=\; \frac{1}{A_d} \int_V \frac{\partial m_s}{\partial t}\, \mathrm{d}V \tag{6.8}$$

Using dimensional analysis the expression on the rhs of equation (6.8) can be reformulated in terms of the thermal diffusion length scale l_{T}:

$$\frac{1}{A_d} \int_V \frac{\partial m_s}{\partial t}\, \mathrm{d}V \approx \frac{V}{A_d} \frac{\partial m_s}{\partial t} \;\equiv\; l_{\text{T}} \dot{S}_{m,c} \tag{6.9}$$

l_{T} is defined in terms of the viscous length scale l_v (see § 1.4.2) i.e.

$$l_{\text{T}} = \frac{l_v}{Pr^{2/3}} \tag{6.10}$$

In our simulations, the viscous length scale and Prandtl number are evaluated using inlet conditions of the black liquor mixture. From equations (6.8) and (6.9), the mass rate of species depletion can be expressed in terms of the rate of fouling resistance:

$$\frac{l_{\text{T}}}{\rho_d k_d} \dot{S}_{m,c} \;=\; \frac{\partial R_{\text{FR}}}{\partial t} \tag{6.11}$$

Based on analysis of experimental data on heat transfer fouling reported by Forster *et al.* (1999), Chen & Gao (2003) expressed the rate of fouling thermal resistance as:

$$\frac{\partial R_{\text{FR}}}{\partial t} = \frac{K_{\text{a}}}{\rho_d k_d} \exp\left(\frac{-E_{\text{act}}}{R\,T_w}\right) (C_b - C^*) \tag{6.12}$$

Combining equations (6.11) and (6.12), the respective mass and heat source terms for the species and energy conservation laws resulting from species depletion due to crystallization can be expressed as:

$$\dot{S}_{m,c} = \frac{Pr^{2/3}}{l_v}\, \rho_l K_{\text{a}} \exp\left(\frac{-E_{\text{act}}}{R\,T_w}\right) (\chi_s - c^*) \tag{6.13a}$$

$$\dot{S}_{q,c} = \triangle H_s^o \dot{S}_{m,c} \tag{6.13b}$$

Table 6.1: Mean values of typical components of black liquor dry solids (Gourdon, 2009)

Analyte	Mean value
Na_2CO_3, wt %	10.0
Na_2SO_4, wt %	6.03
Na_2S, wt %	0.79
Sodium, wt %	18.4
Inorganic carbon, wt %	1.14
Organic carbon, wt %	33.5
Sulfate, wt %	4.08

where (see Chen & Gao, 2003) $\rho_l K_\mathrm{a}/\rho_d k_d = 1.2 \times 10^{-6}\,\mathrm{m^2\,K/W\,s}$, $E_\mathrm{act}/E_\mathrm{o} = 0.95 + 10\,c^*/(t+30)$, $c^* = 0.8547 - 0.0147\,\mathrm{Z_{Na}} - 0.0095\,\mathrm{W_{Na}}$, $E_\mathrm{o} = 3431\,\mathrm{kJ/kmol}$, $\mathrm{Z_{Na}}$ is the effective sodium weight % on total black liquor solids, $\mathrm{W_{Na}}$ is the weight % of $Na_2CO_3 + Na_2SO_4$ on total black liquor solid. $\mathrm{Z_{Na}}$ and $\mathrm{W_{Na}}$ can be evaluated from values in table 6.1. $\triangle H_s^o$ is the enthalpy of crystallization which is approximated by the enthalpy of formation for Na_2CO_3 (see § 6.2.4).

6.2.4 Crystallization Parameters

Sodium carbonate and sodium sulfate form the double salt burkeite ($2Na_2SO_4 \cdot Na_2CO_3$) when they co-crystallize (Hedrick & Kent, 1992; Frederick Jr. *et al.*, 2004; Bayuadri, 2006). For high dry solids black liquor evaporation, Frederick Jr. *et al.* (2004) reports that in addition to burkeite, another double salt of Na_2CO_3 and Na_2SO_4 but rich in Na_2CO_3 is formed. Thus, to simplify the numerical implementation of the crystallization source terms, the primary crystallizing salt in the black liquor mixture in our formulation is assumed to be Na_2CO_3. Consequently, parameter values relevant to species transport and species depletion source terms (e.g.enthalpy of formation of the precipitated salt, mass diffusivity in species conservation law) were approximated using corresponding values for Na_2CO_3. Table 6.2 shows relevant property values of Na_2CO_3 used in black liquor numerical simulations.

Table 6.2: Physical properties of Na_2CO_3 relevant to species transport model (Derek & Robert, 1985; Abdullah & Baris, 2006)

Parameter	Value	Unit
Enthalpy of formation (@ 298 K)	-1.131×10^6	$\mathrm{J\,mol^{-1}}$
Molar mass (anhydrous)	0.106	$\mathrm{kg\,mol^{-1}}$
Density (anhydrous)	2540	$\mathrm{kg\,m^{-3}}$
Thermal conductivity	0.0418	$\mathrm{W\,m^{-1}\,K^{-1}}$
Specific heat	1042	$\mathrm{J\,kg^{-1}\,K^{-1}}$
Diffusion Coefficient (@ 298 K)	1.1×10^{-9}	$\mathrm{m^2\,s^{-1}}$

6.2.5 Black Liquor Transport Properties

Experimental correlations for the transport properties of black liquor relevant to evaporation are defined in terms of temperature and dry solids mass fraction (see Adams *et al.*, 1997):

$$\log_{10}\left(\frac{\mu_l}{\mu_w}\right) = \frac{\frac{\chi_s T^*}{T}}{0.679 - 0.656\,\frac{\chi_s T^*}{T}} \tag{6.14a}$$

$$\rho_l \;=\; 1007 - 0.495\,(T - 273.15) + 6\chi_s \tag{6.14b}$$

$$k_l = 1.44\,\mathrm{x}\,10^{-3}\,(T - 273.15) - 0.335\chi_s + 0.58 \tag{6.14c}$$

$$c_{p_l} = (1 - \chi_s)\,c_{p_w} + \chi_s\,c_{p_s} + c_{p_e} \tag{6.14d}$$

where μ_l [Pa-s], ρ_l [kgm^{-3}], k_l [W/mK], c_{p_l} [J/kgK] are respective black liquor dynamic viscosity, density, thermal conductivity and specific heat, $T^* = 373\,\mathrm{K}$, $\mu_w = (36.6\,T - 10090)^{-1}$, $c_{p_w} = 4216$ J/kg K, $c_{p_s} = 1684 + 4.47\,(T - 273.15)$, $c_{p_e} = (4930 - 29\,(T - 273.15))(1 - \chi_s){\chi_s}^{3.2}$ and T is temperature [K]. The mass diffusion coefficient for black liquor ξ_l is approximated based on the molecular diffusivity of $Na_2CO_3 = 1.1 \times 10^{-9}\,\mathrm{m^2 s^{-1}}$ and the surface tension coefficient is specified as $\sigma = 0.033\,\mathrm{N m^{-1}}$.

6.2.6 Boundary and Initial Conditions

Boundary conditions for velocity and fluid phase fraction for 2-D falling liquid films presented in § 2.1.5 are also valid for black liquor flat plate simulations. For simulations of falling film flow on a cylindrical surface at a given Reynolds number, the perturbed inlet velocity $\boldsymbol{v_o}$ and liquid film inlet thickness r_o are specified as:

$$r_o = r_{wall} + \delta_{_N} \tag{6.15a}$$

$$\boldsymbol{v}_o \;=\; 0\mathbf{i} + u_{_N}\,\mathbf{j} + \,\epsilon \sin(2\pi f t)[u_{_N}\,\mathbf{j} + \mathbf{k}] \tag{6.15b}$$

where $\mathbf{i}$, $\mathbf{j}$, $\mathbf{k}$ are the coordinate unit vectors, r_{wall} is outer radius of the cylindrical wall, f is the forcing frequency in Hz and $\epsilon = 0.05$ for this study. $\delta_{_N}$ and $u_{_N}$ are the corresponding Nusselt values (see § 1.4.2). The primary flow direction for the 3-D simulation is along the y axis and inlet velocity has y and z perturbation components.

On the heating wall, temperature is maintained at a uniform value greater than the sum of the saturation temperature and boiling point rise for the specified inlet dry solids mass fraction. All other variables on this wall have zero-flux conditions with no-slip condition for velocity. For the 3-D simulation, periodic conditions are imposed at the vertical sides of the cylinder since only a portion of the cross-sectional perimeter is simulated. To simplify the computation domain, a numerical wall boundary is imposed at $r = r_{wall} + 4\delta_{_N}$ where zero-flux condition is imposed on all variables except velocity which has no-slip conditions. The same conditions apply to the numerical wall boundary for the flat plate. At the outlet, outflow conditions are specified i.e. stress free conditions for velocity and homogenous face-normal gradients for temperature, species and phase volume fraction. For the 3-D simulation, the flow domain is initialized with a uniform dry solids mass fraction black liquor mixture of film thickness r_o and velocity field $(0, u_{_N}, 0)$.

Table 6.3: Flow and heating conditions for black liquor falling film evaporation simulations

$\chi_{s,in}$	T_{sat} [K]	T_{in} [K]	T_w [K]	Re	Γ [kg/m s]	f [Hz]
0.40	348.15	352.99	359.00	160	0.72	30
0.41	324.15	329.18	334.18	56	0.60	30
0.50	348.15	355.15	360.15	50	0.81	25
0.51	324.15	331.40	336.40	11	0.62	30

6.3 Numerical Validation

Validation results are presented for black liquor falling film evaporation heat transfer coefficient and average dry solids mass fraction at evaporator exit. The simulated results are compared with experimental results and correlations from falling film experiments by Johansson *et al.* (2009*b*).

6.3.1 Evaporation Heat Transfer Coefficient

Table 6.3 shows flow and heating conditions for the numerical simulation of 2-D wavy-laminar falling film evaporation of black liquor. Inlet temperature for black liquor and vapor from the evaporating liquid is set at the elevated temperature corresponding to the sum of the saturation temperature and inlet dry solids boiling point rise. The temperature difference between the inlet liquor and heating wall is set at 5 K. In general, the vapor within the evaporator is superheated since black liquor evaporation occurs at a temperature greater than the prescribed saturation temperature. The computation domain is uniformly discretized with step sizes set at $0.178\delta_{_N}$ and $0.0286\delta_{_N}$ in the streamwise and normal directions respectively. The streamwise length of the computation domain is set at $800\delta_{_N}$ which gives evaporator lengths in the range 0.75m - 1.45m depending on film thickness at the inlet.

For the evaporating black liquor film heated by a uniform temperature wall, the

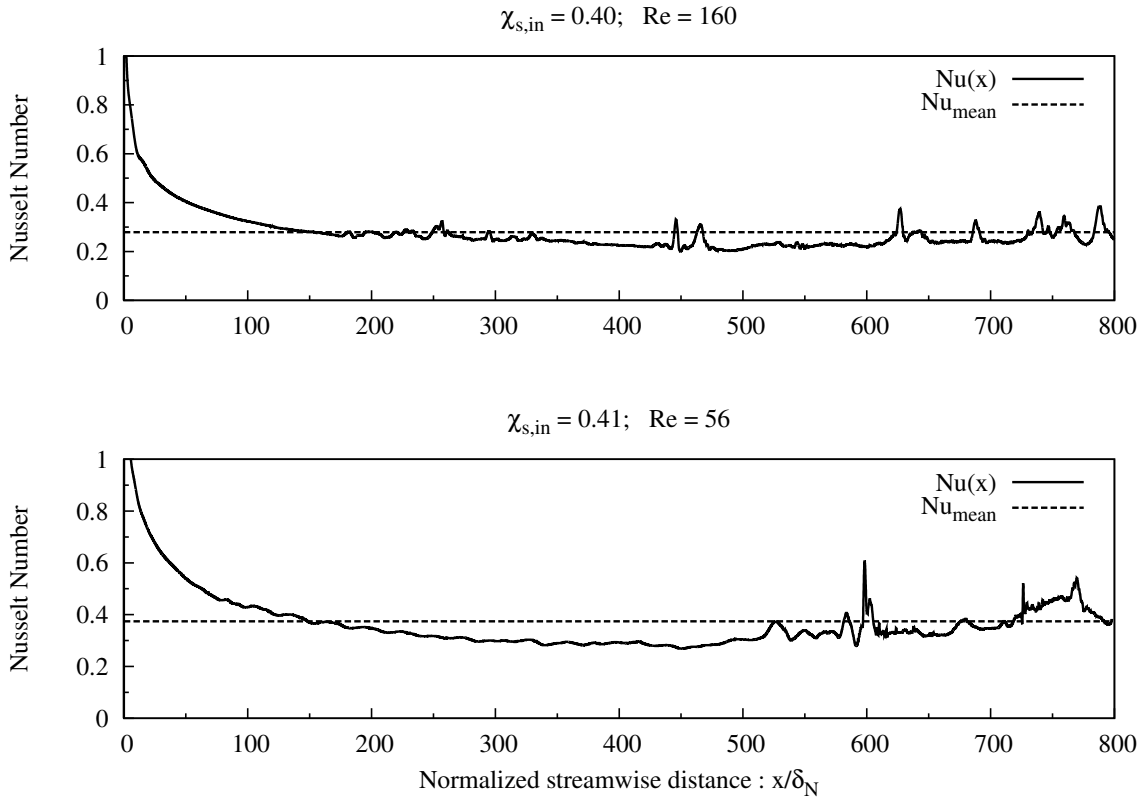

Figure 6.2: Streamwise variation of Nusselt number for simulated cases in table 6.3.

instantaneous evaporation heat transfer coefficient is defined as:

$$h(x,t) \;=\; \frac{-\kappa_l \frac{\partial T}{\partial y}\Big|_{y=0}}{T_w - T_{in}} \tag{6.16}$$

where T_w is the wall temperature and T_{in} is the film inlet temperature. The time averaged heat transfer coefficient $\bar{h}$ is evaluated using equation (5.8) by integrating over the evaporator length. The corresponding average Nusselt number $\bar{Nu}$ is evaluated using equation (5.9). The streamwise variation of the instantaneous Nusselt number is shown in figure 6.2. The effect of dry solids mass fraction on falling film evaporation heat transfer coefficient has been studied by Johansson *et al.* (2009*b*). From their experimental results they proposed the following correlation for predicting the average evaporation heat transfer coefficient for black liquor in the wavy laminar

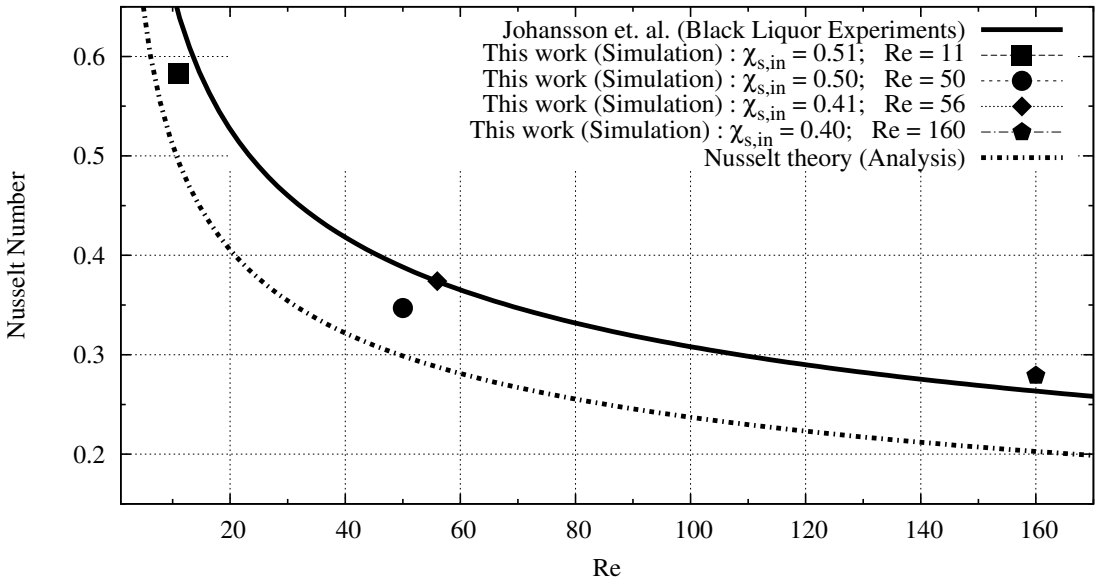

Figure 6.3: Simulated average Nusselt number for the cases in table 6.3 compared with predictions from Nusselt (1916) flat film theory and correlations from Johansson *et al.* (2009*b*).

flow regime:

$$\bar{Nu} = 1.43\, Re^{-1/3} \tag{6.17}$$

Figure 6.3 shows plots of the average Nusselt number from our simulated cases in table 6.3 and predictions using equation (6.17). The results show good agreement.

6.3.2 Exit Dry solids Mass Fraction

Figure 6.4 shows plots of the liquid film crosswise variation of dry solids mass fraction and the corresponding average value at the near exit region of the evaporator. Similar to the mean heat transfer coefficient, the mean dry solids mass fraction $\chi_{s,\text{mean}}$ over the film thickness is expressed as:

$$\chi_{s,\text{mean-exit}} = \frac{1}{\delta_{\text{exit}}} \int_0^{\delta_{\text{exit}}} \chi_{s,\text{exit}}\, dy \tag{6.18}$$

In their experimental study, Johansson *et al.* (2009*b*) determined the change in black liquor dry solids mass fraction between evaporator inlet and exit based on an overall energy balance and the mass flow of vapor produced from the evaporation process.

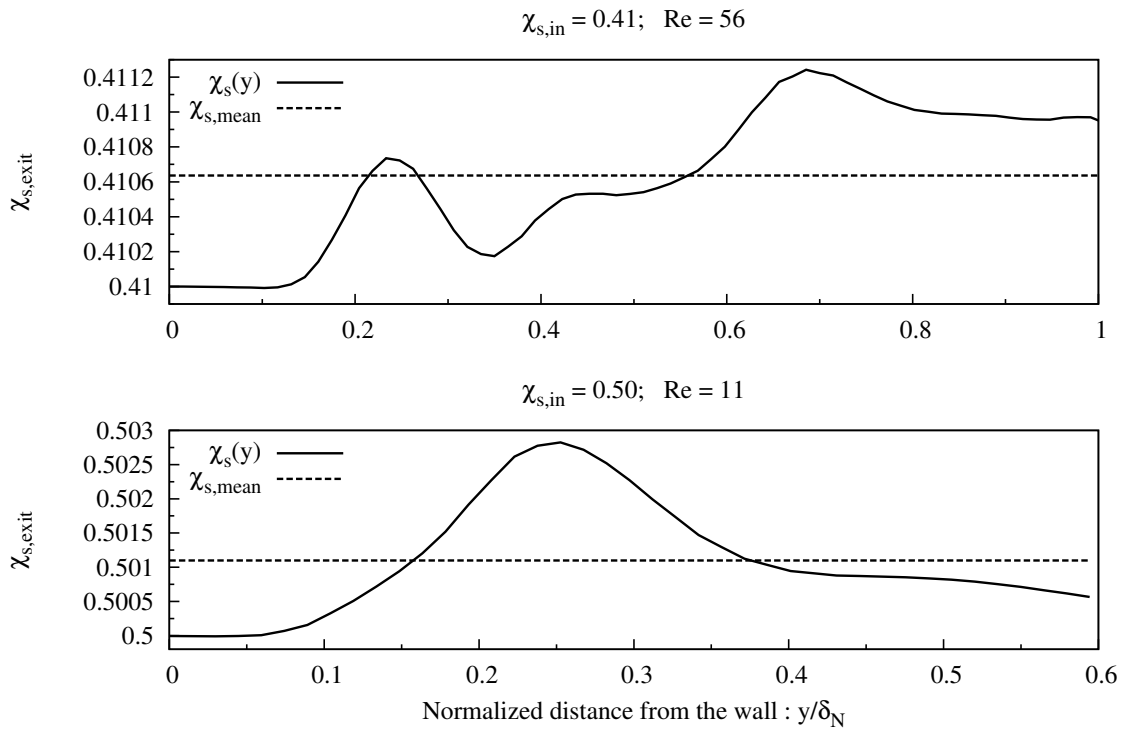

Figure 6.4: Crosswise profile of instantaneous dry solids mass fraction and the corresponding mean value over the film thickness at the evaporator exit.

Figure 6.5 shows plots of percentage change in mass fraction over the evaporator per unit length of evaporator from our simulations and the experimental measurements of Johansson *et al.* (2009*b*). The results provide confidence that the numerical implementation predicts with sufficient accuracy the net dry solids enrichment for an evaporating black liquor mixture.

6.4 Analysis of Simulation Results

6.4.1 Black Liquor Free Surface Waves

Simulations for non-evaporating black liquor falling films on flat plate and cylindrical wall were conducted to investigate the structure and evolution of black liquor free surface waves. The 2-D simulations investigate the influence of dry solids mass fraction and Reynolds number on falling film wave structure and formation of complex interfacial flow structures. The 3-D simulation focused on the evolution of 2-D

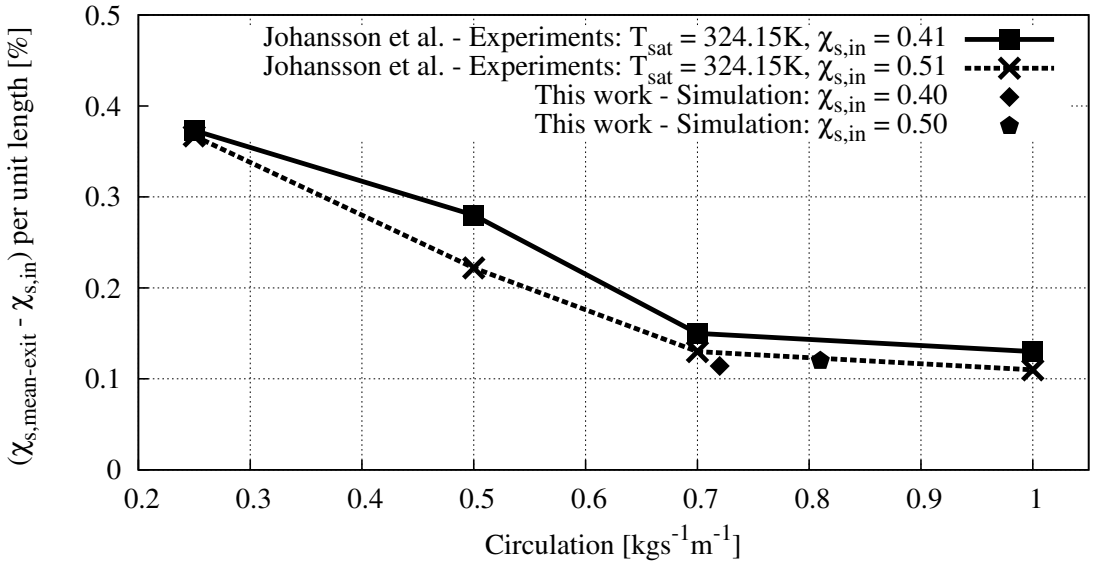

Figure 6.5: Percentage increase in average dry solids mass fraction per unit length of evaporator from numerical simulation compared with experimental results of Johansson *et al.* (2009*b*).

perturbations and analysis of the fundamental structure of the resulting 3-D waves.

6.4.1.1 Effect of Dry Solids

Figure 6.6 shows simulated free surface wave profiles for black liquor falling films at $Re = 80$, $T = 348.15\,\mathrm{K}$, $f = 30\,\mathrm{Hz}$ and dry solids mass fraction $\chi_s = 0.2$, 0.3 and 0.4. From the plots we observe that low dry solids saturated (i.e. fully developed regularly spaced large amplitude waves) black liquor free surface waves consist of solitary waves preceded by growing capillary waves (see top plot when $\chi_s = 0.20$). This is similar to wave structures on laminar water falling films perturbed by long wavelength disturbances. For such surface wave types, secondary instabilities typically evolve from wave regions dominated by capillary waves due to solitary-capillary wave interaction (Nosoko & Miyara, 2004). As the dry solids mass fraction increases, the large amplitude wave still retains its tear-drop shape but the preceding capillary waves no longer develop on the film (see bottom plot when $\chi_s = 0.40$).

This observation follows from the Weber number $We = \sigma/\rho_l u_N^2 \delta_N$ dependence on

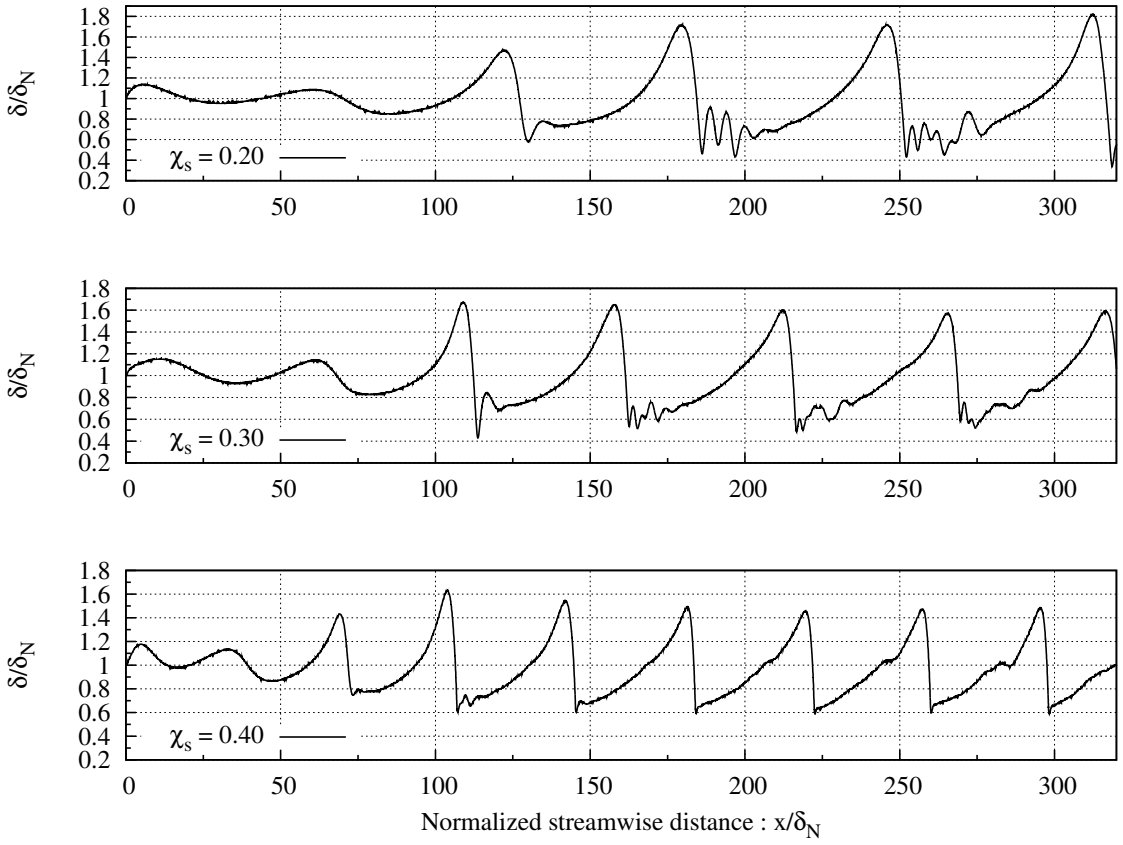

Figure 6.6: Surface wave profiles for simulated black liquor falling films at $Re = 80$, $T = 348.15\,\mathrm{K}$, $f = 30\,\mathrm{Hz}$ and different dry solids mass fraction.

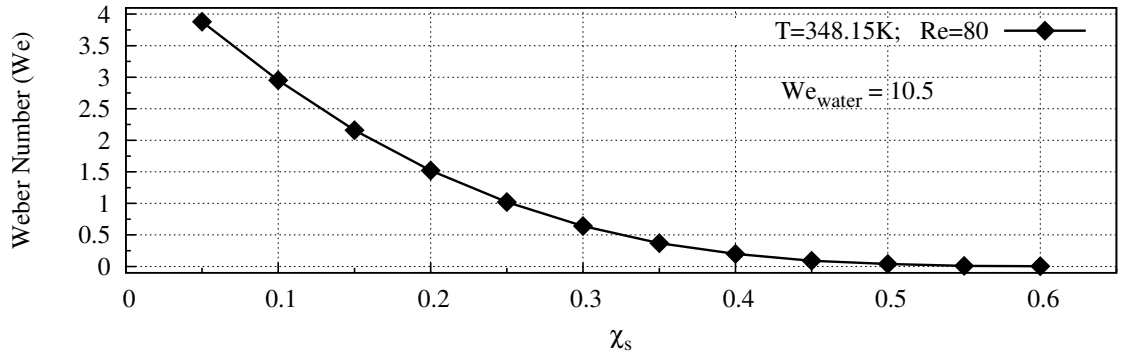

Figure 6.7: Weber number (We) dependence on black liquor dry solids mass fraction χ_s for falling film with $Re = 80$.

dry solids mass fraction. For black liquor (with constant surface tension coefficient) falling films at fixed Reynolds number, an increase in dry solids mass fraction means

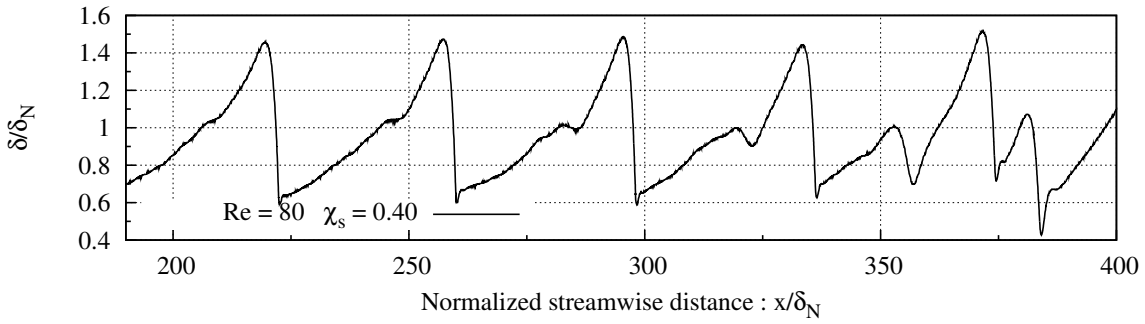

Figure 6.8: Interface profile showing evolution of secondary instability on black liquor falling film free surface - $\chi_s = 0.4$, $Re = 80$.

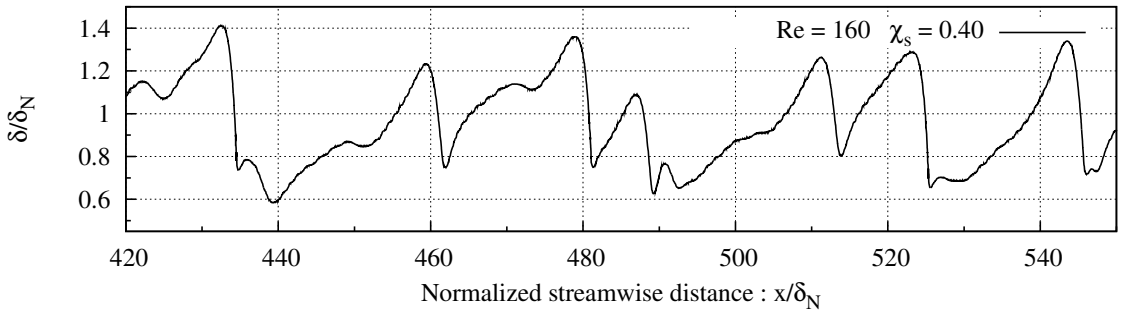

Figure 6.9: Interface profile showing developed free surface waves from secondary instabilities on black liquor falling film - $\chi_s = 0.4$, $Re = 160$.

a decrease in the influence of surface tension relative to inertia on interfacial wave structure (see figure 6.7). Consequently, the liquid film is more likely to spread out leading to a flat interfacial surface as opposed to forming curvatures that support capillary wave structures. The decreasing Weber number also impacts the magnitude of the streamwise pressure gradient in the liquid film. Dietze *et al.* (2008) showed that for constant properties liquid, the streamwise derivative of liquid film pressure is given by:

$$\frac{\partial p}{\partial x} = -\frac{\varepsilon We}{3^{1/3}} \frac{\partial \kappa^*}{\partial x}, \qquad \kappa^* = \frac{\varepsilon(\partial^2\delta/\partial x^2)}{[1+\varepsilon^2(\partial\delta/\partial x)^2]^{3/2}} \tag{6.19}$$

where $\varepsilon = \delta_{_N}/L_e$ and κ^* is the non-dimensional interface curvature. Adverse streamwise pressure gradients at the wavefront of large amplitude waves have been shown to induce flow separation (see § 4.4.2 for discussion on backflow dynamics) in laminar

falling films (Dietze *et al.*, 2008, 2009). From equation (6.19) and figure 6.7, we can conclude that black liquor films with high dry solids mass fraction are less likely to form backflow regions. In particular, results from our simulations show that backflow is not observed when $We < 1$ i.e. for $\chi_s \geq 0.3$ at $Re = 80$.

6.4.1.2 Secondary Instability and Wave-Breaking

For high dry solids black liquor falling films, the absence of capillary waves suggest that secondary instabilities are less likely to evolve at the immediate wavefronts of large amplitude waves. Figure 6.8 shows the onset of a growing secondary instability for $\chi_s = 0.40$, $Re = 80$ black liquor falling film. The secondary instability is seen to evolve from the liquid slope behind the saturated large amplitude wave. In general, the effect of secondary instabilities increase with Reynolds number. Figure 6.9 shows developed secondary instabilities for $\chi_s = 0.40$, $Re = 160$ black liquor film with secondary wave sizes and amplitudes comparable to those of saturated large amplitude primary waves. The large amplitude primary wave tends to travel faster than the secondary wave due to its larger aggregate body force which makes it relatively easier to overcome viscous drag. This characteristic becomes more evident as the dry solids mass fraction of the falling film increases. The result is that the faster traveling saturated wave eventually merges with the secondary wave in front of it (as shown in figure 6.10) giving rise to a larger but stable wave. This new wave also goes through a similar cycle i.e. it accelerates due to increased body force and merges with a preceding saturated wave. The wave resulting from the second merger is much larger and consequently unstable.

Figure 6.11 shows the large wave flow sequence post-second merger. The fluid particles at the wave apex experience much less viscous drag since the streamwise velocity field in the apex region of the large wave is approximately uniform with respect to the crosswise direction. As a result, the apex region travels faster under

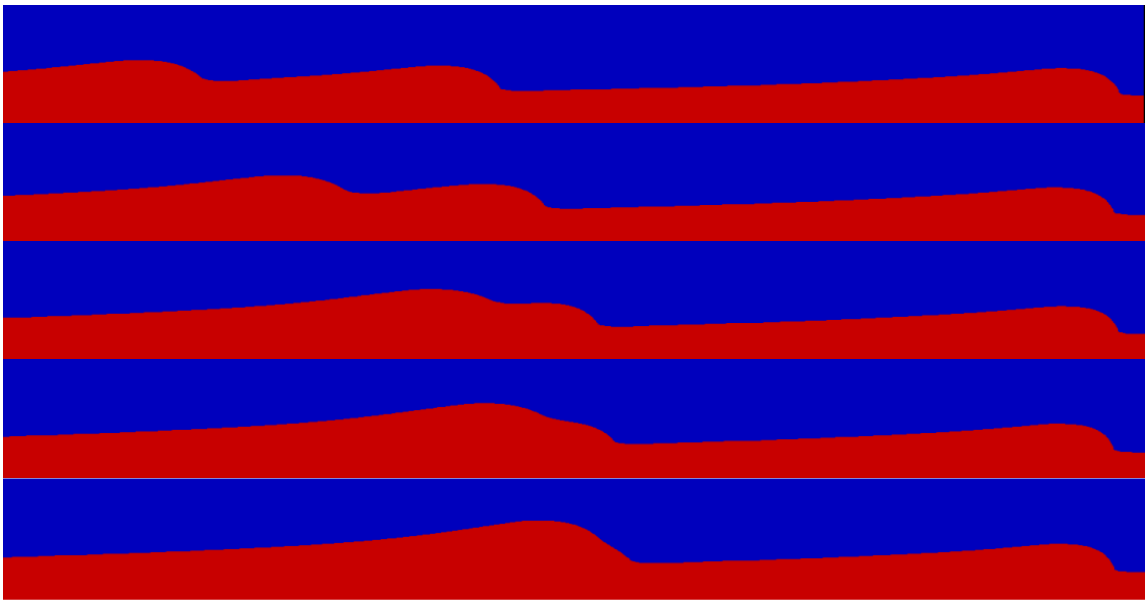

Figure 6.10: Film free surface waves ($\chi_s = 0.50$, $Re = 120$, $T = 348.15\,\mathrm{K}$, $f = 30\,\mathrm{Hz}$) showing flow sequence of a saturated large amplitude wave (left end) merging with a secondary wave (middle). The red portion represent the liquid film while blue defines vapor, and flow is from left to right

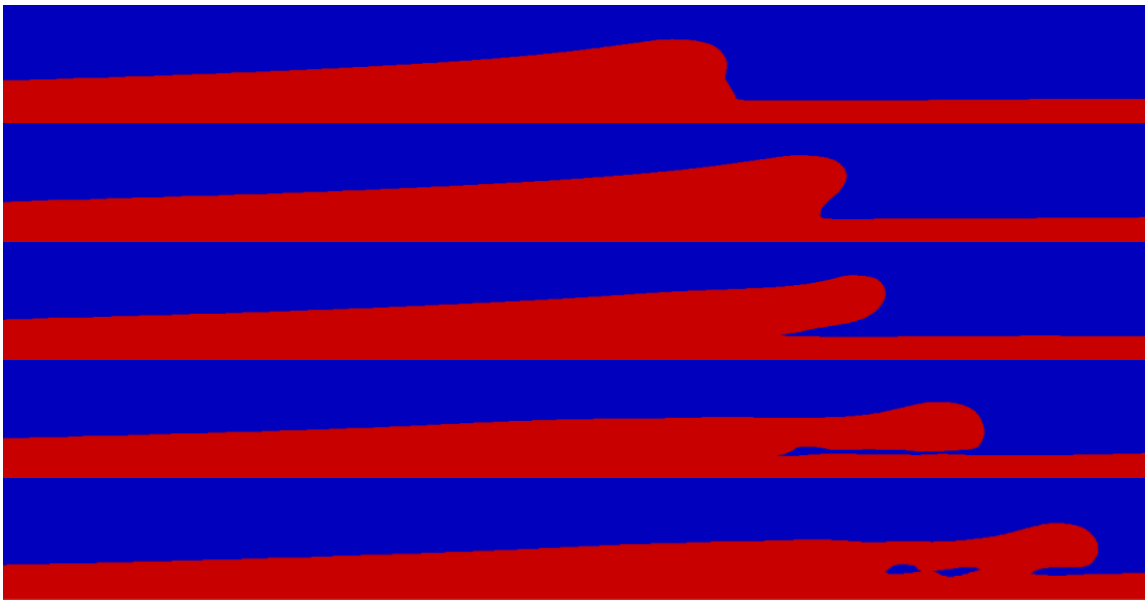

Figure 6.11: Film free surface waves ($\chi_s = 0.50$, $Re = 120$, $T = 348.15\,\mathrm{K}$, $f = 30\,\mathrm{Hz}$) showing flow sequence of large wave after second waves merger. The resulting large wave is unstable as it deforms to form a secondary film.

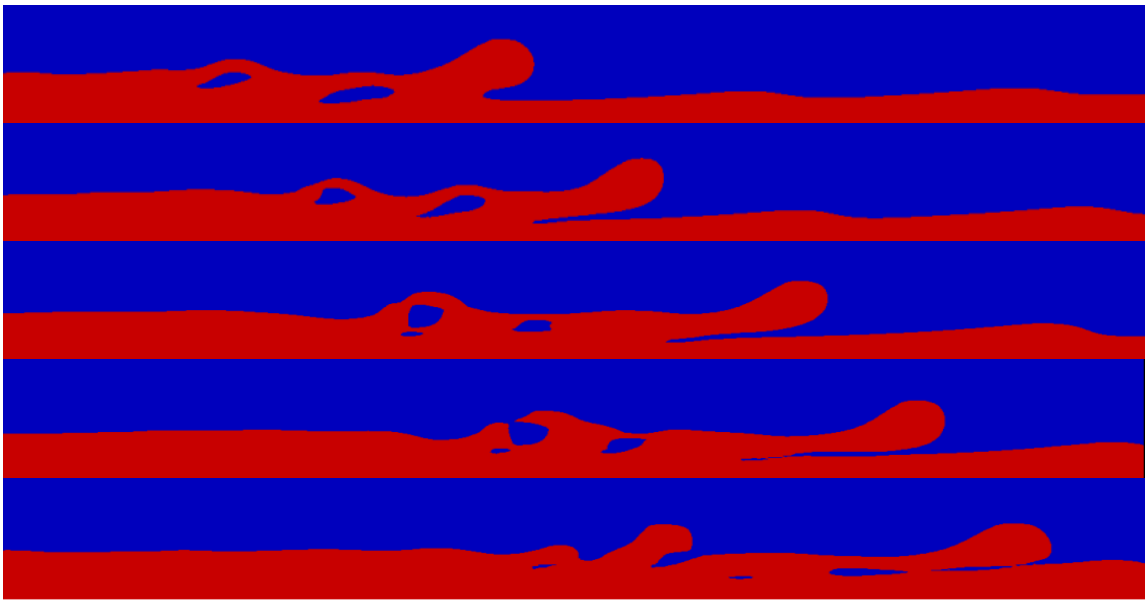

Figure 6.12: Film free surface waves ($\chi_s = 0.50$, $Re = 120$, $T = 348.15\,\mathrm{K}$, $f = 30\,\mathrm{Hz}$) showing bubble migration and subsequent escape from liquid film leading to significant interfacial distortion and secondary wave-breaking.

gravitational body force relative to the wavefront. This relative motion deforms the wave in a manner that gives rise to a secondary film adjacent to the substrate film. The secondary film eventually collapses on the substrate film, trapping a column of vapor underneath (see bottom plots of figure 6.11) thus entraining vapor in the liquid film. The entrained vapor bubbles tend to migrate towards the interface before escaping from the liquid film (see figure 6.12), leaving behind a distorted interfacial region. The combined action of wave breaking and vapor entrainment fundamentally alters the structure of the liquid film (compare figures 6.10 and 6.12) and the process appears to be self sustaining. Johansson (2008) reported similar observations from falling film experiments of evaporating black liquor suggesting that liquid film vapor entrainment and bubble formation is primarily due to surface wave interaction which eventually leads to multiple wave breaking.

6.4.1.3 Evolution of 2-D Perturbation

Figure 6.13 shows black liquor falling film ($\chi_s = 0.50$, $Re = 120$, $T = 348.15\,\mathrm{K}$, $f = 25\,\mathrm{Hz}$) free surface waves on a cylindrical wall. The respective outer diameter and length of the cylinder are 60 mm and 1.28 m. The simulated perimeter is $\frac{1}{8}$ th of actual cylinder perimeter. The uniform grid sizes along the coordinates are $\triangle x = 0.000153\,\mathrm{m}$, $\triangle y = 0.000512\,\mathrm{m}$ and $\triangle z = 0.000589\,\mathrm{m}$ with the streamwise direction set along y. In the figure the complete cylinder is shown as smaller cylinder segments for purposes of illustration. The flow starts from the top of the first cylinder (left end), exits at the bottom and continues at the top of the second cylinder and so on until the last cylinder (right end). Flow is from top to bottom on all cylinders. The flow disturbance is introduced as a monochromatic perturbation of inlet velocity components along y and z directions as specified in equation (6.15b).

Figure 6.13 shows the evolution of an initial 2-D perturbation into a 3-D wave for black liquor falling film. The perturbation goes through a number of wave transformations before complete loss of regularity. Close to the inlet, the wave is predominantly 2-D but gradually evolves into an inverted "*U-shaped*" wave. Wave-breaking can be observed at the vertical ends of the inverted "*U-shaped*" wave (see first cylinder) as the film height grows to an unstable maximum at these points. In this region, the separation between consecutive waves remains regular. Further downstream, the second transformation is initialized as the midpoint of the horizontal section of the inverted "*U-shaped*" wave grows both in amplitude and speed. The downward acceleration of the midpoint (see second cylinder) changes the wave structure into an "*M-shaped*" wave. Wave breaking is also observed at the accelerating midpoint as the amplitude at this point grows to an unstable maximum. Comparing the wave separation on the first two cylinders, we observe that the second transformation slightly affects the regularity of the wave separation. Beyond the second transformation, secondary instabilities start evolving between consecutive large waves (see third cylinder). The

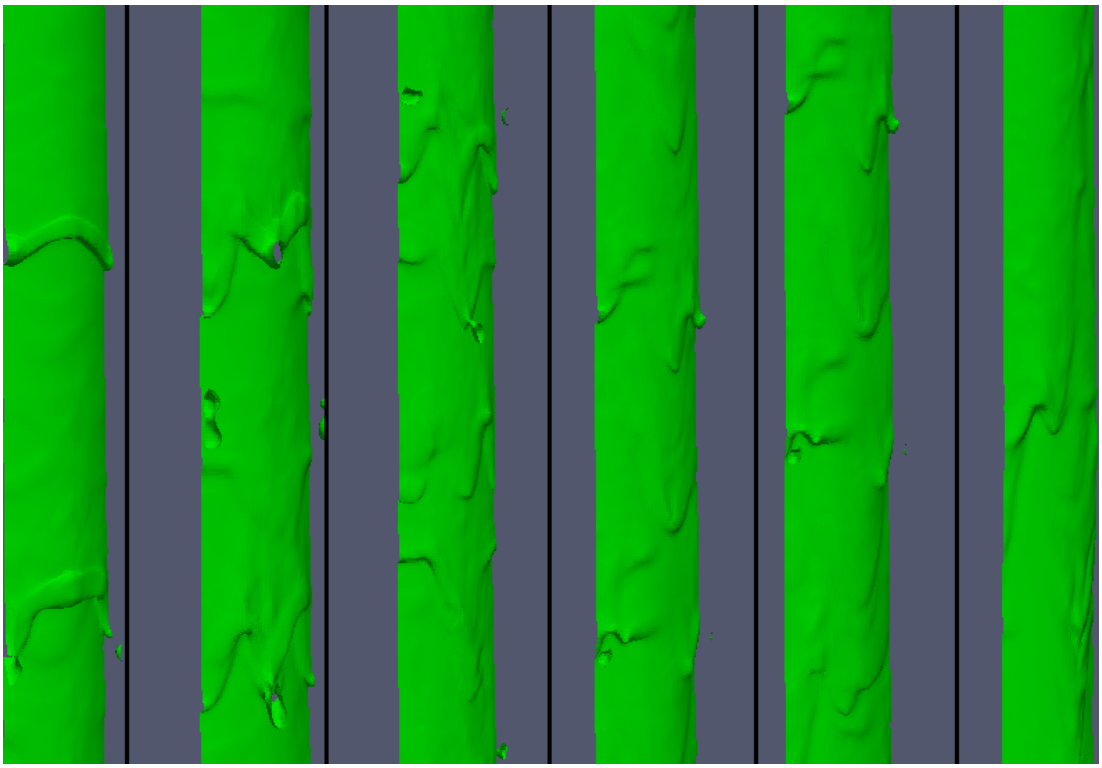

Figure 6.13: Simulated black liquor falling film ($\chi_s = 0.50$, $Re = 120$, $T = 348.15\,\mathrm{K}$, $f = 25\,\mathrm{Hz}$) free surface waves on cylindrical wall. The full cylinder is shown as segments. Flow comes in at the top of the outer left cylinder and exits at the bottom of the outer right cylinder.

secondary disturbances in turn interact with the fast traveling portions of the primary 3-D waves leading to loss of regularity in wave separation.

Figure 6.14 shows free surface waves on an experimental non-evaporating black liquor falling film on a cylinder of same diameter as the simulated domain in figure 6.13, and length of 4.5 m. The dry solids fraction for the experimental liquor is $\chi_s = 0.41$ at temperature $T = 298.15\,\mathrm{K}$ with mass flow $0.19\,\mathrm{kgs}^{-1}$ ($We = 0.085$). The mass flow of the simulated film is $0.37\,\mathrm{kgs}^{-1}$ ($We = 0.018$). Both films are in the laminar flow regime where inertia dominate surface tension effects (based on their Weber numbers) thus allowing for a qualitative comparison of flow structures. Figure 6.14 is taken from a height of 0.67 m from the inlet which corresponds to the upper section of the third cylinder in figure 6.13. The plots show that the simulated result correctly

Figure 6.14: Experimental black liquor ($\chi_s = 0.41$, $T = 298.15\,\mathrm{K}$) falling film free surface waves.

reproduces the qualitative 3-D structure of the experimental wave with respect to circumferential variation primary instability and evolution of secondary instabilities.

6.4.2 Wave Induced Transport in Evaporating Film

6.4.2.1 Influence on Temperature and Species

With evaporation and consequently species enrichment limited to the interfacial region only, a species boundary layer in the interfacial region soon develops in the evaporating liquid film. The functional dependence of black liquor transport properties on species concentration and temperature implies stronger coupling and increased nonlinearity of the transport equations. The combined effect of increased nonlinearity and highly irregular interfacial wave structures give rise to more complex crosswise concentration profiles in evaporating black liquor falling films (e.g. see figure 6.4) in comparison to the regular boundary layer profile.

Falling liquid films interfacial deformation impose streamwise pressure variations that induce velocity gradients in the liquid film (Dietze *et al.*, 2008, 2009). For black liquor, the impact of crosswise convective transport to and from the evaporator surface is of significance to species enrichment i.e. evaporation and more importantly

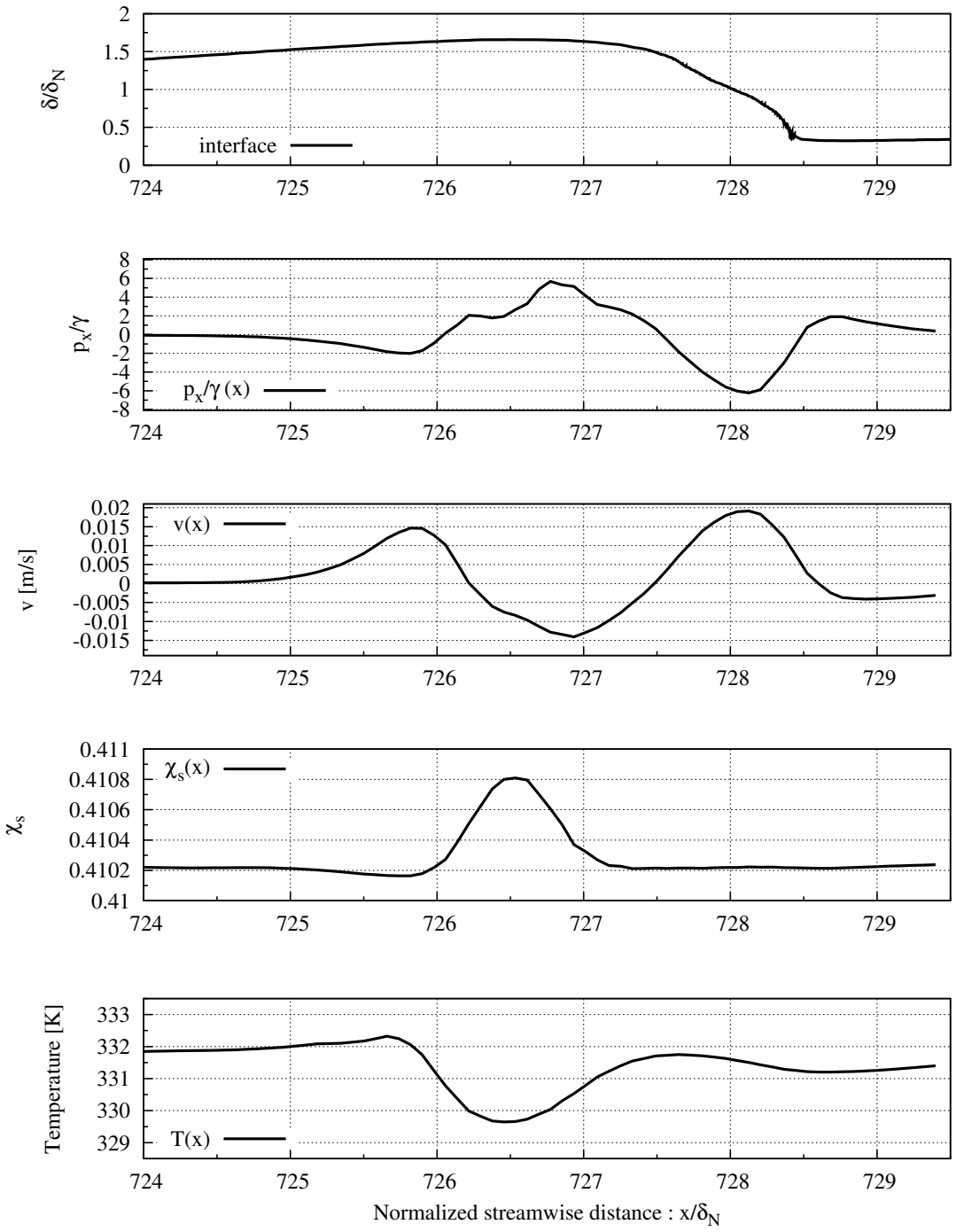

Figure 6.15: Normalized film thickness $\delta/\delta_{_N}$, normalized liquid film streamwise pressure gradient $p_x(=\frac{\partial p}{\partial x})/\gamma$, liquid film crosswise velocity v, dry solids mass fraction χ_s and temperature T across a large amplitude wavefront for an evaporating black liquor ($\chi_{s,in} = 0.41$, $Re = 56$) 2-D falling film. Variables were sampled at a distance $y = 0.220\,\text{mm} = 0.2\delta_{_N}$ from the wall.

soluble scaling. High thermal energy liquid elements transported by convection from the wall into the liquid film enhance evaporation heat transfer. On the other hand, species-enriched liquid elements transported from the phase boundary to the higher temperature evaporator wall region could induce soluble scale fouling as a result of the inverse solubility property (Chen & Gao, 2003) of dissolved black liquor salts.

High dry solids black liquor falling films at moderately high Reynolds numbers are characterized by low Weber numbers and consequently low streamwise pressure gradients (see equation (6.19)). However for regions along the interface where the curvature gradient is significant e.g. wavefronts of large amplitude waves, sufficiently high streamwise pressure gradients could still develop, thus creating velocity gradients that drive crosswise convective transport. Figure 6.15 shows plots of normalized streamwise pressure gradient, crosswise velocity, dry solids mass fraction and temperature across a large amplitude wavefront for an evaporating black liquor ($\chi_{s,in} = 0.41$, $Re = 56$) 2-D falling film.

Across the wavefront, a streamwise pressure gradient develops in the liquid film. From the plots we observe that as pressure grows in the streamwise direction the crosswise velocity decreases in the same direction, and vice versa. The result of this streamwise variation of crosswise velocity can be observed from the streamwise distribution of dry solids mass fraction and temperature in the liquid film across the large amplitude wavefront. In the region where v is negative, fluid particles from the interface (i.e. high dry solids and low thermal energy) are transported towards the wall. The overall effect in the near wall region is that local temperature drops while local dry solids mass fraction increases as shown in the two bottom plots on figure 6.15. Away from the wavefront, the curvature variation is negligible and the crosswise velocity approaches zero. The result is that temperature and dry solids mass fraction return to uniform near wall values.

6.4.2.2 Implications for Crystallization and Scaling

In the absence of large amplitude waves, crystallization rates in the liquid film is highest at the phase boundary due to elevated species concentrations resulting from interfacial evaporation. This can be seen from the boundary-layer type crystallization rate profile in the thin liquid film downstream of the large amplitude wavefront shown in the bottom plot of figure 6.17(b). The normal velocity profile (see top plot of figure 6.17(b)) at this position indicates that crosswise convective flux is small but predominantly towards the high temperature wall. Thus the rate of soluble scaling or transport and deposition of molecules of salt precipitates from the phase boundary on evaporator surface is limited by resistance to mass diffusion i.e. the precipitated salt concentration difference (between the interface and the wall) and the film thickness over which diffusion occurs.

Figure 6.16: Black liquor film free surface waves ($\chi_{s,in} = 0.50$, $Re = 50$) showing large amplitude waves traveling downstream over a preceding flat thin liquid film.

With the formation of large amplitude waves traveling over sections of thin flat liquid film, the following inferences can be made:

1. Species enrichment due to liquid vaporization at the phase boundary of the large wave is limited by high liquid film resistance to conduction heat transfer. Consequently, lower crystallization rates can be observed at the large wave interface compared to the interface of the preceding flat thin film (see bottom plots of figure 6.17).

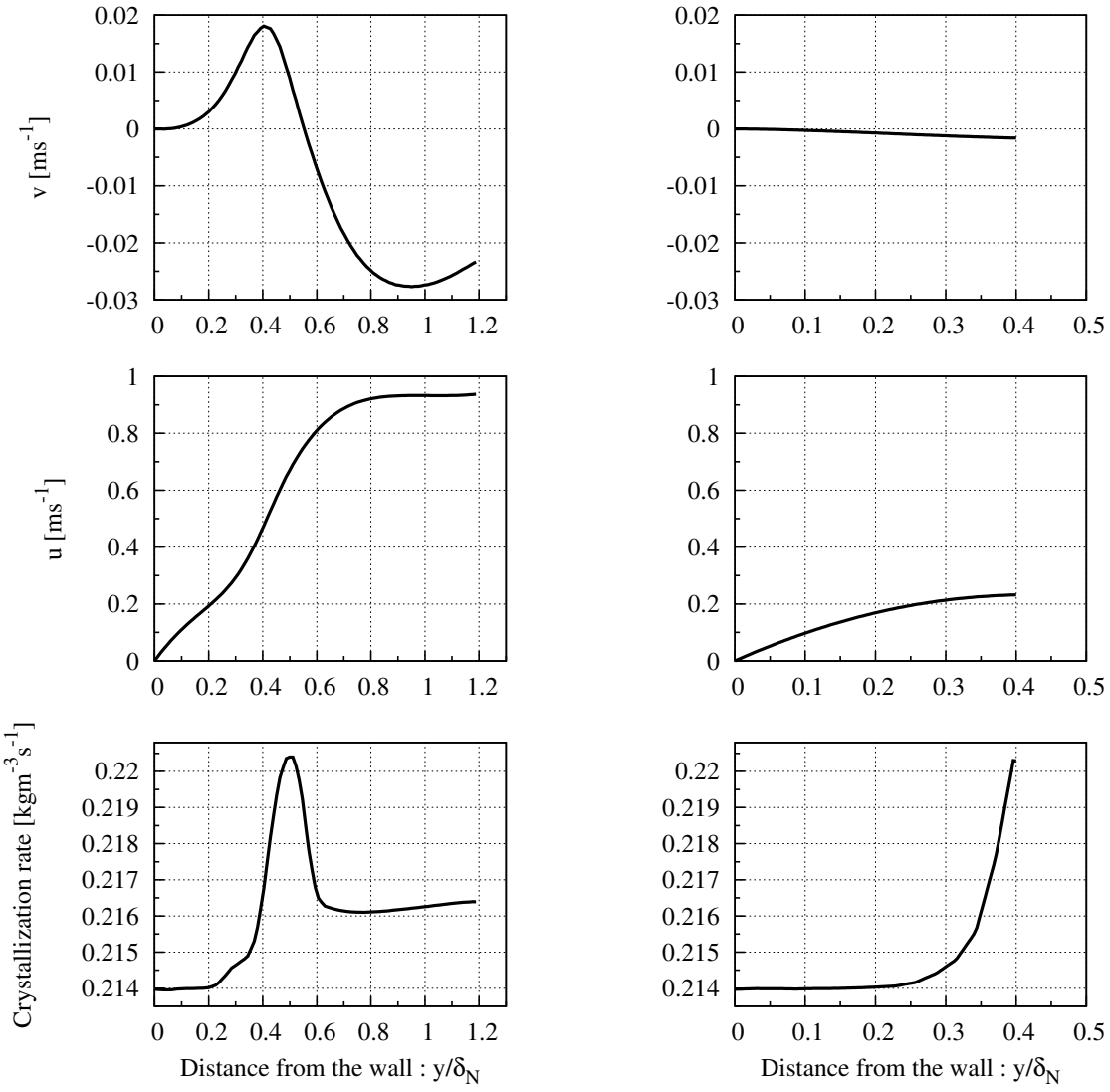

(a) Upstream of wavefront : $x/\delta_{_N} = 588.4$

(b) Downstream of wavefront : $x/\delta_{_N} = 590$

Figure 6.17: Crosswise distribution of crystallization rate $\dot{S}_{m,c}$, streamwise u and normal v velocity profiles at streamiwse positions upstream/downstream of the large amplitude wavefront shown in figure 6.16. See figure 6.18 for waves height and streamwise coordinates of sampled positions.

2. When large waves travel over thin film sections undergoing interfacial evaporation, the core of the large wave becomes enriched with liquid elements at higher species concentration from the interfacial region of the preceding thin film. From the middle plots of figure 6.17 we observe that the large wave interfacial region

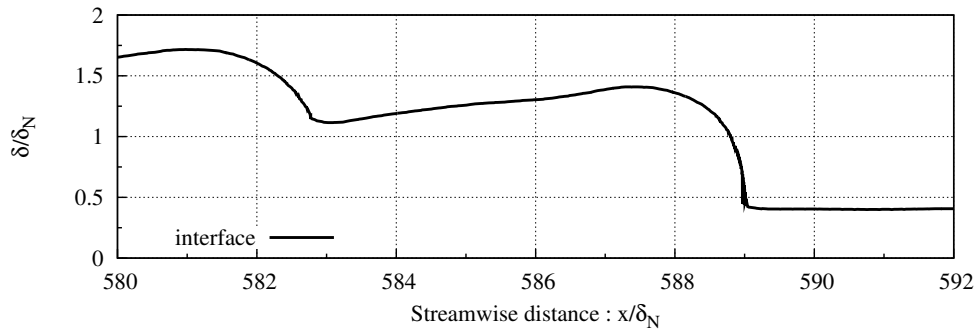

Figure 6.18: Interface profile showing amplitude and streamwise positions of free surface waves in figure 6.16.

travels in the streamwise direction at a uniform speed approximately four times the streamwise velocity of the thin film interface.

3. There is significant increase in magnitude and crosswise gradient of the normal velocity upstream of the large amplitude wavefront as shown in the top plot of figure 6.17(a). The normal velocity profile defines two crosswise flow regions based on the sign of v i.e. $v > 0$ or v^+ represents the near-wall region dominated by transport away from the wall towards the wave core while $v < 0$ or v^- describes the region dominated by transport from the interface towards the wave core. Neglecting the zero normal viscous stress boundary condition at the wall, the plot shows that the crosswise gradient of the normal velocity i.e. $\frac{\partial v}{\partial y}$, has a unique stationary point in each flow region. The v^+ region has a unique maximum while v^- region has a unique minimum. The preceding analysis implies that there is a stable point in the core of the large wave where fluid elements remain almost stationary with respect to the normal direction.

The implication of the second inference is that high species concentration can be observed in the core of the large amplitude wave though species enrichment i.e. evaporation does not explicitly occur in that region. This is consistent with results from the bottom plot of figure 6.17(a) which shows that the region of peak crystallization rate

(or χ_s) in the large wave corresponds approximately with the height of the thin film (see figure 6.18) downstream of the large amplitude wave. In addition, the region of peak crystallization also corresponds to points where fluid elements in the large wave are near-stationary with respect to the normal direction. In other words, high species concentration fluid elements from the interfacial region of preceding thin film that end up in the core of the large wave tend to remain within the wave core as the wave continues downstream. Finally, the velocity profile (see top plot of figure 6.17(a)) clearly shows a relatively high flux of species rich fluid elements transported from the interfacial region of the large amplitude wave towards the wave core. All three inferences combine to explain the high rate of crystallization in the core of the large amplitude wave compared to its phase boundary. This fundamentally distinguishes the crystallization process in the large wave compared with the flat thin film.

In the near wall region of the large amplitude wave, the velocity profile indicates that high temperature liquid elements from the wall are transported to the core of the large wave. This process enhances mixing and as such exposes the wave core to elevated temperatures. The resulting combination of high crystallization rates and temperature increases the potential for soluble scale precipitation due to the inverse solubility property of black liquor salts. Unlike the thin film downstream of the wavefront, the relatively high crosswise convective flux in the near wall region of the large amplitude wave ensures that precipitated salt molecules are not easily transported to evaporator wall. Consequently the potential for soluble scale fouling in the large wave is somewhat diminished.

6.4.2.3 Accumulative Effect of Waveforms

To investigate the accumulative effect of free surface wave variation with respect to fouling, we analyze the change in maximum crystallization rate at a fixed point in the liquid film with time (see plots in figure 6.19). This is motivated by the fact that

the crystallization rate is a measure of soluble salts available for evaporator surface fouling. The variables plotted in figure 6.19 were sampled over a time frame coinciding with the period of a large amplitude wave in the flow region where surface waves are fully developed.

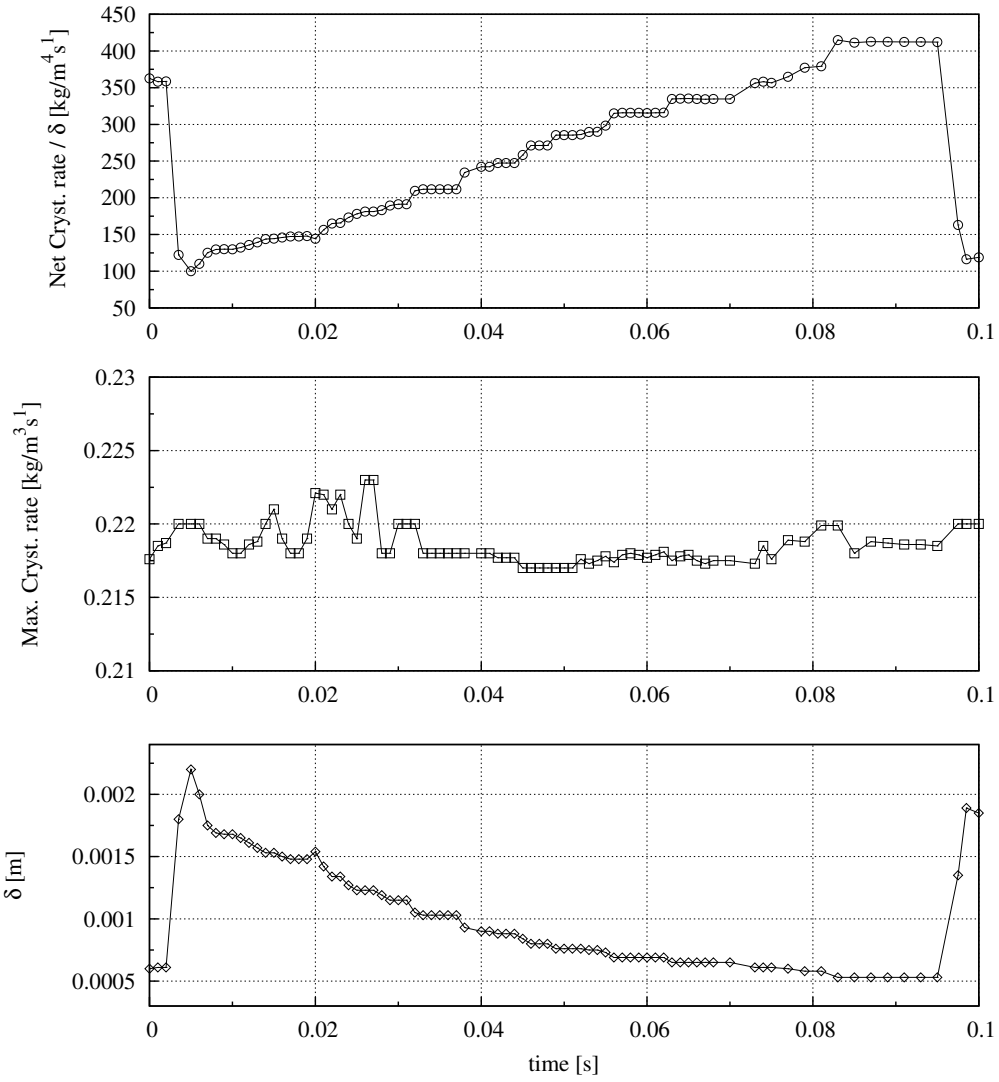

Figure 6.19: Time series of film amplitude and crystallization rates for evaporating black liquor ($\chi_{s,in} = 0.50$, $Re = 50$) at a fixed point in the liquid film. The values were sampled at a streamwise distance $x/\delta_{_N} = 586$.

The results show that the maximum rate of crystallization in the evaporating liquid film does not vary significantly with time even with relatively large changes in

film amplitude at the specified point (see bottom and middle plots of figure 6.19). From the analysis in § 6.4.2.2, we established that at different sections within the liquid film, convective fluxes do not play a significant role with respect to enhancement of fouling potential. Thus it suffices to analyze the diffusive transport of soluble salt in order to evaluate the variation of fouling potential with time (or accumulative effect) at a fixed point. For simplicity, we define the fouling potential due to diffusive flux across the liquid film at a fixed point as follows:

$$\text{diffusive fouling potential} \approx \frac{\dot{S}_{m,c}^{\max} - \dot{S}_{m,c}^{\text{wall}}}{\delta} \tag{6.20}$$

where $\dot{S}_{m,c}^{\max}$ is the maximum crystallization rate in the crosswise direction at a fixed streamwise position and $\dot{S}_{m,c}^{\text{wall}}$ is the corresponding rate at the wall. In a strict sense, the denominator of the right hand side of (6.20) should be evaluated as the normal distance from the wall to the point where the crystallization rate equals $\dot{S}_{m,c}^{\max}$. However we retain the above definition to simplify the analysis. The top plot of figure 6.19 shows the diffusive fouling potential variation with time at a fixed point in the liquid film. The net crystallization rate in the plot is defined as $\dot{S}_{m,c}^{\max} - \dot{S}_{m,c}^{\text{wall}}$.

The plot shows that over a large amplitude wave period, the diffusive fouling potential grows from a minimum value corresponding to the large amplitude wavefront to a maximum value at the tail end of the wave. This process continues as a cycle in time as waves travel over the fixed streamiwse position. For large amplitude waves separated by long stretches of thin film sections, extended periods of high fouling rates would result in rapid build up of soluble scale on heat transfer surface. As the dry solids mass fraction of the black liquor mixture increases, the large amplitude waves become bigger (implying much longer thin film sections) and more irregular which partly explains the rapid and erratic fouling behavior observed during evaporation of high dry solids black liquor mixtures.

CHAPTER 7

CONCLUSIONS AND FUTURE RECOMMENDATIONS

7.1 Conclusions

In the following sections we outline the key findings reported in this research study for the different falling film flow and transport phenomena investigated.

7.1.1 Backflow Dynamics

For low Reynolds number constant property falling liquid films with high Kapitza numbers such as water, capillary separation vortices or backflow regions also evolve at the wavefront of sinusoidal waves. This phenomenon has only been previously reported for films with solitary-capillary waves. Based on analysis of the streamwise pressure gradient at the wavefront of traveling interfacial waves, we show that the fundamental film hydrodynamics leading to flow separation and backflow are the same for both sinusoidal and solitary waves. We characterized the primary differences in backflow regions for both wave regimes in terms of the intensity of crosswise transport and the size of the resulting open vortex at wave saturation. Higher crosswise convective fluxes at the backflow regions of solitary waves result in more enhanced film transport compared to sinusoidal waves. A theory based on post-saturation dynamics of the streamwise pressure gradient and conservation of surface deformation energy is proposed to explain the interfacial wave interaction that give rise to capillary waves in front of saturated solitary waves. A consequence of this interaction is the formation of multiple backflow regions across the solitary-capillary wave train. The energy exchange between the waves also explains the evolution of the post-saturation backflow region as it is transformed from closed circulation to an open vortex and vice versa.

7.1.2 Thermal Analysis of Falling Film Evaporation

Simulations of falling liquid film evaporation at moderately high Reynolds numbers and large wavelength perturbation show that in addition to the well known solitary-capillary wave form that develop at the film interface, an intermediate wave with amplitude and wavelength less than the solitary wave's but greater than the capillary wave's also forms on the film interface well after the solitary waves have grown to saturation. The intermediate waves evolve due to interaction of capillary waves and are formed in front of the capillary waves preceding a saturated solitary wave. With respect to heat transfer, the growth of the intermediate waves give rise to significant film thinning at the intermediate wavefront resulting in relatively higher crosswise velocities and evaporation rates. This is the primary means by which heat transfer is enhanced in the falling film. For the case of constant wall heat flux, we identified three distinct thermal regions in terms of the streamwise variation of the wall temperature: (1) developing thermal region (growing thermal boundary layer), (2) region of near-uniform wall temperature and (3) region of fluctuating wall temperature with the later two regions largely influenced by evolution of film thickness. The heat transfer is highest in the region of fluctuating temperature where in addition to solitary and capillary waves, the flow also consists of developed intermediate waves.

7.1.3 Falling Film Evaporation of Black Liquor

With respect to film hydrodynamics our simulation results show that high dry solids mass fraction in the black liquor mixture damps out capillary waves on the film free surface. As a result, secondary instabilities evolve in regions where they easily grow into sizes comparable to large amplitude primary waves. The interaction between fully developed secondary and saturated primary waves give rise to unstable wave deformations which in turn leads to wave breaking and air entrainment. Results from 3-D black liquor simulations show that the initial 2-D perturbations of inlet

velocity evolve through distinct stages leading to 3-D free surface waves. The loss of 3-D wave regularity is attributed to interaction between relatively faster traveling portions of saturated 3-D waves and newly formed secondary instabilities. For the evaporating black liquor film, wave induced transport ensures that liquid elements with high species mass fraction are transported from the interfacial region to the core of large amplitude waves. As a result, similar crystallization rates can be observed at the interfacial region of thin films as well as the core of large amplitude waves even though the former has a lower species enrichment rate. The normal velocity profile at the large amplitude wave and thin flat sections of the liquid film shows that soluble scaling is a mass diffusion controlled process with a higher fouling potential at the thin film surface due to lower mass transfer resistance.

7.2 Future Recommendations

7.2.1 Non-Newtonian Black Liquor Rheology

At dry solids mass fraction greater than 0.5, black liquor rheology is characterized by non-Newtonian deformation. To implement more accurate solvers for simulating black liquor falling films at high dry solids mass fraction, a more accurate model for predicting black rheology is required. In addition to temperature and dry solids mass fraction, the model would also account for the influence of shear stress / strain-rate in predicting black liquor viscosity.

7.2.2 Crystallization Model

One of the primary objectives of this research is to develop a computational framework for studying more complex evaporation induced mass transfer phenomena such as bulk flow salt crystallization and evaporator surface soluble scale fouling during black liquor falling film evaporation. A first step in achieving this objective is accurately predicting the hydrodynamics and flow field for the falling film process. To this extent, the computational model presented correctly captures important flow

features such as interfacial deformation, free surface waves evolution and evaporation heat transfer. Species enrichment follows directly from liquid vaporization and is therefore correctly predicted by the model. To predict soluble salt precipitation in the evaporating liquid film, accurate crystallization/dissolution models based on empirically determined rate equations for black liquor would required. These models would define species depletion source terms based on supersaturation states of crystallizing salts and explicitly account for the inverse solubility property by including temperature dependence in the crystallization process.

7.2.3 Lagrangian Dynamics of Crystals

A more accurate representation of the flow physics and hydrodynamics of falling liquid films with crystallization can be obtained by explicitly accounting for the presence of crystals of different sizes in the liquid film. This formulation would allow for better capture of the force interactions between solid crystals and liquid thus ensuring more accurate description of the overall system dynamics. A logical extension of this formulation would be to allow for mass transfer analysis with respect to competition between crystallization on the heat transfer surface and bulk flow crystals.

REFERENCES

Abdullah, S. & Baris, O. 2006 Dehydration of sodium carbonate monohydrate with indirect microwave heating. *Thermochimica Acta* **448**, 31–36.

Abdulmalik, A. A., Tuzla, K. & John, C. C. 1998 Falling film evaporation of single component liquids. *Int. J. Heat Mass Transfer* **43** (12), 1623–1632.

Adams, T. N., Frederick, W. J., Grace, T. M., Hupa, M., Lisa, K., Jones, A. K. & Tran, H. 1997 Kraft Recovery Boilers. *Tappi Press, American Forest & Paper Association, New York* .

Alekseenko, S. V., Nakoryakov, Y. Y. & Pokusaev, B. G. 1985 Wave formation on a vertical falling liquid film. *AIChE J.* **31**, 1446.

Bayuadri, C. 2006 Stability of sodium sulfate dicarbonate ($2Na_2SO_4 \cdot Na_2CO_3$) crystals. *MSc. Thesis, School of Chemical & Biomolecular Engineering, Georgia Institute of Technology* .

Benjamin, T. B. 1957 Wave formation in laminar flow down an inclined plane. *J. Fluid Mech* **2** (554).

Benney, D. J. 1966 Long waves on liquid films. *J. Math. Phys.* **45**, 150–55.

Berberovic, E., van Hinsberg, N. P., Jarkirlic, S., Roisman, V. I. & Tropea, C. 2009 Drop impact onto a liquid layer of finite thickness: Dynamics of the cavity evolution. *Physical Review* **E 79** (036306).

Brackbill, J. U., Kothe, D. B. & Zemach, C. 1992 A continuum method for modeling surface tension. *J. Comput. Phys.* **100**, 335–354.

Cerne, G., Petelin, S. & Tiselj, I. 2001 Coupling of the interface tracking and the two-fluid models for the simulation of incompressible two-phase flow. *J. Comput. Phys.* **171:2**, 776–804.

Chang, H.-C. 1994 Wave evolution on a falling film. *Annu. Rev. Fluid Mech.* **26**, 103–36.

Chang, H.-C., Demekhin, E. A. & Kopelevich, D. I. 1993 Nonlinear evolution of waves on a vertically falling film. *J. Fluid Mech.* **250**, 433.

Chen, C. F. & Gao, Z. 2003 An anaylsis of black liquor falling film evaporation. *Int. J. Heat Mass Transfer* **47**, 1657–1671.

Chu, K. J. & Dukler, A. E. 1974 Statistical characterisitcs of thin wavy films: Part 2. Studies of the substrate and its wave structure. *AIChE J.* **20** (4), 695–706.

Chu, K. J. & Dukler, A. E. 1975 Statistical characterisitcs of thin wavy films: Part 3. Structure of large waves and their resistance to gas flow. *AIChE J.* **21** (3), 583–593.

Chun, K. R. & Seban, R. A. 1971 Heat transfer to evaporating liquid films. *Journal of Heat Transfer* pp. 391–397.

Clay, T. D. 2011 Evaporation principles and black liquor properties. `http://www.tappi.org/content/events/08kros/manuscripts/3-1.pdf`.

DeMartini, N. & Verrill, C. L. 2007 Minimizing soluble scales in black liquor evaporators: Application of metastable and solubility limit data for the $Na_2 - CO_3 - SO_4$ system. *Proc. Int. Chemical Recovery Conference* pp. 479–483.

Derek, L. G. & Robert, N. A. 1985 Multicomponent diffusion of aqueous sodium carbonate and aqueous sodium bicarbonate. *Can. J. Chem.* **63**, 2319–2323.

Dietze, F. G., Al-Sibai, F. & Kneer, R. 2009 Experimental study of flow seperation in laminar falling liquid films. *J. Fluid Mech.* **637**, 73–104.

Dietze, F. G., Leefken, A. & Kneer, R. 2008 Investigation of the backflow phenomenon in falling liquid films. *J. Fluid Mech.* **595**, 435–459.

Ferziger, J. H. & Peric, M. 2002 Computational Methods for Fluid Dynamic, 3rd edition. *Springer-Verlag Berlin* .

Forster, M., Augustin, W. & Bohnet, M. 1999 Influence of the adhesion force crystal/heat exchanger surface on fouling mitigation. *Chem. Eng. Process* **38:4**, 449–461.

Frederick Jr., W. V., Shi, B., Euhus, D. D. & Rousseau, R. W. 2004 Crystallization and control of sodium salt scales in black liquor concentrators. *TAPPI Journal* **3**, 7–12.

Gao, D., Morley, N. B. & Dhir, V. 2003 Numerical simulation of wavy falling film flow using VOF method. *J. Comput. Phys.* **192**, 624–642.

Golike, G. P., Pu, Q., Holman, K. L., Carlson, K. R., Wollwage, P. C., Folster, H. G. & Rankin, S. 1998 A new method for calculating equilibrium solubility of burkeite and sodium carbonate in black liquor. *Proc. Int. Chemical Recovery Conference* .

Gourdon, M. 2009 Sodium salt scaling in black liquor evaporators. *Ph.D. Thesis, Department of Energy and Environment, Chalmers University of Technology* .

Gourdon, M. 2011 The effects of flow velocity on crystallization fouling in falling film black liquor evaporators. *Proceedings of International Conference on Heat Exchanger Fouling and Cleaning* .

Gourdon, M., Vamling, L., Andersson, U. & Olausson, L. 2009 Crystallization in a pilot evaporator - aqueous solutions of Na_2CO_3 and Na_2SO_4. *Ind. Eng. Chem. Res.* **5**, 2401–2409.

Grace, T. M. 1975 A survey of evaporator scaling in the alkaline pulp industry. *Institute of Paper Chemistry Project 3234* pp. 107–111.

Hardt, S. & Wondra, F. 2008 Evaporation model for interfacial flows based on a continuum-field representation of the source terms. *J. Comput. Phys.* **227**.

Hedrick, R. H. & Kent, J. S. 1992 Crystallizing sodium salts from black liquor. *TAPPI J.* **75 (12)**, 107–111.

Hirt, C. W. & Nichols, B. D. 1981 Volume of fluid (VOF) method for the dynamics of free boundaries. *J. Comput. Phys.* **39**, 202.

Ho, L. W. & Patera, A. T. 1990 A Legendre spectral element method for simulation of unsteady incompressible viscous free-surface flows. *Comput. Methods Appl. Mech. Eng.* **80**, 355.

Holmberg, P. A., Berntsson, T. & Persson, L. 1991 Heat transfer in a falling film lithium bromide-water evaporator - an experimental study. *Int. Congress of Refrigeration* .

Hrvoje, J. 1996 Error analysis and estimation for the finite volume method with applications to fluid flows. *Ph.D. Dissertation, Department of Mechanical Engineering, Imperial College London* .

Incropera, F. P., Dewitt, D. P., Bergman, T. L. & Lavine, A. S. 2007 Principles of Heat and Mass Transfer, 6th edition. *John Wiley & Sons* .

Jayanti, S. & Hewitt, G. F. 1995 Hydrodynamics and heat transfer of wavy thin film flow. *Int. J. Heat Mass Transfer* **40** (1), 179–190.

Johansson, M. 2008 Heat transfer and hydrodynamics in falling film evaporation of black liquor. *Ph.D. Thesis, Department of Energy and Environment, Chalmers University of Technology* .

Johansson, M., Leifer, I., Vamling, L. & Olausson, L. 2009*a* Falling film hydrodynamics of black liquor under evaporative conditions. *Int. J. Heat Mass Transfer* **52**, 2769–2778.

Johansson, M., Vamling, L. & Olausson, L. 2009*b* Heat transfer in evaporating black liquor falling film. *Int. J. Heat Mass Transfer* **52**, 2759–2768.

Kapitza, P. L. & Kapitza, S. P. 1964 Collected papers of P. L. Kapitza (Edited by D. T. Haar). *Pergamon Press Oxford* .

Karapantsios, T. D., Paras, S. V. & Karabelas, A. J. 1989 Statistical characterisitcs of free falling films at high reynolds numbers. *Int. J. Multiphase Flow* **15** (1), 1–21.

Kheshgi, H. S. & Scriven, L. E. 1987 Disturbed film flow on a vertical plate. *Phys. Fluids* **30** (4), 990–997.

Kunkelman, C. & Stephan, P. 2009 CFD simulation of boiling flows using the volume-of-fluid method within OpenFOAM. *International Journal of Computation and Methodology* **56:8**, 631–646.

Kunugi, T. & Kino, C. 2005 DNS of falling film structure and heat transfer via MARS method. *Comp. Struct* **83**, 455–462.

Kutateladze, S. S. & Gogonin, I. I. 1979 Heat transfer in film condensation of slowly moving vapour. *Int. J. Heat Mass Transfer* **22**, 1593–1599.

Luan, N. T. & Balakotaiah, V. 2000 Modeling and experimental studies of wave evolution on free falling viscous films. *Phys. Fluids* **12** (9).

Malamataris, N. T. & Papanastasiou, T. C. 1991 Unsteady free surface flows on truncated domains. *Ind. Eng. Chem. Res.* **30**, 2211.

Miyara, A. 1999 Numerical analysis on flow dynamics and heat transfer of falling liquid films with interfacial waves. *Heat Mass Transfer* **35**, 298–306.

Miyara, A. 2000 Numerical simulation of wavy liquid film flow down on a vertical wall and inclined wall. *Int. J. Therm. Sci.* **39**, 1015–1027.

Muller-Steinhagen, H. & Branch, C. A. 1997 Heat transfer and heat transfer fouling in kraft black liquor evaporators. *Exp. Therm. Fluid Sci.* **14:4**, 425–437.

Nakoryakov, V. E., Pokusaev, B. G. & Alekseenko, S. V. 1976 Stationary two-dimensional rolling waves on a vertical film of liquid. *J. Engng. Phys* **30**, 517–521.

Nosoko, T. & Miyara, A. 2004 The evolution and subsequent dynamics of waves on a vertically falling liquid film. *Phys. Fluids* **16** (4), 1118–1126.

Nosoko, T., Yoshimura, P. N., Nagata, T. & Oyakawa, K. 1995 Characteristics of two-dimensional waves on a falling liquid film. *Chem. Eng. Science* **51** (5), 725–732.

Nusselt, W. 1916 Die oberflaechenkondensateion des Waserdampfes. *VDI Zeitschrift* **67**, 541–546; 569–575.

OpenCFD 2011 `http://www.openfoam.com`.

Pierson, W. F. & Whitaker, S. 1977 Some theoretical and experimental observations of the wave structure of falling liquid films. *Ind. Eng. Chem. Fundam.* **16** (4).

Ramaswamy, B., Chippada, S. & Joo, S. W. 1996 A full-scale numerical study of interfacial instabilities in thin-film flows. *J. Fluid Mech.* **325**, 163–194.

Rosier, M. A. 1997 Model to predict the precipitation of burkeite in the multiple-effect evaporator and techniques for controlling scaling. *TAPPI J.* **80 (4)**, 203–209.

Rusche, H. 2002 Computational fluid dynamics of dispersed two-phase flows at high phase fractions. *Ph.D. Dissertation, Department of Mechanical Engineering, Imperial College London* .

Salamon, T. R., Amstrong, R. C. & Brown, R. A. 1994 Traveling waves on vertical films: Numerical analysis using the finite element method. *Phys. Fluids* **6**, 2202–2220.

Schnabel, G. & Schlunder, E. U. 1980 Heat transfer from vertical walls to falling liquid films with or without evaporation. *Verfahrenstechnik* **14** (2), 79–83.

Schrage, R. W. 1953 A Theoretical study of Interphase Mass Transfer. *Columbia University Press, New York* pp. 32–43.

Shi, B., Frederick, W. J. & Rousseau, R. W. 2003 Effects of calcium and other ionic impurities on the primary nucleation of burkeite. *Ind. Eng. Chem. Res.* pp. 2861–2869.

Shkadov, V. Y. 1967 Wave conditions in the flow of thin layer of a viscous liquid. *Izv. Akad. Nauk SSSR, Mekh. Zhidik.* **Gaza 1** (43).

Shkadov, V. Y. 1968 Theory of wave flows of a thin layer of a viscous liquid. *Izv. Akad. Nauk SSSR, Mekh. Zhidik.* **Gaza 2**.

Sivashinsky, G. I. & Michelson, D. M. 1980 On the irregular wavy flow of a liquid film down a vertical plane. *Prog. Theor. Phys.* **63**, 2112.

Tanasawa, I. 1991 Advances in condensation heat transfer, in: J.P. Hartnett, T.F.Irvine (Eds.), Advances in Heat Transfer. *Academic Press, San Diego* **21**.

Thomas, J. W. 1995 Numerical Partial Differential Equations. *Springer New York* .

Tsvelodub, O. Y. & Trifonov, Y. Y. 1992 Nonlinear waves on the surface of a falling liquid film. Part 2. Bifurcations of the first-family waves and other types of nonlinear waves. *J. Fluid Mech.* **244**, 149.

Welch, J. W. & John, W. 2000 A volume of fluid based method for fluid flows with phase change. *J. Comput. Phys.* **160**, 662–682.

Xu, Z. F., Khoo, B. C. & Wijeysundera, N. E. 2008 Mass transfer across the falling film: Simulations and experiments. *Chem. Engr. Sci.* **63**, 2559–2575.

Yih, C. S. 1963 Stability of liquid flow down an inclined plane. *Phys. Fluids* **6** (321).